

# MEASUREMENT OF ELECTROWEAK PRODUCTION OF SAME-SIGN W BOSON PAIRS WITH ATLAS

3 William Kennedy DiClemente

7                   Presented to the Faculties of The University of Pennsylvania  
8       in Partial Fulfillment of the Requirements for the Degree of Doctor of Philosophy  
9                   2019 Last compiled: February 9, 2019

---

10  
11 I. Joseph Kroll, Professor, Physics  
12 Supervisor of Dissertation

14 Joshua Klein, Professor, Physics  
15 Graduate Group Chairperson

Dissertation Committee

17 Elliot Lipeles, Associate Professor, Physics  
18 Christopher Mauger, Associate Professor, Physics  
19 Burt Ovrut, Professor, Physics  
20 Justin Khouri, Professor, Physics  
21 I. Joseph Kroll, Professor, Physics

22 MEASUREMENT OF ELECTROWEAK PRODUCTION OF SAME-SIGN W BOSON PAIRS  
23 WITH ATLAS

24 COPYRIGHT  
25 2019  
26 William Kennedy DiClemente

27 All rights reserved.

---

## Acknowledgements

---

29 It would be impossible to properly thank everyone who has helped me along this journey; nevertheless  
30 I will attempt to be as thorough as possible.

31 First and foremost, I would like to thank my family. My parents, Gwynne Kennedy and John  
32 DiClemente, for always believing in me and listening to me attempt to explain what it is I am  
33 working on. My many feline friends past and present—Stella, Lucky, Julia, Elise, Lucille, Tweedie,  
34 Ruby, and Sylvie—for keeping me warm during the winter holidays back home. My girlfriend Amber  
35 Wright, for tolerating me these past few months and doing your best to keep me relatively sane.

36 Thanks to my advisor Joe Kroll for guiding me through the past six years at Penn; your advice  
37 both in physics and in life has been invaluable to my growth as a physicist and a person. Additional  
38 thanks to the rest of the ATLAS faculty at Penn: Elliot Lipeles, Evelyn Thomson, and Brig Williams.  
39 The amount of open collaboration between students and faculty irrespective of who works for whom  
40 has helped me learn so much.

41 I would also like to extend thanks to two important figures from before my time at Penn. Firstly,  
42 to Gardner Friedlander, my high school physics teacher who first got me interested in the subject.  
43 You were the first to show me how I could use a pen and paper to predict events in real life, a  
44 fascination of mine that has continued into my work here, just with much harder math and on a more  
45 fundamental scale. Secondly, my undergraduate research advisor, Al Goshaw, at Duke University.  
46 You gave a college freshman who thought particle physics was “pretty neat” the opportunity to do  
47 meaningful research with one of the leading collaborations in the field. Without either of you, I  
48 likely would not be in this position today.

49 Thanks to the members of the Inner Detector Alignment group, including but not limited to  
50 Anthony Morley for his guidance on my qualification task, and to Shih-Chieh Hsu, Pierfrancesco  
51 Butti, Matthias Danninger, Salvador Marti, and Steffen Henkelmann for numerous collaborative

52 alignment efforts.

53 The entire  $W^\pm W^\pm jj$  13 TeV analysis group, and those with whom I worked most closely: Philip  
54 Sommer, Emily Duffield, Rustem Ospanov, Stefanie Todt, and Liqing Zhang. Special thanks to  
55 Rustem for pushing me to find my voice in the analysis. Thanks to my  $W^\pm W^\pm jj$  14 TeV prospects  
56 collaborators Claire Lee and Karolos Potamiamos.

57 Lastly, thanks to my fellow Penn ATLAS graduate students, Bijan Haney, Joey Reichert, Khilesh  
58 Mistry, Leigh Schaefer, Bill Balunas, Christian Herwig, Elodie Ressegue, and many more, for lis-  
59 tening to my ramblings, answering my many questions, and for countless entertaining lunchtime  
60 discussions.

# ABSTRACT

62 MEASUREMENT OF ELECTROWEAK PRODUCTION OF SAME-SIGN W BOSON PAIRS  
 63 WITH ATLAS

William Kennedy DiClemente

J. Kroll

66 This thesis presents two studies of electroweak same-sign  $W^\pm W^\pm jj$  scattering with the ATLAS  
 67 experiment. The first is a measurement of the fiducial cross section at  $\sqrt{s} = 13$  TeV using  $36.1 \text{ fb}^{-1}$   
 68 of data recorded in 2015 and 2016. The electroweak production is observed with a signal significance  
 69 of  $6.9\sigma$ , and the fiducial cross section is measured to be  $\sigma_{\text{meas}}^{\text{fid}} = 2.91^{+0.51}_{-0.47}(\text{stat})^{+0.28}_{-0.29}(\text{sys}) \text{ fb}$ . The  
 70 second is a study on the future prospects for the  $W^\pm W^\pm jj$  process at the planned High-Luminosity  
 71 LHC, with a projected  $\sqrt{s} = 14$  TeV and  $3000 \text{ fb}^{-1}$  of data. The expected electroweak production  
 72 cross section is determined with a total uncertainty of 6%, and the purely longitudinal scattering  
 73 component is extracted with an expected significance of  $1.8\sigma$ . Additionally, some time is taken to  
 74 detail the alignment of the ATLAS Inner Detector subsystems, as good alignment performance is  
 75 essential for making high-quality physics measurements.

---

# Contents

---

77	Acknowledgements	iii
78	Abstract	v
79	Contents	vi
80	List of Tables	x
81	List of Figures	xiii
82	Preface	xix
83	1 Introduction	1
84	2 Theoretical Framework	3
85	2.1 Introduction to the Standard Model . . . . .	3
86	2.2 Electroweak symmetry breaking and the Higgs boson . . . . .	5
87	2.3 Electroweak vector boson scattering . . . . .	8
88	3 LHC and the ATLAS Detector	12
89	3.1 The Large Hadron Collider . . . . .	12
90	3.2 The ATLAS Detector . . . . .	12
91	3.2.1 The Inner Detector . . . . .	12
92	3.2.1.1 Pixel Detector . . . . .	12
93	3.2.1.2 Semiconductor Tracker . . . . .	12
94	3.2.1.3 Transition Radiation Tracker . . . . .	12

95	3.2.2	The Calorimeters . . . . .	13
96	3.2.2.1	Liquid Argon Calorimeters . . . . .	13
97	3.2.2.2	Tile Calorimeters . . . . .	13
98	3.2.3	The Muon Spectrometer . . . . .	13
99	3.2.4	Particle reconstruction . . . . .	14
100	3.2.4.1	Track reconstruction . . . . .	14
101	3.2.4.2	Muon reconstruction . . . . .	14
102	3.2.4.3	Electron reconstruction . . . . .	14
103	3.2.4.4	Jet reconstruction . . . . .	14
104	<b>4</b>	<b>Alignment of the ATLAS Inner Detector</b>	<b>15</b>
105	4.1	The alignment method . . . . .	16
106	4.1.1	Alignment levels . . . . .	19
107	4.1.2	Alignment coordinate systems . . . . .	20
108	4.2	Early 2015 alignment of the ATLAS detector . . . . .	21
109	4.2.1	June alignment procedure . . . . .	23
110	4.2.2	Alignment results . . . . .	24
111	4.2.2.1	Residual distributions from collisions . . . . .	25
112	4.2.2.2	Track parameter resolution from cosmic rays . . . . .	27
113	4.2.3	Error scaling . . . . .	28
114	4.3	Level 2 alignment of the TRT . . . . .	31
115	4.4	Momentum bias from sagitta deformations . . . . .	32
116	4.4.1	Sagitta bias monitoring with electron $E/p$ . . . . .	34
117	4.4.1.1	Measuring $\langle E/p \rangle$ . . . . .	35
118	4.4.1.2	Results in 13 TeV data . . . . .	36
119	<b>5</b>	<b>Measurement of same-sign <math>WW</math> production at <math>\sqrt{s} = 13</math> TeV with ATLAS</b>	<b>40</b>
120	5.0.1	Experimental overview of vector boson scattering . . . . .	40
121	5.0.2	Same-sign $W^\pm W^\pm$ scattering . . . . .	41
122	5.0.3	Overview of backgrounds . . . . .	43
123	5.1	Data and Monte Carlo samples . . . . .	45
124	5.1.1	Monte Carlo samples . . . . .	46
125	5.2	Object and event selection . . . . .	48

126	5.2.1	Object selection . . . . .	48
127	5.2.1.1	Muon candidate selection . . . . .	48
128	5.2.1.2	Electron candidate selection . . . . .	49
129	5.2.1.3	Jet candidate selection . . . . .	51
130	5.2.1.4	Treatment of overlapping objects . . . . .	51
131	5.2.2	Signal event selection . . . . .	52
132	5.3	Background estimations . . . . .	53
133	5.3.1	Estimation of the $WZ$ background . . . . .	54
134	5.3.2	Estimation of the $V\gamma$ background . . . . .	55
135	5.3.3	Estimation of backgrounds from charge misidentification . . . . .	57
136	5.3.3.1	Validation of the charge misidentification estimate . . . . .	59
137	5.3.4	Estimation of non-prompt backgrounds with the fake-factor method . . . . .	60
138	5.3.4.1	Overview of the default fake-factor method . . . . .	61
139	5.3.4.2	The fake-factor with $p_T^{\text{cone}}$ . . . . .	62
140	5.3.4.3	Application of the fake-factor . . . . .	65
141	5.3.4.4	Systematic uncertainties . . . . .	67
142	5.3.4.5	Results of the fake-factor . . . . .	70
143	5.3.4.6	Validation of the fake-factor . . . . .	72
144	5.3.5	Reduction of $WZ$ background using custom overlap removal . . . . .	72
145	5.4	Cross section measurement . . . . .	77
146	5.4.1	Maximum likelihood fit . . . . .	77
147	5.4.2	Definition of the fiducial volume . . . . .	79
148	5.4.3	Cross section extraction . . . . .	80
149	5.5	Summary of uncertainties . . . . .	81
150	5.5.1	Experimental uncertainties . . . . .	81
151	5.5.2	Theoretical uncertainties . . . . .	82
152	5.5.2.1	Uncertainties from EWK-QCD interference . . . . .	84
153	5.6	Results . . . . .	85
154	<b>6</b>	<b>Prospects for same-sign <math>WW</math> at the High Luminosity LHC</b>	<b>89</b>
155	6.0.1	Analysis Overview . . . . .	90
156	6.1	Theoretical motivation . . . . .	91
157	6.1.1	Experimental sensitivity to longitudinal polarization . . . . .	91

158	6.2 Monte Carlo samples . . . . .	92
159	6.3 Background estimations . . . . .	93
160	6.3.1 Truth-based isolation . . . . .	94
161	6.4 Object and event selection . . . . .	95
162	6.4.1 Object selection . . . . .	95
163	6.4.2 Event selection . . . . .	95
164	6.5 Selection optimization . . . . .	96
165	6.5.1 Random grid search algorithm . . . . .	97
166	6.5.2 Inputs to the optimization . . . . .	98
167	6.5.3 Results of the optimization . . . . .	99
168	6.6 Results . . . . .	100
169	6.6.1 Event yields . . . . .	100
170	6.6.2 Uncertainties . . . . .	104
171	6.6.3 Cross section measurement . . . . .	104
172	6.6.4 Longitudinal scattering significance . . . . .	105
173	<b>7 Conclusion</b>	109
174	<b>A Additional material on <math>W^\pm W^\pm jj</math> measurement at <math>\sqrt{s} = 13\text{TeV}</math></b>	110
175	A.1 Impact of experimental uncertainty on MC background estimations . . . . .	110
176	A.2 Additional signal region plots . . . . .	112
177	<b>B Additional material on <math>W^\pm W^\pm jj</math> prospects at the HL-LHC</b>	113
178	B.1 Truth isolation . . . . .	113
179	B.1.1 TRUTH1++ derivations . . . . .	114
180	B.1.2 Check of truth-based isolation . . . . .	115
181	B.1.3 Loose isolation working point . . . . .	115
182	B.2 Plots of other optimization variables . . . . .	118
183	<b>Bibliography</b>	120

---

## List of Tables

---

185    4.1	The four alignment levels for each of the detector subsystems. The total number of alignable structures and degrees of freedom (DoF) to be aligned are given for each level.	21
187    4.2	Summary of the highest level of alignment applied to each ID subsystem when deriving the June alignment. . . . .	24
189    4.3	Estimated value of the error scaling term $b$ for each subdetector component with the June alignment. . . . .	31
191    5.1	Predicted cross sections for EQK and QCD production of diboson processes relevant to VBS at $\sqrt{s} = 13\text{TeV}$ using the <b>SHERPA</b> MC generator. The numbers for the $W^\pm W^\pm jj$ process are bolded. Leptons are required to have $p_T \geq 25\text{ GeV}$ and lie within $ \eta  \leq 2.5$ with $m_{ll} > 20\text{ GeV}$ , and at least two jets are required with $p_T \geq 30\text{ GeV}$ and $ \eta  < 4.5$ . The VBS contributions are enhanced by requiring the dijet invariant mass $m_{jj} > 500\text{ GeV}$ and dijet separation $\Delta y_{jj} > 2.4$ . . . . .	43
197    5.2	Summary of MC samples used in the analysis. . . . .	47
198    5.3	Muon selection criteria. All muons are required to pass the preselection (top), and then either the signal (middle) or loose (bottom) criteria is applied to the preselected electrons. . . . .	49
200    5.4	Electron selection criteria. All electrons are required to pass the preselection (top), and then either the signal (middle) or loose (bottom) criteria is applied to the preselected electrons. . . . .	50
203    5.5	Jet selection criteria. All jets are required to pass the above selection in order to be used in the analysis. . . . .	51
205    5.6	Summary of the overlap removal procedure used in the analysis. If the criteria in the “check” column is met, in the “result” column, the object on the left of the arrow is removed in favor of the object on the right. . . . .	52
208    5.7	Summary of trigger requirements for electrons and muons for $\sqrt{s} = 13\text{TeV}$ data collected in 2015 and 2016. At least one of the triggers must be satisfied. . . . .	53
210    5.8	The signal event selection. . . . .	54
211    5.9	Event yields in the $WZ$ control region before normalization. All lepton flavor channels are combined. . . . .	55
213    5.10	Selection criteria for the $V\gamma$ control region. . . . .	56
214    5.11	Event yields in the $V\gamma$ control region. The $V\gamma$ scale factor of 1.77 is calculated by scaling up the $Z\gamma$ and $Z+jets$ backgrounds to account for the difference between the data and predicted total background. . . . .	57

217	5.12 Selection criteria for the same-sign inclusive validation region. . . . .	60
218	5.13 Event selection for the dijet region used for calculating the fake-factor. The selected	
219	lepton can pass either the nominal (signal) or loose selections. In the case of the nominal	
220	leptons, the $p_T > 27$ GeV requirement is replaced with $p_T > 15$ GeV. . . . .	66
221	5.14 Values of the fake-factor in each $p_T$ bin and for each individual systematic source. . . . .	69
222	5.15 Estimated yields for the fake lepton background. The estimated yield is shown in the first	
223	column together with the statistical uncertainty followed by the systematic uncertainties	
224	from variations of the the fake-factors within their statistical (stat.) and systematic	
225	(syst.) uncertainties. The labels $f_e$ and $f_\mu$ indicate the fake-factors for electrons and	
226	muons, respectively. . . . .	70
227	5.16 Selection criteria for the same-sign top fakes validation region. . . . .	72
228	5.17 Custom OR definition. Leptons must pass this selection in order to be counted for the	
229	trilepton veto. . . . .	76
230	5.18 Definition of the fiducial volume. . . . .	79
231	5.19 Impact of various systematic effects on the fiducial cross section measurement. The	
232	impact of a given source of uncertainty is computed by performing the fit with the	
233	corresponding nuisance parameter varied up or down by one standard deviation from its	
234	nominal value. . . . .	82
235	5.20 List of sources of experimental uncertainties on the reconstruction of physics objects. . . . .	83
236	5.21 Impact of experimental uncertainties for the $W^\pm W^\pm jj$ EWK processes in all channels.	83
237	5.22 Impact of experimental uncertainties for the $WZ$ process in all channels. . . . .	83
238	5.23 The set of generator level cuts used for generating the interference samples with <code>MadGraph</code> .	84
239	5.24 Cross sections for each different $W^\pm W^\pm jj$ production mode (inclusive, EWK only, QCD	
240	only, and interference only) generated using <code>MadGraph</code> . The cross sections are calculated	
241	using a minimal set of generator level cuts from events where the $W$ decays to a muon.	
242	5.25 Table of the data and prediction event yields in the signal region before the fit. Numbers	
243	are shown for the six lepton flavor and charge channels and for all channels combined.	
244	Here the $WZ$ background yields are normalized to the data in the $WZ$ control region. The	
245	background estimations from the fake-factor are included in the “Non-prompt” category,	
246	and backgrounds from $V\gamma$ production and electron charge misidentification are combined	
247	in the “ $e/\gamma$ conversions” category. Finally, $ZZ$ , $VVV$ , and $t\bar{t} + V$ backgrounds are	
248	combined in the “Other prompt” category. . . . .	85
249	5.26 Table of the data and prediction event yields in the signal region after the fit. Numbers	
250	are shown for the six lepton flavor and charge channels and for all channels combined. The	
251	background estimations from the fake-factor are included in the “Non-prompt” category,	
252	and backgrounds from $V\gamma$ production and electron charge misidentification are combined	
253	in the “ $e/\gamma$ conversions” category. Finally, $ZZ$ , $VVV$ , and $t\bar{t}V$ backgrounds are combined	
254	in the “Other prompt” category. . . . .	87
255	6.1 Summary of MC samples used in the analysis. . . . .	93
256	6.2 Truth-based isolation requirements for electrons and muons. . . . .	94
257	6.3 Summary of the signal event selection. . . . .	96
258	6.4 Updates to the $W^\pm W^\pm jj$ event selection criteria after optimization. Cuts not listed	
259	remain unchanged from the default selection in Table 6.3. . . . .	100
260	6.5 Signal and background event yields using the default event selection for an integrated	
261	luminosity of $\mathcal{L} = 3000 \text{ fb}^{-1}$ . Events containing a fake or charge-flipped electron are	
262	removed from their respective sources and combined into a single entry each. . . . .	101

---

263	6.6	Signal and background event yields using the optimized event selection for an integrated luminosity of $\mathcal{L} = 3000 \text{ fb}^{-1}$ . Events containing a fake or charge-flipped electron are removed from their respective sources and combined into a single entry each. . . . .	102
265	6.7	Summary of estimated experimental and rate uncertainties. . . . .	105
267	A.1	Impact of experimental uncertainties for the $W^\pm W^\pm jj$ QCD processes in all channels. .	110
268	A.2	Impact of experimental uncertainties for triboson process in all channels. . . . .	111
269	A.3	Impact of experimental uncertainties for $t\bar{t}V$ processes in all channels. . . . .	111
270	A.4	Impact of experimental uncertainties for the $W\gamma$ process in all channels. . . . .	111
271	A.5	Impact of experimental uncertainties for the $Z\gamma$ process in all channels. . . . .	111
272	A.6	Impact of experimental uncertainties for the $ZZ$ process in all channels. . . . .	112
273	B.1	Event yields prior to applying any form of truth-based isolation criteria. . . . .	113
274	B.2	Event yields after applying a test version of the truth-based isolation. . . . .	114
275	B.3	Electron and muon isolation requirements for the loose working point. . . . .	115
276	B.4	Event yields broken down by sample and by background type using the loose isolation workingpoint. Events contining a fake or charge-flipped electron are removed from their respective sample and added to the “fakes” and “charge flip” rows, respectively. Errors include statistical uncertainty and estimated systematic rate uncertainty based on the background process. . . . .	116
281	B.5	Event yields broken down by background type using the tight isolation workingpoint. Events contining a fake or charge-flipped electron are removed from their respective sample and added to the “fakes” and “charge flip” rows, respectively. Errors include statistical uncertainty and estimated systematic rate uncertainty based on the background process. . . . .	117

---

# List of Figures

---

287	2.1	An illustration of the potential term $V(\phi)$ in the cases where $\mu^2 > 0$ (left) and $\mu^2 < 0$ (right). The right-hand plot shows the Higgs potential, or ‘‘Mexican hat potential’’, with the minimum at $ \phi  = \sqrt{-\frac{\mu^2}{\lambda}}$ rather than at $ \phi  = 0$ as in the left-hand plot. . . . .	6
290	2.2	Feynman diagram of a generic VBS process. The gray circle represents any interaction with two incoming and two outgoing vector bosons, including any of the diagrams shown in Figures 2.3 and 2.4. . . . .	9
293	2.3	Leading order $VV \rightarrow VV$ Feynman diagrams involving EWK bosons. From left to right: $s$ -channel, $t$ -channel, $u$ -channel, and the quartic gauge coupling. . . . .	9
295	2.4	Leading order $VV \rightarrow VV$ Feynman diagrams involving the exchange of a Higgs boson. From left to right: $s$ -channel, $t$ -channel, and $u$ -channel. . . . .	9
297	2.5	Cross sections in nanobarns for five different longitudinally polarized VBS processes as a function of center of mass energy $\sqrt{s}$ . Without a Higgs boson (left), the cross sections grow unbounded with $\sqrt{s}$ . With a 120 GeV Higgs boson (right), the cross sections no longer diverge. . . . .	11
301	3.1	General cut-away view of the ATLAS detector. . . . .	13
302	4.1	Graphical representation of the effect of a misaligned detector element. The reconstructed particle track (dashed arrow) differs from the actual trajectory of the particle (solid arrow) due to the shift in one of the detector elements. The cyan lines represent the track-to-hit residuals. . . . .	16
306	4.2	Graphical representation of the ID alignment chain. . . . .	19
307	4.3	A schematic representation of the Inner Detector in the longitudinal plane with the global coordinate system overlaid on top. The Pixel detector and IBL are shown in blue, the SCT in green, and the TRT in red. The local coordinates for each subdetector module are inset on the right. . . . .	22
311	4.4	The $d_0$ distributions with respect to the reconstructed primary vertex using the $\sqrt{s} = 13$ TeV collision data sample reconstructed using the June (black) and March (green) alignments. The data is compared to a MC simulation using a perfect detector geometry (red). The distributions are normalized to the same number of entries. . . . .	25

315	4.5	Local $x$ (left) and local $y$ (right) residual distributions of the IBL planar sensors using the $\sqrt{s} = 13\text{TeV}$ collision data sample reconstructed using the June (black) and March (green) alignments. The data is compared to a MC simulation using a perfect detector geometry (red). The distributions are normalized to the same number of entries. . . . .	26
319	4.6	The mean of the local $x$ (left) and local $y$ (right) residual distributions as a function of the global $z$ position of each IBL module using the $\sqrt{s} = 13\text{TeV}$ collision data sample reconstructed using the June (black) and March (green) alignments. The data is compared to a MC simulation using a perfect detector geometry (red). . . . .	27
323	4.7	Local $x$ (top) and local $y$ (bottom) residual distributions for the Pixel barrel (excluding the IBL, left) and end-caps (right) using the $\sqrt{s} = 13\text{TeV}$ collision data sample reconstructed using the June (black) and March (green) alignments. The data is compared to a MC simulation using a perfect detector geometry (red). The distributions are normalized to the same number of entries. . . . .	28
328	4.8	Local $x$ residual distributions for the SCT barrel (left) and end-caps (right) using the $\sqrt{s} = 13\text{TeV}$ collision data sample reconstructed using the June (black) and March (green) alignments. The data is compared to a MC simulation using a perfect detector geometry (red). The distributions are normalized to the same number of entries. . . . .	29
332	4.9	Residual distributions for the TRT barrel (left) and end-caps (right) using the $\sqrt{s} = 13\text{TeV}$ collision data sample reconstructed using the June (black) and March (green) alignments. The data is compared to a MC simulation using a perfect detector geometry (red). The distributions are normalized to the same number of entries. . . . .	29
336	4.10	Representation of splitting a single cosmic ray track passing through the entire detector (left) into two separate tracks (right). . . . .	30
338	4.11	Distribution of the difference in the impact parameter $\Delta d_0$ (left) and charge over transverse momentum $\Delta q/p_T$ (right) between the two cosmic ray split tracks. The June (black) and March (green) alignments are compared. The distributions are normalized to the same number of entries. . . . .	30
342	4.12	Pull distributions in local $x$ (left) and $y$ (right) for the IBL using the $\sqrt{s} = 13\text{TeV}$ collision data sample after applying the error scaling. . . . .	31
344	4.13	Residual means by straw layer in two TRT $\phi$ -sectors affected by a tilt misalignment. The tilts in each of the three modules are clearly visible in the red points representing the reconstructed data prior to alignment. After four iterations of L2 alignment, the residual means in the gray points are flat. . . . .	32
348	4.14	Two dimensional map of residuals in the first layer of the TRT barrel vs $z$ and $\phi$ . Each bin represents the mean of a Gaussian fit to the TRT residuals in that bin. The map on the left is after the L3 (wire-by-wire) alignment of the TRT performed in 2010, and the map on the right is after the L2 alignment at the end of 2015. The $z$ -axis for both plots use the same scale. . . . .	33
353	4.15	Representation of a curl distortion in the detector. The image shows a cutaway in the transverse plane. The deformation is represented by the red arrows, and the impact on the reconstructed positive (blue) and negative (green) tracks are shown. The dashed lines represent the true particle trajectories, and the solid lines represent the reconstructed trajectories. . . . .	34
358	4.16	Geometric definition of the sagitta $s$ in relation to the length of the chord $l$ and the radius $r$ of a circular arc. . . . .	34
360	4.17	$E/p$ distributions of electrons and positrons in two different $\eta\phi$ bins of the detector. The left hand plot is taken from a region with no momentum bias where $\langle E/p \rangle^+ = \langle E/p \rangle^-$ , while the right hand plot shows an 8% disagreement in $\langle E/p \rangle$ between electrons and positrons. . . . .	36

364	4.18	Sagitta bias in the $\sqrt{s} = 13\text{TeV}$ data collected by ATLAS in 2016 as a function of $\eta$ and $\phi$ for the prompt (left) and reprocessed (right) alignments using the $E/p$ method. . . . .	37
365			
366	4.19	Sagitta bias in the $\sqrt{s} = 13\text{TeV}$ data collected by ATLAS in 2016 projected along $\eta$ for the prompt (gray) and reprocessed (blue) alignments using the $E/p$ method. . . . .	38
367			
368	4.20	Sagitta bias in the $\sqrt{s} = 13\text{TeV}$ data collected by ATLAS in 2017 as a function of $\eta$ and $\phi$ in reconstructed electrons (left) and after two iterations of momentum corrections (right) from the $E/p$ method. . . . .	38
369			
370	4.21	Sagitta bias in the $\sqrt{s} = 13\text{TeV}$ data collected by ATLAS in 2017 projected along $\eta$ in reconstructed electrons (gray) and after one (red) and two (blue) iterations of momentum corrections from the $E/p$ method. . . . .	39
371			
372			
373			
374	5.1	Tree-level Feynman diagrams for VBS EWK $VVjj$ production including triple gauge couplings involving $W$ and/or $Z$ bosons (top left and top middle), quartic gauge coupling (top right), or the exchange of a Higgs boson ( $s$ -channel bottom left and $t$ -channel bottom right). The labels are quarks ( $q$ ), fermions ( $f$ ), and gauge bosons ( $V = W, Z$ ). . . . .	42
375			
376	5.2	Tree-level Feynman diagrams for non-VBS EWK $VVjj$ production. The labels are quarks ( $q$ ), fermions ( $f$ ), and gauge bosons ( $V = W, Z$ ). . . . .	42
377			
378	5.3	Tree-level Feynman diagrams for QCD $VVjj$ production. The labels are quarks ( $q$ ), fermions ( $f$ ), and gauge bosons ( $V = W, Z$ ). . . . .	42
379			
380	5.4	Leading order Feynman diagrams for VBS EWK production of $W^\pm W^\pm jj$ events. The leftmost diagram contains a quartic gauge coupling vertex, and the rightmost diagram contains an exchange of a Higgs boson. . . . .	44
381			
382	5.5	$W^\pm W^\pm jj$ VBS event topology containing two leptons (1 and 2) with the same electric charge, two neutrinos, and two forward tagging jets (3 and 4) with large rapidity separation $\Delta y$ . . . . .	44
383			
384	5.6	Generator level comparisons at $\sqrt{s} = 7\text{TeV}$ of dijet invariant mass ( $m_{jj}$ , left) and dijet rapidity ( $\Delta y_{jj}$ , right) in EWK (red) and QCD (blue) $W^\pm W^\pm jj$ events with no selection cuts applied. . . . .	45
385			
386	5.7	ATLAS event display of a $pp \rightarrow W^+ W^+ \rightarrow \mu^+ \nu_\mu \mu^+ \nu_\mu jj$ event. The muons are represented by the red lines travelling from the ID through the MS, and the forward jets are represented by the blue cones with yellow energy deposits in the calorimeters. The direction of the $E_T^{\text{miss}}$ in the transverse plane is indicated by the gray dashed line in the inset image. . . . .	46
387			
388	5.8	Leading lepton $p_T$ (left) and $\eta$ (right) distributions in the $WZ$ control region before normalization. All lepton channels are combined. . . . .	55
389			
390	5.9	Trilepton invariant mass $m_{lll}$ distribution in the $WZ$ control region before normalization. All lepton channels are combined. . . . .	56
391			
392	5.10	Charge misidentification rates for electrons as a function of $ \eta $ and $p_T$ . Rates are calculated from $Z \rightarrow e^+ e^-$ MC after applying scale factors to approximate the charge mis-ID rates in data. . . . .	58
393			
394	5.11	Dilepton invariant mass distribution $m_{ll}$ for the $ee$ channel in the same-sign inclusive VR. . . . .	60
395			
396	5.12	$p_T$ distributions for the leading (left) and subleading (right) electron for the $ee$ channel in the same-sign inclusive VR. In these plots, the cut requiring $m_{ee}$ to fall within the $Z$ mass window has been inverted in order to test the modelling away from the $Z$ peak. . . . .	61
397			
398	5.13	$\Delta p_T$ distributions for nominal (blue) and loose (red) muons in simulated $t\bar{t}$ events. Each muon has been matched to a truth-level jet. Both distributions are normalized to unit area. . . . .	63
399			
400			
401			
402			
403			
404			
405			
406			
407			
408			
409			

410	5.14	$\Delta p_T$ distributions for muons (top) and electrons (bottom) in simulated $t\bar{t}$ events. Each lepton has been matched to a truth-level jet, and that truth jet has had its $p_T$ corrected to include all truth muons within a cone of $\Delta R < 0.4$ . The nominal leptons are in black. $\Delta p_T$ is calculated for the loose leptons using $p_T$ (red) and $p_T + p_T^{\text{cone}}$ (blue). . . . .	64
411			
412	5.15	Distributions of $p_T^{\text{cone}}/p_T$ for nominal (black) and loose (red) muons in simulated $t\bar{t}$ events. . . . .	65
413			
414	5.16	The measured fake-factor as a function of muon $p_T + p_T^{\text{cone}}$ . The error bars represent the statistical uncertainty only. . . . .	66
415			
416	5.17	The measured fake-factor as a function of electron $p_T + p_T^{\text{cone}}$ in the central ( $ \eta  < 1.37$ , blue) and forward ( $ \eta  > 1.37$ , red) regions of the detector. The error bars represent the statistical uncertainty only. . . . .	67
417			
418	5.18	Graphical representation of the fake-factor application using $p_T + p_T^{\text{cone}}$ . The value of $p_T + p_T^{\text{cone}}$ for the loose lepton is used to “look up” the fake-factor weight which is then applied to the event. The loose lepton’s $p_T$ becomes $p_T + p_T^{\text{cone}}$ for the purpose of the fake background estimation. . . . .	68
419			
420	5.19	Systematic variations in the fake-factor as a function of muon $p_T + p_T^{\text{cone}}$ . The individual fake-factors obtained for each systematic variation are displayed with their statistical uncertainties. . . . .	70
421			
422	5.20	Systematic variations in the fake-factor as a function of electron $p_T + p_T^{\text{cone}}$ in the central ( $ \eta  < 1.37$ , top) and forward ( $ \eta  > 1.37$ , bottom) regions of the detector. The individual fake-factors obtained for each systematic variation are displayed with their statistical uncertainties. . . . .	71
423			
424	5.21	Distributions of the subleading lepton $p_T$ in the same-sign top fakes VR for $\mu^\pm\mu^\pm$ events (top right), $e^\pm e^\pm$ events (top left), $\mu^\pm e^\pm$ events (bottom left), and all events combined (bottom right). All errors are statistical only. . . . .	73
425			
426	5.22	Pseudorapidity ( $\eta$ ) distributions of truth muons (top) and electrons (bottom) for Sherpa $W^\pm W^\pm jj$ and $WZ$ MC samples. The blue vertical lines represent the allowed $\eta$ range for each lepton flavor. The numbers correspond to the number of raw MC events that fall within and outside of the allowed $\eta$ range for each MC sample. . . . .	74
427			
428	5.23	Distributions of $p_{T,\text{ratio}}(\mu, j)$ for EWK and QCD $W^\pm W^\pm jj$ signal (black) and $WZ$ background (teal) for truth-matched third muons in events that pass the trilepton veto. Both distributions are normalized to unit area. The associated efficiency curves are on the right where efficiency is defined as the percentage of total events that would pass a cut on $p_{T,\text{ratio}}(\mu, j)$ at a given value on the $x$ -axis. . . . .	74
429			
430	5.24	Distributions of $\Delta R(\mu, j)$ for EWK and QCD $W^\pm W^\pm jj$ signal (black) and $WZ$ background (teal) for truth-matched third muons in events that pass the trilepton veto. Both distributions are normalized to unit area. The associated efficiency curves are on the right where efficiency is defined as the percentage of total events that would pass a cut on $\Delta R(\mu, j)$ at a given value on the $x$ -axis. . . . .	75
431			
432	5.25	Distributions of $p_{T,\text{ratio}}(e, j)$ for EWK and QCD $W^\pm W^\pm jj$ signal (black) and $WZ$ background (teal) for truth-matched third electrons in events that pass the trilepton veto. Both distributions are normalized to unit area. The associated efficiency curves are on the right where efficiency is defined as the percentage of total events that would pass a cut on $p_{T,\text{ratio}}(e, j)$ at a given value on the $x$ -axis. . . . .	75
433			
434	5.26	Two-dimensional plots of $p_{T,\text{ratio}}(\mu, j)$ vs $\Delta R(\mu, j)$ for truth-matched third muons in events that pass the trilepton veto for EWK and QCD $W^\pm W^\pm jj$ signal (left) and $WZ$ background (right). The blue overlay indicates the area in which the third leptons will pass the custom OR and result in the event failing the trilepton veto. . . . .	76
435			
436			
437			
438			
439			
440			
441			
442			
443			
444			
445			
446			
447			
448			
449			
450			
451			
452			
453			
454			
455			
456			

457	5.27	Visual representation of the different kinematic regions relevant to the cross section measurement. The acceptance factor $\mathcal{A}$ converts from the truth level total phase space to the truth level fiducial region, and the efficiency correction $\mathcal{C}$ translates the fiducial region in to the reconstruction level signal region. . . . .	80
461	5.28	The dijet invariant mass $m_{jj}$ distributions for data and predicted signal and background in the signal region after the fit. The shaded band represents the statistical and systematic uncertainties added in quadrature. Note that the bins have been scaled such that they represent the number of events per 100 GeV in $m_{jj}$ . The background estimations from the fake-factor are included in the “Non-prompt” category, and backgrounds from $V\gamma$ production and electron charge misidentification are combined in the “ $e/\gamma$ conversions” category. Finally, $ZZ$ , $VVV$ , and $t\bar{t}+V$ backgrounds are combined in the “Other prompt” category. . . . .	86
469	5.29	The event yields for data and predicted signal and background in the $WZ$ and low- $m_{jj}$ control regions after the fit. The shaded band represents the statistical and systematic uncertainties added in quadrature. The background estimations from the fake-factor are included in the “Non-prompt” category, and backgrounds from $V\gamma$ production and electron charge misidentification are combined in the “ $e/\gamma$ conversions” category. Finally, $ZZ$ , $VVV$ , and $t\bar{t}V$ backgrounds are combined in the “Other prompt” category. . . . .	86
475	5.30	Comparison of the measured $W^\pm W^\pm jj$ EWK fiducial cross section with theoretical calculations from SHERPA v2.2.2 and POWHEG-BOX v2. The light orange band represents the total experimental uncertainty on the measured value, and the dark orange hashed band is the statistical uncertainty. For the simulations, the light blue band represents the total theoretical uncertainty, and the dark blue hashed band are the scale uncertainties. The theory predictions do not include the interference between the EWK and QCD production. . . . .	88
482	6.1	Comparison of the leading (left) and subleading (right) lepton $p_T$ distributions for purely longitudinal (LL, black) and mixed polarization (LT+TT, cyan) $W^\pm W^\pm jj$ events. . . . .	91
484	6.2	Comparison of the azimuthal dijet separation ( $ \Delta\phi_{jj} $ ) for purely longitudinal (LL, black) and mixed polarization (LT+TT, cyan) $W^\pm W^\pm jj$ events. . . . .	92
486	6.3	A visual representation of a two-dimensional rectangular grid (left) and a random grid (right) in variables $x$ and $y$ . The signal events are the black circles, and the red squares are the background events. Each intersection of gray dashed lines represents a cut point to be evaluated by the optimization. . . . .	98
490	6.4	Leading (top) and subleading (bottom) jet $p_T$ distributions. The default and optimized cuts are represented by the red and green dashed lines, respectively. The $W^\pm W^\pm jj$ EWK signal (black points) is normalized to the same area as the sum of the backgrounds (colored histogram). . . . .	101
494	6.5	Lepton-jet centrality distribution. The default and optimized cuts are represented by the red and green dashed lines, respectively. The $W^\pm W^\pm jj$ EWK signal (black points) is normalized to the same area as the sum of the backgrounds (colored histogram). . . . .	102
497	6.6	$p_T$ distributions for the leading jet using the default (left) and optimized (right) event selections for all channels combined. . . . .	103
499	6.7	$p_T$ distributions for the subleading jet using the default (left) and optimized (right) event selections for all channels combined. . . . .	103
501	6.8	$p_T$ distributions for lepton-jet centrality $\zeta$ using the default (left) and optimized (right) event selections for all channels combined. . . . .	104

---

503	6.9	Projections of the statistical (black), theoretical (blue), systematic (yellow), and total (red) uncertainties on the measured cross section as a function of integrated luminosity using the optimized event selection. . . . .	106
506	6.10	Dijet azimuthal separation ( $ \Delta\phi_{jj} $ ) for the low $m_{jj}$ region ( $520 < m_{jj} < 1100$ GeV, top) and the high $m_{jj}$ region ( $m_{jj} > 1100$ GeV, bottom). The purely longitudinal (LL, gray) is plotted separately from the mixed and transverse (LT+TT, cyan) polarizations. . . . .	107
509	6.11	Projections of the expected longitudinal scattering significance as a function of integrated luminosity when considering all sources of uncertainties (black) or only statistical uncertainties (red). . . . .	108
512	B.1	Number of truth particles within $\Delta R < 0.4$ of a selected muon or electron using the ATLAS standard TRUTH1 (left) and the custom TRUTH1++ (right) derivations in $t\bar{t}$ simulation. The complete truth record is stored in the TRUTH1++ derivation, and this is best seen in the first bin, where the lepton has no nearby truth particles. . . . .	114
516	B.2	Leading lepton $p_T$ distribution. The default and optimized cuts are represented by the red and green dashed lines, respectively. The $W^\pm W^\pm jj$ EWK signal (black points) is normalized to the same area as the sum of the backgrounds (colored histogram). . . . .	118
519	B.3	Dilepton invariant mass distribution. The default and optimized cuts are represented by the red and green dashed lines, respectively. The $W^\pm W^\pm jj$ EWK signal (black points) is normalized to the same area as the sum of the backgrounds (colored histogram). . . . .	118
523	B.4	Dijet invariant mass distribution. The default and optimized cuts are represented by the red and green dashed lines, respectively. The $W^\pm W^\pm jj$ EWK signal (black points) is normalized to the same area as the sum of the backgrounds (colored histogram). . . . .	119

---

## Preface

---

526 This thesis presents the major highlights of my work with the ATLAS experiment as a graduate  
527 student at the University of Pennsylvania from Fall of 2013 until early Spring of 2019.

528 The first step of working on the experiment is to complete a *qualification task* in order to be  
529 included on the author list of ATLAS publications. These tasks are an opportunity to contribute  
530 to the experiment as a whole, such as maintaining detector hardware or monitoring physics perfor-  
531 mance. For my qualification task, I worked with the Inner Detector Alignment group which works  
532 to make sure we have accurate knowledge of the locations of each and every sensor in the tracking  
533 detector. My qualification task involved investigating a possible momentum bias in the Monte Carlo  
534 (MC) simulated data. The MC is supposed to be reconstructed with a perfect detector geometry  
535 which should in principle be free of any momentum biases. Ultimately I determined that the size of  
536 the biases were small enough to be negligible compared to what is seen in the real data, and that  
537 they could be corrected for if necessary.

538 My work with the alignment group would continue for the duration of my time here at Penn. In  
539 early 2015, at the start of the LHC’s second data-taking run (Run 2), I assisted with the validation  
540 of the first set of alignment constants using  $\sqrt{s} = 13$  TeV proton-proton collision data. At this point  
541 I took over the responsibility of alignment of the TRT subdetector. The TRT was aligned to high  
542 accuracy in Run 1, and over the course of my time working on alignment, the TRT never required  
543 a straw-by-straw alignment; however it did require a module-level alignment at the end of 2015.  
544 My final responsibility in the alignment group was monitoring momentum biases using the energy-  
545 momentum ratio ( $E/p$ ) of electrons. For the large data reprocessing, the  $E/p$  method served as a  
546 cross check to a similar method using  $Z$  boson events for monitoring and aligning out momentum  
547 biases in the detector. The results from both methods were also used in the uncertainties for the  
548 tracking measurements.

549 On the analysis side, I had previous experience in Standard Model (SM) electroweak physics  
550 from my time as an undergraduate at Duke University, and it remained a point of interest for  
551 me in graduate school. As such, I was happy to work with fellow Penn students on the cross  
552 section measurement of SM  $WZ$  diboson production with the early  $\sqrt{s} = 13$  TeV ATLAS data.  
553 My contribution to the analysis was primarily on the software side, as I maintained and updated  
554 the analysis framework. While the  $WZ$  measurement is not covered by this thesis, it provided me  
555 with invaluable analysis experience in electroweak physics, as well as a detailed understanding of a  
556 major background to many diboson processes. The results for this analysis can be found published  
557 in Physics Letters B in 2016 [1].

558 The final two analyses I worked on involved the scattering of same-sign  $W$  bosons, and they make  
559 up the majority of this thesis. The first analysis is a measurement of the  $W^\pm W^\pm jj$  cross section  
560 at  $\sqrt{s} = 13$  TeV. This measurement along with that of the CMS collaboration represent the first  
561 observation of the  $W^\pm W^\pm jj$  scattering process. My primary contribution to the analysis is in the  
562 estimation of the fake lepton background, where we implemented a brand new version of the fake-  
563 factor method using particle isolation variables. I also did a preliminary study of the interference  
564 between electroweak and strong production of  $W^\pm W^\pm jj$  events, assisted in the production of data  
565 samples for use with the analysis framework, and used my familiarity with the  $WZ$  process to  
566 optimize the rejection of this background. Ultimately the results of this optimization were not  
567 included in the final result; however, it is still covered in the thesis in the hopes that it will be useful  
568 for similar analyses in the future. The formal publication for this measurement will likely be coming  
569 out within the next few months.

570 The second  $W^\pm W^\pm jj$  analysis is a study on the prospects for a measurement of the process at the  
571 upgraded High-Luminosity LHC, scheduled to begin operation in 2026. Here my main contribution  
572 was an optimization of the event selection using a Random Grid Search algorithm. Through the  
573 optimization we expect to take advantage of the higher center of mass energy and greater volume of  
574 data and tighten certain selection cuts to increase the strength of the  $W^\pm W^\pm jj$  signal. In addition, I  
575 once again maintained and updated the analysis framework and produced the group's data samples,  
576 and I also developed a truth-based particle isolation criteria in order to reduce contributions from  
577 backgrounds involving the top quark. The results of this prospects study will be published as a part  
578 of the annual Yellow Report for the High-Luminosity LHC.

579

Will K. DiClemente

Philadelphia, February 2019

# CHAPTER 1

---

## Introduction

---

582 The Large Hadron Collider (LHC) at CERN is the most powerful collider experiment in the world.  
 583 At the time of its construction, the largest unanswered question in the Standard Model (SM) was  
 584 the mechanism behind electroweak symmetry breaking (EWSB). As a result, one of the primary  
 585 goals of the experiment is to learn as much as possible about this mechanism. Thus far, the LHC  
 586 has succeeded in discovering a particle consistent with the long-awaited Higgs boson. In addition,  
 587 measurements of many SM processes have been performed for the first time or at better precision  
 588 than before thanks to the high collision energy and large volume of data collected by the LHC.

589 Processes involving the scattering of two massive electroweak (EWK) gauge bosons are of par-  
 590 ticular interest at the LHC for two main reasons. Firstly, they allow for tests of the self-interactions  
 591 predicted by the EWK gauge theory through triple and quartic gauge couplings. While the triple  
 592 couplings have been studied by previous experiments as well as at the LHC, the quartic couplings  
 593 of the massive gauge bosons have not been accessible previously. Thus, processes involving these  
 594 couplings can be measured and compared to the SM predictions for the first time. Secondly, the scat-  
 595 tering of two massive gauge bosons is sensitive to the underlying EWSB mechanism. The  $W^\pm$  and  
 596  $Z$  bosons are given non-zero masses—and consequently a longitudinal polarization mode—through  
 597 the Higgs mechanism, and thus their interactions serve as a direct probe of the symmetry breaking  
 598 sector.

599 This thesis presents two separate analyses dealing with the scattering of two same-sign  $W^\pm$   
 600 bosons with the LHC’s ATLAS experiment. The  $W^\pm W^\pm jj$  process is one of the most sensitive to the  
 601 goals above: it has access to the  $WWWW$  quartic gauge coupling, production modes that involve the  
 602 exchange of a Higgs boson, and relatively low backgrounds. Evidence of EWK  $W^\pm W^\pm jj$  production  
 603 was first seen by the ATLAS and CMS experiments at  $\sqrt{s} = 8$  TeV, however the data set was too

604 small to claim observation of the process. The first analysis covered here is the follow up to the above  
605 ATLAS measurement, measuring the EWK fiducial cross section at  $\sqrt{s} = 13$  TeV with a larger data  
606 sample. The second analysis explores the prospects for future measurements of the  $W^\pm W^\pm jj$  process  
607 at the planned High-Luminosity LHC (HL-LHC). A measurement of the production cross section  
608 as well as sensitivity to the purely longitudinal component of the  $W^\pm W^\pm$  scattering is presented.

609 In addition to the SM measurements, a part of this thesis is devoted to alignment of the detector  
610 components making up ATLAS’s Inner Detector (ID). Precise knowledge of the locations of detector  
611 elements is essential for accurate particle track reconstruction, which in turn results in improved  
612 resolutions for physics measurements. The ATLAS alignment algorithm determines the positions  
613 of each ID sensor through minimizing the distance between reconstructed particle tracks and the  
614 sensor hit position. Special emphasis is given to the monitoring of momentum biases that may exist  
615 in the ID even after alignment.

616 This first few chapters of this thesis are intended to provide context for the main topics. Chapter 2  
617 gives a brief introduction to the Standard Model with a focus on the mechanism of electroweak  
618 symmetry breaking and vector boson scattering. The experimental apparatus—the LHC and the  
619 ATLAS detector—are detailed in Chapter 3. The next three chapters present the main body of  
620 work. Chapter 4 covers the alignment of the ATLAS Inner Detector. Finally, Chapters 5 and  
621 6 detail the ATLAS  $\sqrt{s} = 13$  TeV  $W^\pm W^\pm jj$  cross section measurement and the  $\sqrt{s} = 14$  TeV  
622 HL-LHC  $W^\pm W^\pm jj$  prospects study, respectively.

## CHAPTER 2

---

# Theoretical Framework

---

625 This chapter outlines the theoretical groundwork for the rest of the thesis. An overview of the Stan-  
 626 dard Model of particle physics (SM) is given in Section 2.1, followed by the electroweak symmetry  
 627 breaking mechanism involving the Higgs boson in Section 2.2. Finally, Section 2.3 will go into detail  
 628 on the interests of electroweak vector boson scattering (VBS).

629 **2.1 Introduction to the Standard Model**

630 The Standard Model of particle physics serves as a mathematical description of the fundamental  
 631 particles of the universe and their interactions. It has been developed over the course of the past  
 632 century, incorporating both predictions from theory and results from experiments. All in all, the SM  
 633 has proven remarkably successful in accurately describing particle interactions seen in experiments.

634 The SM is a quantum field theory (QFT) [2, 3] in which the fundamental particles are represented  
 635 as excited states of their corresponding fields. The spin- $\frac{1}{2}$  fermionic fields give rise to the quarks  
 636 and leptons comprising ordinary matter, the spin-1 fields correspond to the electroweak bosons and  
 637 the gluon which mediate the electroweak and strong forces, respectively, and finally the scalar Higgs  
 638 field is responsible for electroweak symmetry breaking. The excitations and interactions of the fields  
 639 are governed by the SM Lagrangian, which is invariant under local transformations of the group  
 640  $SU(3) \times SU(2) \times U(1)$ . **TODO: need more detail/refinement here**

641 The first quantum field theory to be developed was quantum electrodynamics (QED) [4], which  
 642 describes the electromagnetic interaction. The theory predicts the existence of a  $U(1)$  gauge field  
 643 that interacts with the electrically charged fermions. This field corresponds to the photon. A key  
 644 aspect of QED is that it is perturbative. The coupling constant  $\alpha = e^2/4\pi$  is small, where  $e$  is

645 electrical charge of the field, allowing for the use of perturbation theory in calculations. In this case,  
 646 calculations can be written as a power series in  $\alpha$ , where successive higher order terms contribute  
 647 less to the final result.

648 The strong interaction—the theory of quarks and gluons—has also been described using QFT  
 649 as quantum chromodynamics (QCD). The symmetry group for QCD is SU(3), and its eight gen-  
 650 erators correspond to the eight differently charged, massless gluons [5]. Unlike in QED, which has  
 651 positive and negative charges, the strong force has three “colors”. Color charge combined with the  
 652 non-Abelian nature of  $SU(3)$ , which allows the gluons to interact with each other, result in the  
 653 most well-known property of QCD: color confinement. In order to increase the separation between  
 654 two color-charged quarks, the amount of energy required increases until it becomes energetically  
 655 favorable to pair-produce a new quark-antiquark pair, which then bind to the original quarks. The  
 656 end result of this is that only color-neutral objects exist in isolation. What this means for the strong  
 657 coupling constant  $\alpha_s$  is that its value at the low energies where confinement occurs is large, on  
 658 the order of  $\alpha_s \sim 1$ . The consequence of this is that perturbation theory cannot be used to accu-  
 659 rately approximate interactions. While this appears at first to be a critical problem for predictions,  
 660 fortunately it turns out that  $\alpha_s$  “runs”, or decreases in magnitude at higher energy [6, 7]. This so-  
 661 called “asymptotic freedom” allows QCD to be calculated perturbatively [8] at energies accessible  
 662 by collider experiments including the LHC.

663 The last gauge field corresponds to the weak interaction. Ultimately, the weak  $SU(2)$  and the  
 664 electromagnetic  $U(1)$  mix to form the  $SU(2) \times U(1)$  *electroweak* (EWK) interaction [9, 10]. A  
 665 more detailed description of the mixing will be discussed in conjunction with electroweak symmetry  
 666 breaking (EWSB) in Section 2.2; however, a summary of the resulting EWK interaction is presented  
 667 here, at the risk of some repeated information to follow. There are three weak isospin bosons arising  
 668 from the  $SU(2)$  group ( $W_\mu^1$ ,  $W_\mu^2$ , and  $W_\mu^3$ ) and one weak hypercharge boson from the  $U(1)$  group  
 669 ( $B_\mu$ ). The  $W_3$  and  $B$  bosons mix according to the weak mixing angle  $\theta_W$  to form the  $Z$  boson and  
 670 the photon according to:

$$\begin{pmatrix} \gamma \\ Z \end{pmatrix} = \begin{pmatrix} \cos \theta_W & \sin \theta_W \\ -\sin \theta_W & \cos \theta_W \end{pmatrix} \begin{pmatrix} B_\mu \\ W_\mu^3 \end{pmatrix} \quad (2.1)$$

671 The value of  $\theta_W$  is not predicted by the SM; it is one example of an experimental input to the  
 672 theory, measured to be  $\sin^2 \theta_W = 0.23153 \pm 0.00016$  [11]. The charged  $W^\pm$  bosons are a mixture of  
 673 the remaining  $W_\mu^1$  and  $W_\mu^2$  bosons:

$$W^\pm = \frac{1}{\sqrt{2}}(W_\mu^1 \mp iW_\mu^2) \quad (2.2)$$

674 Unlike the photon (and the gluon of QCD), the  $W^\pm$  and  $Z$  bosons are massive. This means that  
 675 even though SU(2) is non-Abelian, the range of interaction is short and confinement does not occur.  
 676 Lastly, the EWK interaction is chiral, only coupling to the left-handed component of the fermion  
 677 fields

678 One final field remains within the SM: the scalar Higgs field. It was originally proposed in the  
 679 1960's to explain the masses of the  $W^\pm$  and  $Z$  bosons [12, 13, 14] and is the mechanism for the  
 680 EWSB process. The particle associated with the field is a massive scalar boson, which was at last  
 681 discovered by ATLAS and CMS in 2012 [15, 16] with a mass of 125 GeV.

## 682 2.2 Electroweak symmetry breaking and the Higgs boson

683 The results of electroweak mixing and the implications of the Higgs field have been introduced  
 684 in the previous section. If the EWK theory were an unbroken symmetry, the associated  $W^\pm$  and  
 685  $Z$  bosons would be massless; however, when observed experimentally, they were found to be quite  
 686 heavy [17, 18], at around 80 GeV and 91 GeV, respectively [19]. Here, a more detailed explanation  
 687 of the Higgs mechanism and how it “spontaneously breaks” the EWK symmetry, resulting in the  
 688 three massive bosons ( $W^\pm$  and  $Z$ ) and one massless boson (photon), is presented.

689 To see how the Higgs mechanism results in the massive vector bosons and a massless photon,  
 690 consider the following. Beginning with a complex scalar doublet  $\phi$  defined as:

$$\phi = \begin{pmatrix} \phi^+ \\ \phi^0 \end{pmatrix} = \sqrt{\frac{1}{2}} \begin{pmatrix} \phi_1 + i\phi_2 \\ \phi_3 + i\phi_4 \end{pmatrix} \quad (2.3)$$

691 a Lagrangian  $\mathcal{L}$  can be written:

$$\mathcal{L} = (\mathcal{D}_\mu \phi)^\dagger (\mathcal{D}^\mu \phi) - \mu^2 \phi^\dagger \phi - \lambda(\phi^\dagger \phi)^2 \quad (2.4)$$

692 where  $\lambda > 0$  and  $\mathcal{D}_\mu$  is the covariant derivative.  $\mathcal{D}_\mu$  is defined such that  $\mathcal{L}$  is invariant under a local  
 693 SU(2)  $\times$  U(1) gauge transformation:

$$\mathcal{D}_\mu \phi = \left( \partial_\mu + \frac{ig}{2} \tau_a W_\mu^a + \frac{ig'}{2} B_\mu \right) \phi \quad (2.5)$$

694 where  $W_\mu^a$  ( $a = 1, 2, 3$ ) are the SU(2) fields with generators  $\tau_a$  and coupling constant  $g$ , and  $B_\mu$  is  
 695 the U(1) field with coupling constant  $g'$ .

696 Isolating the potential term:

$$V(\phi) = \mu^2 \phi^\dagger \phi + \lambda(\phi^\dagger \phi)^2 \quad (2.6)$$

697 a choice must be made on the sign of  $\mu^2$ , and the case of interest is for  $\mu^2 < 0$ . This results in  
 698 the famous “mexican hat potential” shown in Figure 2.1, which is minimized along the collection of  
 699 points:

$$\phi^\dagger \phi = \frac{1}{2} (\phi_1^2 + \phi_2^2 + \phi_3^2 + \phi_4^2) = -\frac{\mu^2}{2\lambda} \quad (2.7)$$

700 This means that the minimum of the potential is not at  $\phi = 0$  (as it would be in the case where  
 701  $\mu^2 > 0$ ), but rather at a value:

$$v \equiv \sqrt{-\frac{\mu^2}{\lambda}} \quad (2.8)$$

702 With no loss of generality due to the SU(2) symmetry,  $\phi_1 = \phi_2 = \phi_4 = 0$  can be imposed on  
 703 Equation 2.7 leaving  $\phi_3^2 = v^2$ . Finally, the *vacuum expectation value* (VEV) of the field can be  
 704 written as:

$$\langle \phi \rangle = \sqrt{\frac{1}{2}} \begin{pmatrix} 0 \\ v \end{pmatrix} \quad (2.9)$$

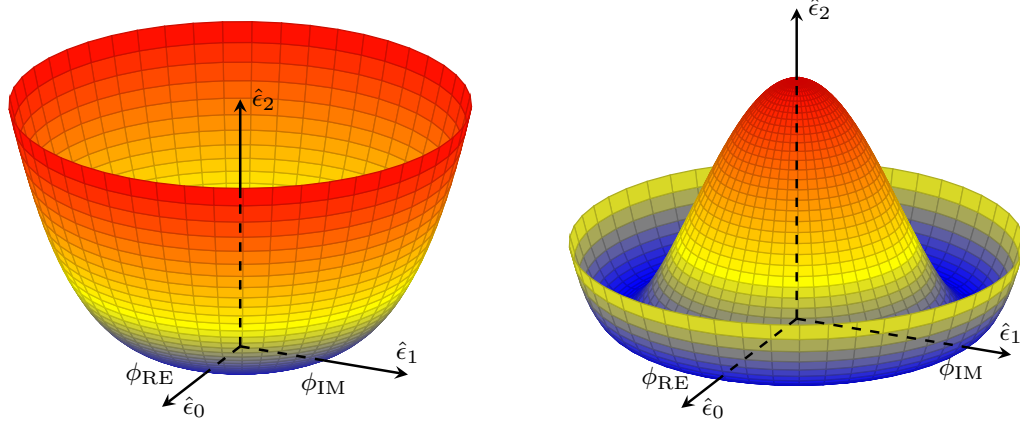


Figure 2.1: An illustration of the potential term  $V(\phi)$  in the cases where  $\mu^2 > 0$  (left) and  $\mu^2 < 0$  (right). The right-hand plot shows the Higgs potential, or “Mexican hat potential”, with the minimum at  $|\phi| = \sqrt{-\frac{\mu^2}{\lambda}}$  rather than at  $|\phi| = 0$  as in the left-hand plot.

705 The VEV can be substituted back into the original Lagrangian in Equation 2.4, and, following  
 706 quite a bit of math, a collection of mass terms can be identified:

$$\mathcal{L} \subset \mathcal{L}_M \equiv \frac{1}{8} v^2 g^2 \left[ (W_\mu^1)^2 + (W_\mu^2)^2 \right] + \frac{1}{8} v^2 \left[ g^2 (W_\mu^3)^2 - 2gg' W_\mu^3 B^\mu + g'^2 (B_\mu)^2 \right] \quad (2.10)$$

<sup>707</sup> Focusing on the first term for the moment, substituting in Equation 2.2 for the physical  $W^\pm$  bosons,  
<sup>708</sup> the mass term can be seen clearly:

$$M_W^2 W^+ W^- = \left(\frac{1}{2} v g\right)^2 W^+ W^- \quad (2.11)$$

<sup>709</sup>

$$M_W = \frac{1}{2} v g \quad (2.12)$$

<sup>710</sup> With a bit of clever forward-thinking, the second term of Equation 2.10 can be rewritten as:

$$\frac{1}{8} v^2 \left[ g W_\mu^3 - g' B_\mu \right]^2 + 0 \left[ g' W_\mu^3 - g B_\mu \right]^2 = \frac{1}{2} M_Z^2 Z_\mu^2 + \frac{1}{2} M_A^2 A_\mu^2 \quad (2.13)$$

<sup>711</sup> where  $Z_\mu^2$  and  $A_\mu^2$  represent the physical  $Z$  boson and photon, respectively, and are defined as:

$$Z_\mu = \frac{g W_\mu^3 - g' B_\mu}{\sqrt{g^2 + g'^2}} \quad (2.14)$$

<sup>712</sup>

$$A_\mu = \frac{g' W_\mu^3 - g B_\mu}{\sqrt{g^2 + g'^2}} \quad (2.15)$$

<sup>713</sup> From this, it can be seen that the photon is massless, and the mass of the  $Z$  boson is identified as:

$$M_Z = \frac{1}{2} v \sqrt{g^2 + g'^2} \quad (2.16)$$

<sup>714</sup> Lastly, the Higgs field can couple directly to the fermions. Taking the electron as an example,  
<sup>715</sup> an additonal Lagrangian term can be written:

$$\mathcal{L}_e = -G_e [\bar{e}_L \phi e_R + \bar{e}_R \phi^\dagger e_L] \quad (2.17)$$

<sup>716</sup> where  $e_L$  and  $e_R$  are the left-handed doublet and right-handed singlet, respectively, and  $\phi$  is as in  
<sup>717</sup> Equation 2.3. The symmetry can be spontaneously broken by a perturbation about the VEV:

$$\phi = \sqrt{\frac{1}{2}} \begin{pmatrix} 0 \\ v + h(x) \end{pmatrix} \quad (2.18)$$

<sup>718</sup> which, when substituted into  $\mathcal{L}_e$  gives:

$$\begin{aligned} \mathcal{L}_e &= -\frac{G_e}{\sqrt{2}} v (\bar{e}_L e_R + \bar{e}_R e_L) - \frac{G_e}{\sqrt{2}} (\bar{e}_L e_R + \bar{e}_R e_L) h \\ &= -m_e \bar{e} e - \frac{m_e}{v} \bar{e} e h \end{aligned} \quad (2.19)$$

<sup>719</sup> for electron mass  $m_e = \frac{G_e v}{\sqrt{2}}$ . From the second term, it can be seen that the strength of the Higgs  
<sup>720</sup> coupling to the electron is proportional to the mass of the electron. The rest of the fermion couplings  
<sup>721</sup> follow from this example.

What is accomplished here is quite remarkable. The weak and electromagnetic interactions have been unified into a single  $SU(2) \times U(1)$  interaction, and the physical bosons observed in nature arise as mixtures of the four gauge fields. Three of the four degrees of freedom in the scalar field  $\phi$  of Equation 2.3, are absorbed by the  $W^\pm$  and  $Z$  bosons, and the fourth generates the Higgs boson. Additionally, it is shown that the Higgs couples to fermions in proportion to their mass. From experimental measurements, the value of the VEV has been determined to be  $v \approx 246$  GeV [19]. However, it should be noted that the theory does not predict the mass of the Higgs boson or of the fermions; these must all be determined from experiment.

### 2.3 Electroweak vector boson scattering

Due to the non-Abelian nature of the EWK interaction, the associated gauge bosons are allowed to self-interact. This results in triple and quartic couplings of gauge bosons (TGCs and QGCs, respectively). The SM allowed TGCs are the  $WW\gamma$  and  $WWZ$  vertices, which can be measured experimentally via diboson production or through vector boson fusion (VBF). QGCs predicted by the model include  $WWZ\gamma$ ,  $WW\gamma\gamma$ ,  $WWZZ$ , and  $WWWW$  vertices accessible in triboson production or via vector boson scattering (VBS)<sup>1</sup> [20]. VBS processes are defined by a  $VV \rightarrow VV$  signature, where  $V$  represents one of the EWK gauge bosons ( $W^\pm$ ,  $Z$ , or  $\gamma$ ), as shown in Figure 2.2. The actual interaction between the incoming and outgoing vector bosons can be mediated by the exchange of a virtual  $V$  or directly via a QGC (as in Figure 2.3), or by the exchange of a Higgs boson (as in Figure 2.4).

As detailed in the previous section, the Higgs mechanism produces three Goldstone bosons and a Higgs boson. The Goldstone bosons are then “eaten” by the physical gauge bosons, giving them mass and consequently a longitudinal polarization<sup>2</sup>. In fact, according to the Electroweak Equivalence Theorem, the high-energy interactions of longitudinal gauge bosons can be accurately described by the Goldstone bosons of the EWSB mechanism [21]. Thus, the scattering of the massive gauge bosons are inextricably linked to EWSB.

It turns out that without a light SM Higgs boson, the scattering amplitude of longitudinally polarized vector bosons grows with center-of-mass energy and ultimately violates unitarity above

---

<sup>1</sup>Vector boson fusion and scattering typically refer to the  $s$ -channel and  $t$ -channel exchanges of a vector boson, respectively. Since both deal with a similar  $VV \rightarrow VV$  process, for the remainder of this thesis, *vector boson scattering* will refer to both VBF and VBS.

<sup>2</sup>A massless spin-1 boson can have one of two transverse polarization states, while a massive spin-1 boson can also be longitudinally polarized. As a result, only the massive  $W^\pm$  and  $Z$  bosons, and not the massless photon, are sensitive to EWSB.

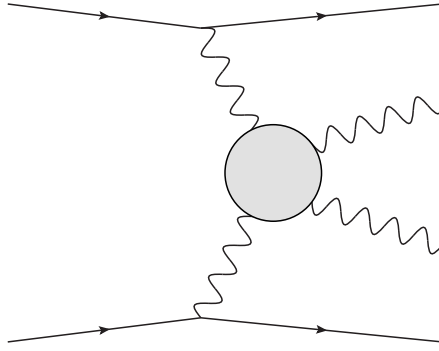


Figure 2.2: Feynman diagram of a generic VBS process. The gray circle represents any interaction with two incoming and two outgoing vector bosons, including any of the diagrams shown in Figures 2.3 and 2.4.

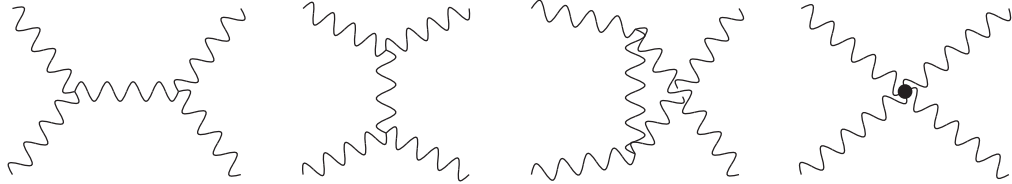


Figure 2.3: Leading order  $VV \rightarrow VV$  Feynman diagrams involving EWK bosons. From left to right:  $s$ -channel,  $t$ -channel,  $u$ -channel, and the quartic gauge coupling.

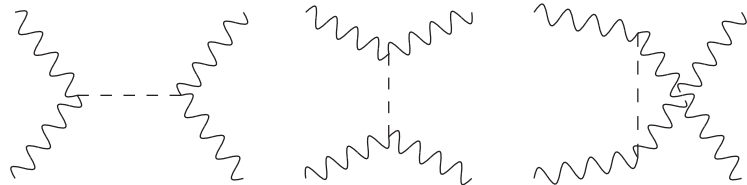


Figure 2.4: Leading order  $VV \rightarrow VV$  Feynman diagrams involving the exchange of a Higgs boson. From left to right:  $s$ -channel,  $t$ -channel, and  $u$ -channel.

<sup>749</sup>  $\sqrt{s} \approx 1.2$  TeV [22, 23]. Writing down the equations for the transverse and longitudinal polarization  
<sup>750</sup> vectors for a gauge boson of mass  $M_V$  [24]:

$$\epsilon_{\pm}^{\mu} = \frac{1}{\sqrt{2}}(0, 0, \pm i, 0) \quad (2.20)$$

<sup>751</sup>

$$\begin{aligned} \epsilon_L^{\mu} &= \frac{1}{M_V}(|\vec{p}|, 0, 0, E) \\ &= \frac{p^{\mu}}{M_V} + v^{\mu} \end{aligned} \quad (2.21)$$

<sup>752</sup> where  $v^{\mu}$  is of the order  $M_V/E$  and becomes small in the high energy limit, it can be seen that

753  $\epsilon_L^\mu$  grows with the momentum of the boson  $p^\mu$ . Therefore, the dominant contribution to the VBS  
754 process at high energy comes from the longitudinally polarized gauge bosons [25].

755 The high-energy behavior of longitudinally polarized vector boson scattering can be explored in  
756 the case of opposite-sign  $W^+W^- \rightarrow W^+W^-$  scattering. In the high-energy limit ( $s \gg M_W^2, M_H^2$ ),  
757 the amplitude of  $W^+W^-$  scattering without considering the Higgs contributions (the relevant dia-  
758 grams in Figure 2.3) can be written as [23]:

$$\mathcal{M}_{\text{gauge}} = -\frac{g^2}{4M_W^2}u + \mathcal{O}\left(\left[\frac{E}{M_W}\right]^0\right) \quad (2.22)$$

759 where  $g$  is the EWK coupling and  $u$  is one of the Mandelstam variables (the others being  $s$  and  
760  $t$ ). The  $\mathcal{O}(E^4)$  terms cancel out between the TGC and QGC diagrams [25]. What is left is an  
761 amplitude proportional to  $E^2$  that diverges as  $E/M_W \rightarrow \infty$ . However, the amplitude from the  
762 diagrams involving the Higgs boson (the relevant diagrams in Figure 2.4) is:

$$\mathcal{M}_{\text{Higgs}} = -\frac{g^2}{4M_W^2} \left[ \frac{(s - M_W^2)^2}{s - m_H^2} + \frac{(t - M_W^2)^2}{t - M_H^2} \right] \quad (2.23)$$

763 which, in the high-energy limit, reduces to:

$$\mathcal{M}_{\text{Higgs}} = \frac{g^2}{4M_W^2}u + \mathcal{O}\left(\left[\frac{E}{M_W}\right]^0\right) \quad (2.24)$$

764 Adding the two equations together cancels out the  $E^2$  term and leaves only terms constant in  
765 energy. Therefore, with a SM Higgs, the scattering amplitude for longitudinally polarized  $W$  bosons  
766 no longer diverges. Plots of the cross section of several  $VV \rightarrow VV$  scattering processes are shown  
767 in Figure 2.5 with and without a SM Higgs boson.

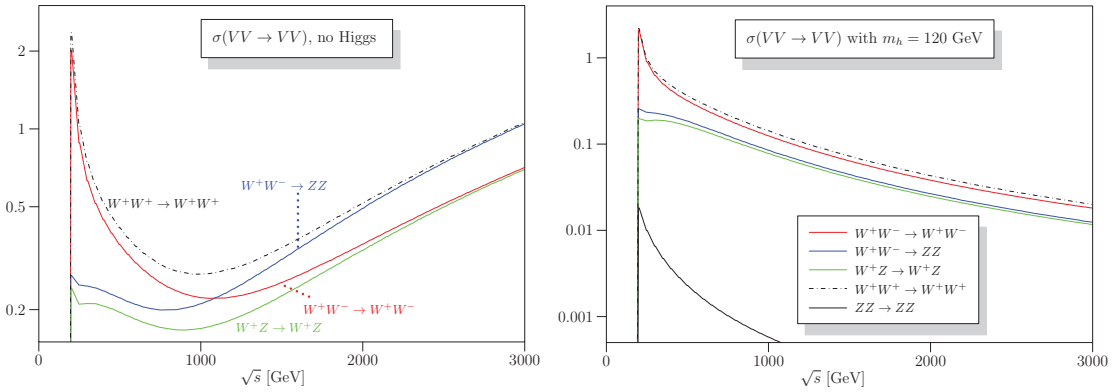


Figure 2.5: Cross sections in nanobarns for five different longitudinally polarized VBS processes as a function of center of mass energy  $\sqrt{s}$ . Without a Higgs boson (left), the cross sections grow unbounded with  $\sqrt{s}$ . With a 120 GeV Higgs boson (right), the cross sections no longer diverge. Plots taken from [26].

768

## CHAPTER 3

769

# LHC and the ATLAS Detector

770 **3.1 The Large Hadron Collider**

771 The Large Hadron Collider (LHC) [27] is...

772 **3.2 The ATLAS Detector**

773 ATLAS is a general-purpose particle detector...

774 **3.2.1 The Inner Detector**

775 The Inner Detector serves the primary purpose of measuring the trajectories of charged particles...

776 **3.2.1.1 Pixel Detector**

777 The Pixel detector consists of four cylindrical barrel layers and three disk-shaped endcap layers...

778 **3.2.1.2 Semiconductor Tracker**

779 The Semiconductor Tracker uses the same basic technology as the Pixels, but the fundamental unit  
780 of silicon is a larger “strip”...

781 **3.2.1.3 Transition Radiation Tracker**

782 The Transition Radiation Tracker is the outermost component of the ID...

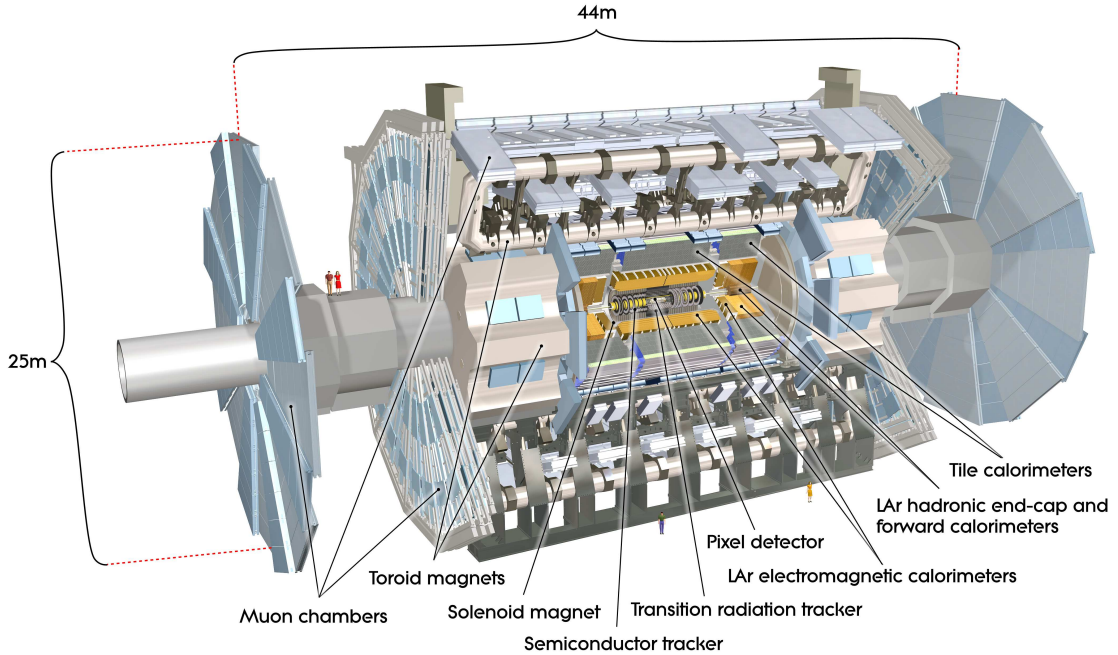


Figure 3.1: General cut-away view of the ATLAS detector [28].

### 783 3.2.2 The Calorimeters

784 ATLAS includes two types of calorimeter system for measuring electromagnetic and hadronic showers.  
 785 These are the Liquid Argon (LAr) calorimeters and the Tile calorimeters. Together, these cover  
 786 the region with  $|\eta| < 4.9\dots$

#### 787 3.2.2.1 Liquid Argon Calorimeters

788 The Liquid Argon system consists of...

#### 789 3.2.2.2 Tile Calorimeters

790 The Tile calorimeter provides coverage for hadronic showers...

### 791 3.2.3 The Muon Spectrometer

792 Muon spectrometer stuff.

<sup>793</sup> **3.2.4 Particle reconstruction**

<sup>794</sup> Particle reconstruction algorithms

<sup>795</sup> **3.2.4.1 Track reconstruction**

<sup>796</sup> **3.2.4.2 Muon reconstruction**

<sup>797</sup> **3.2.4.3 Electron reconstruction**

<sup>798</sup> **3.2.4.4 Jet reconstruction**

## CHAPTER 4

---

# 800 Alignment of the ATLAS Inner Detector

---

801 When a charged particle passes through the ATLAS ID, it leaves hits in the sensors along its path.  
802 In order to accurately measure the track of the particle, it is necessary to know where these hits  
803 occurred as precisely as possible, which in turn requires knowledge of the physical location of the  
804 element that registered the hit. If one of these elements is *misaligned*, or displaced relative to its  
805 position in the known detector geometry, the assumed location of the corresponding hit will not  
806 match its actual location, resulting in an incorrect track fit. These misalignments can occur for  
807 any number of reasons, including but not limited to elements shifting during maintenance periods  
808 or cycles in ATLAS's magnetic field, or small movements during normal detector operations. The  
809 effect of a misaligned detector element on the track reconstruction is shown in Figure 4.1.

810 In order to correct the misalignments, the ID alignment procedure is applied to accurately  
811 determine the physical position and orientation of each detector element. The baseline accuracy of  
812 the alignment is required to be such that the track parameter resolutions are not degraded by more  
813 than 20% with respect to those derived from a perfect detector geometry<sup>3</sup>. This corresponds to a  
814 precision of better than  $10\mu\text{m}$  in the positioning of the elements of the silicon detectors [29].

815 This chapter outlines the ID alignment procedure, the alignment of the detector during the 2015  
816 data taking period, and the steps taken to measure momentum biases in the alignment.

---

<sup>3</sup>The so-called *perfect geometry* refers to the description of the ATLAS detector in which every sensor precisely matches its design specifications. The perfect geometry contains no misalignments, and the position of each sensor is known exactly.

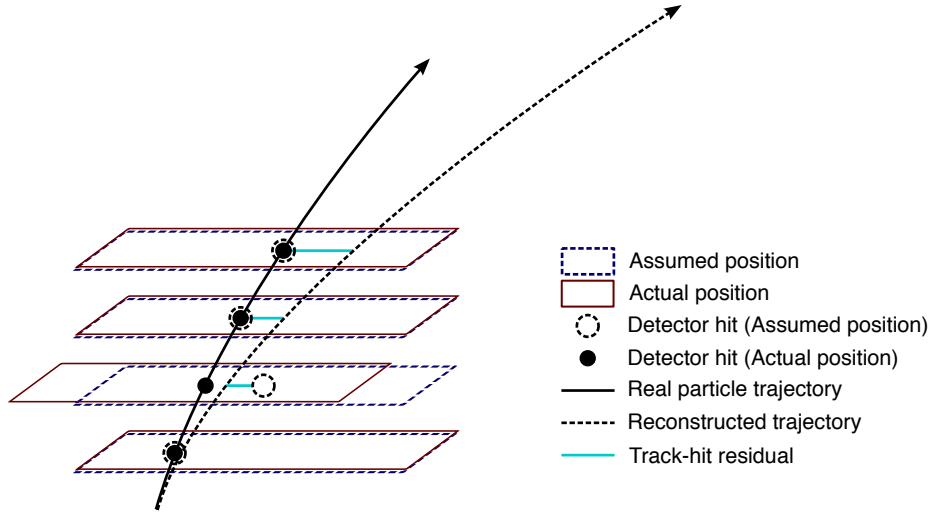


Figure 4.1: Graphical representation of the effect of a misaligned detector element. The reconstructed particle track (dashed arrow) differs from the actual trajectory of the particle (solid arrow) due to the shift in one of the detector elements. The cyan lines represent the track-to-hit residuals.

## 817 4.1 The alignment method

818 The alignment procedure uses track-based algorithm that updates the locations of detector elements  
 819 in order to minimize the set of track-hit *residuals*. These residuals are defined as the distance between  
 820 the fitted track position in a given detector element to the position of the hit recorded by the same  
 821 element, and are shown by the cyan lines in Figure 4.1. Tracks in ATLAS are parameterized as  
 822 five-dimensional vectors [30]:

$$\vec{\tau} = (d_0, z_0, \phi_0, \theta, q/p) \quad (4.1)$$

823 where  $d_0$  and  $z_0$  are the transverse and longitudinal impact parameters with respect to the origin,  
 824 respectively,  $\phi_0$  is the azimuthal angle of the track at the point of closest approach to the origin,  $\theta$   
 825 is the polar angle, and  $q/p$  is the charge of the track divided by its momentum. The residual for the  
 826  $i^{\text{th}}$  hit of a given track can then be written in terms of the track parameters  $\vec{\tau}$  and a set of alignment  
 827 parameters  $\vec{a}$  that describe the hit location [31]:

$$r_i(\vec{\tau}, \vec{a}) = (\vec{m}_i - \vec{e}_i(\vec{\tau}, \vec{a})) \cdot \hat{k} \quad (4.2)$$

828 where  $\vec{e}_i$  is the intersection point of the extrapolated track with the sensor,  $\vec{m}_i$  is the position of the  
 829 associated hit within the sensor, and  $\hat{k}$  is the unit vector defining the direction of the measurement  
 830 within the sensor.  $\vec{r}$  is then the vector of residuals for the given track.

831 A  $\chi^2$  function can be built from the residuals of all collected tracks:

$$\chi^2 = \sum_{\text{tracks}} \vec{r}^T V^{-1} \vec{r} \quad (4.3)$$

832 where  $V$  is the covariance matrix of the hit measurements. The  $\chi^2$  function is then minimized with  
833 respect to the alignment parameters  $\vec{a}$ , which contain all degrees of freedom being aligned. The  
834 minimization condition with respect to  $\vec{a}$  is:

$$\frac{d\chi^2}{d\vec{a}} = 0 \rightarrow 2 \sum_{\text{tracks}} \left( \frac{d\vec{r}}{d\vec{a}} \right)^T V^{-1} \vec{r} = 0 \quad (4.4)$$

835 This equation can be difficult to solve exactly, so the residual is rewritten as a first order Taylor  
836 expansion:

$$\vec{r} = \vec{r}_0 + \frac{d\vec{r}}{d\vec{a}} \delta\vec{a} \quad (4.5)$$

837 where  $\vec{r}_0$  is dependent on an initial set of track and alignment parameters  $\vec{r}_0$  and  $\vec{a}_0$ , respectively;  
838 the track parameter dependence has also been folded into the total derivative  $\frac{d\vec{r}}{d\vec{a}}$ . Equation 4.5 can  
839 then be inserted into the minimization condition from Equation 4.4 to give:

$$\left[ \sum_{\text{tracks}} \left( \frac{d\vec{r}}{d\vec{a}} \right)^T V^{-1} \left( \frac{d\vec{r}}{d\vec{a}} \right) \right] \delta\vec{a} + \sum_{\text{tracks}} \left( \frac{d\vec{r}}{d\vec{a}} \right)^T V^{-1} \vec{r}_0 = 0 \quad (4.6)$$

840 From this equation, the alignment matrix  $\mathcal{M}_a$  and alignment vector  $\vec{\nu}_a$  can be defined:

$$\mathcal{M}_a = \sum_{\text{tracks}} \left( \frac{d\vec{r}}{d\vec{a}} \right)^T V^{-1} \left( \frac{d\vec{r}}{d\vec{a}} \right) \quad (4.7)$$

841

$$\vec{\nu}_a = \sum_{\text{tracks}} \left( \frac{d\vec{r}}{d\vec{a}} \right)^T V^{-1} \vec{r}_0 \quad (4.8)$$

842 Finally, the alignment corrections  $\delta\vec{a}$  can be solved for by inverting the alignment matrix:

$$\delta\vec{a} = -\mathcal{M}_a^{-1} \vec{\nu}_a \quad (4.9)$$

843 which is a linear system of equations with a number of equations equal to the number of alignment  
844 degrees of freedom [32].

845 Inverting the matrix and solving this system of equations is referred to as *Global  $\chi^2$*  align-  
846 ment [31]. This can be useful, as  $\mathcal{M}_a$  contains all the correlations between the alignable structures.  
847 However, inverting the matrix becomes difficult when the number of degrees of freedom becomes  
848 large, and as the number of alignable structures increases, so too does the size of the matrix  $\mathcal{M}_a$ .  
849 Eventually inverting the matrix becomes too computationally intensive to be practical.

850 This problem is solved by the *Local*  $\chi^2$  algorithm [33]. In this case, the alignment matrix is  
 851 constructed to be block-diagonal, allowing for it to be inverted even for large numbers of degrees of  
 852 freedom. This is achieved by replacing the full derivative in Equation 4.6 with the partial derivative  
 853  $\frac{\partial \vec{r}}{\partial \vec{a}}$ . The new alignment matrix  $\mathcal{M}'_a$  and alignment vector  $\vec{\nu}'_a$  become:

$$\mathcal{M}_a = \sum_{\text{tracks}} \left( \frac{\partial \vec{r}}{\partial \vec{a}} \right)^T V^{-1} \left( \frac{\partial \vec{r}}{\partial \vec{a}} \right) \quad (4.10)$$

854

$$\vec{\nu}_a = \sum_{\text{tracks}} \left( \frac{\partial \vec{r}}{\partial \vec{a}} \right)^T V^{-1} \vec{r}_0 \quad (4.11)$$

855 Inverting  $\mathcal{M}'_a$  is considerably faster and less intensive even for large numbers of degrees of freedom;  
 856 however, the correlations between the alignable structures is lost.

857 Due to the Taylor expansion used in Equation 4.6, several iterations of the alignment algorithm  
 858 may be necessary to converge on a final set of alignment constants. The Local  $\chi^2$  alignment typically  
 859 requires more iterations due to the loss of the correlation information [34]. In practice, the ATLAS  
 860 reconstruction is run over a set of events, and the resulting tracks are fed to the alignment algorithm.  
 861 The residuals are calculated, the alignment matrix is built and inverted, and a new set of alignment  
 862 constants is obtained. The convergence of the alignment can be checked by:

863 1. Measure the  $\Delta\chi^2$  with the previous iteration. If it is near zero, then the  $\chi^2$  is approaching its  
 864 minimum.

865 2. Looking at the residual distributions for different alignable structures. A well aligned detector  
 866 will have a mean residual of zero with a width approximating the intrinsic resolution of the  
 867 detector.

868 If the above checks are satisfied, the process is finished and the final alignment constants are read  
 869 out; if not, another iteration is performed. A visual representation of the alignment chain is shown  
 870 in Figure 4.2.

871 Since a  $\chi^2$  minimization is used to align the detector, if there is a systematic misalignments in  
 872 the detector that does not adversely affect the  $\chi^2$ , the algorithm will be insensitive to it. These  
 873 misalignments are referred to as *weak modes*, and special care is taken to remove them [35]. One  
 874 potential impact of weak modes is a bias in the track momentum of reconstructed particles. This  
 875 particular effect is the subject of Section 4.4.

876 In practice, the detector is aligned both in “real-time” as data is collected, and during dedicated  
 877 offline alignment campaigns. The real-time alignment is run in ATLAS’s so-called *calibration loop*,

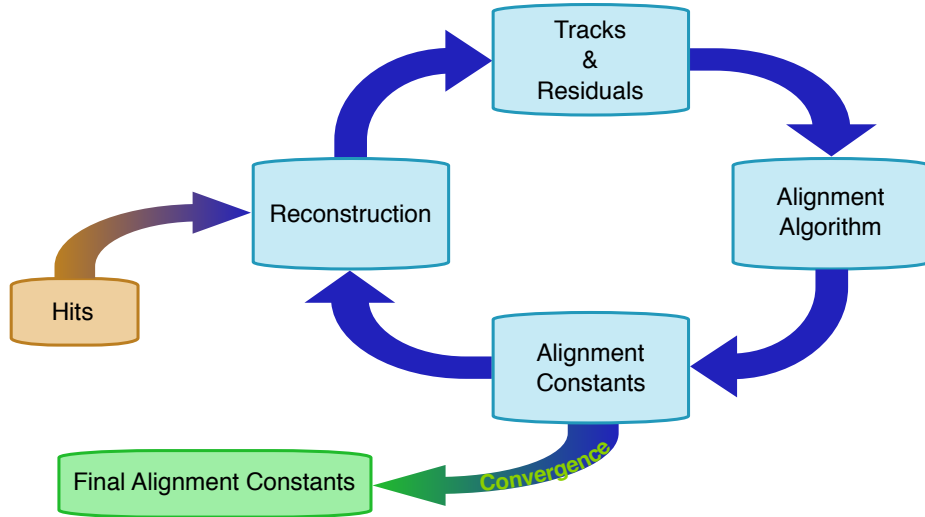


Figure 4.2: Graphical representation of the ID alignment chain.

which comprises the first stage in the preparation of data for physics analysis. The calibration loop requires the alignment as well as various other detector calibrations to be available within 48 hours for initial data processing. A fast, coarse-grained alignment<sup>4</sup> is run on a subset of the available data containing full tracking information, and the results are propagated to the reconstruction of that particular run [36]. Due to the time constraints of the calibration loop, a full sensor-by-sensor alignment is not possible.

The more thorough and finely tuned alignments are reserved for the dedicated alignment campaigns. These generally occur early in data taking campaigns, typically once a sufficient amount of data is collected after a detector shutdown, in order to obtain a good baseline alignment for use in the remainder of the data collection period. Once data taking is complete, another campaign determines an improved set of alignment constants (divided into several “blocks” to account for time-dependent misalignments), and the full data is reprocessed using the newly derived detector geometry. The initial offline alignment of the ATLAS detector at the beginning of Run 2 in 2015 is the subject of Section 4.2.

### 4.1.1 Alignment levels

The alignment of the detector is performed at several levels of increasing granularity. This adds flexibility in being able to align only as finely as needed, and it also allows for global, detector-level

<sup>4</sup>The calibration loop runs up to a Level 2 alignment in the silicon detectors, which involves treating each layer of sensors as a single object, defined in greater detail in Table 4.1.

895 misalignments to be corrected first before dealing with finer adjustments.

- 896     ● Level 1 (L1) alignment involves moving entire subdetector components as a single unit, such  
897         as the entire Pixel detector, or the SCT barrel. These often have the largest misalignments,  
898         but they are easily corrected and do not require large volumes of data to do so.
- 899     ● Level 2 (L2) alignment treats individual layers in the silicon detectors (modules in the TRT)  
900         and end cap disks as individual alignable objects.
- 901     ● Level 2.7 (L27) alignment was introduced with the addition of the IBL to the ID in Run 2. It  
902         involves the stave-by-stave alignment of the IBL and Pixel barrel<sup>5</sup>.
- 903     ● Level 3 (L3) alignment treats each sensor in the silicon detectors and each straw in the TRT  
904         as an individual alignable object. It is the finest grained alignment available but also the most  
905         computationally intensive due to the large number of degrees of freedom. The large number  
906         of individual detector sensors being aligned also requires the largest amount of statistics.

907 The different alignment levels are listed in more detail in Table 4.1, including the number of alignable  
908 structures and associated degrees of freedom for each detector component.

909     The implementation of the alignment algorithm in the software is flexible enough to allow each  
910     subsystem to be aligned individually at a specified level. Each alignable structure has six degrees of  
911     freedom: 3 translations ( $T_x, T_y, T_z$ ) and 3 rotations ( $R_x, R_y, R_z$ )<sup>6</sup>; however individual degrees of  
912     freedom may be turned on and off as required. In a typical alignment job, L1 and L2 contain few  
913     enough degrees of freedom that the Global  $\chi^2$  algorithm can be used, but L3 alignments (which can  
914     contain over 36,000 degrees of freedom in the silicon detectors alone) require the Local  $\chi^2$  algorithm.

#### 915 4.1.2 Alignment coordinate systems

916 The global coordinate system ( $x, y, z$ ) used by the ID alignment matches that of the ATLAS detector  
917 in general. The positions and orientations of individual detector modules of the ID are defined by  
918 a right-handed local coordinate system ( $x', y', z'$ ) where the origin is defined as the geometrical  
919 center of the module. The  $x'$ -axis for each silicon module is defined to point along the most sensitive  
920 direction of the module, the  $y'$ -axis is oriented along the long side of the module, and the  $z'$ -axis is

---

<sup>5</sup>For the purposes of this Chapter, the term “Pixel” will refer to the original three layers of the Pixel detector, and the IBL will be referenced separately.

<sup>6</sup>The TRT is an exception, as the subdetector does not have any resolution along the length of the straw. Therefore, for the barrel,  $T_z$  is omitted. Similarly for the straws themselves, only two parameters are defined: translation with respect to the radial direction ( $T_\phi$ ) and rotation with respect to the radial axis ( $R_r$  for the barrel and  $R_z$  for the end-caps) [37].

Level	Description of alignable structure	Structures	DoF
1	IBL detector	1	6
	Whole Pixel detector	1	6
	SCT barrel and 2 end-caps	3	18
	TRT barrel and 2 end-caps ( $T_z$ fixed)	3	17
Total:		8	47
2	IBL detector	1	6
	Pixel barrel layers	3	18
	Pixel end-cap disks	$2 \times 3$	36
	SCT barrel layers	4	24
	SCT end-cap disks	$2 \times 9$	108
	TRT barrel 32 modules ( $T_z$ fixed)	$3 \times 32$	480
	TRT end-cap wheels	$2 \times 40$	480
Total:		208	792
2.7	IBL staves	14	84
	Pixel barrel staves	$22+38+52$	672
	Pixel end-cap disks	$2 \times 3$	18
	Total:		132
3	IBL modules	280	1,680
	Pixel modules	1,744	10,464
	SCT modules	4,088	24,528
	TRT barrel wires ( $T_\phi, R_r$ only)	105,088	210,176
	TRT end-cap wires ( $T_\phi, R_Z$ only)	245,760	491,520
	Total silicon sensors:		6,112
	Total TRT wires:		350,848
Total:		36,672	701,696

Table 4.1: The four alignment levels for each of the detector subsystems. The total number of alignable structures and degrees of freedom (DoF) to be aligned are given for each level.

921 orthogonal to the  $(x', y')$  plane. For the TRT straws, the  $x'$ -axis is perpendicular to both the wire  
 922 and the radial direction, defined from the origin of the global frame to the straw center, the  $y'$ -axis  
 923 points along the straw, and once again the  $z'$ -axis is orthogonal to the  $(x', y')$  plane. A depiction of  
 924 the global and local coordinate systems for the ID is shown in Figure 4.3.

925 When considering the alignment degrees of freedom listed earlier in Section 4.1.1, grouped collec-  
 926 tions of modules, layers, or entire subdetectors use the global coordinate system; individual modules  
 927 use their respective local coordinate systems. The translations  $T_i$  are with respect to the origin of  
 928 the given reference frame, and the rotations  $R_i$  are taken about the Cartesian axes.

## 929 4.2 Early 2015 alignment of the ATLAS detector

930 At the end of Run 1, the LHC was shut down for upgrades and maintenance. During this time,  
 931 a number of upgrades were performed on the ATLAS detector, including the installation of a new

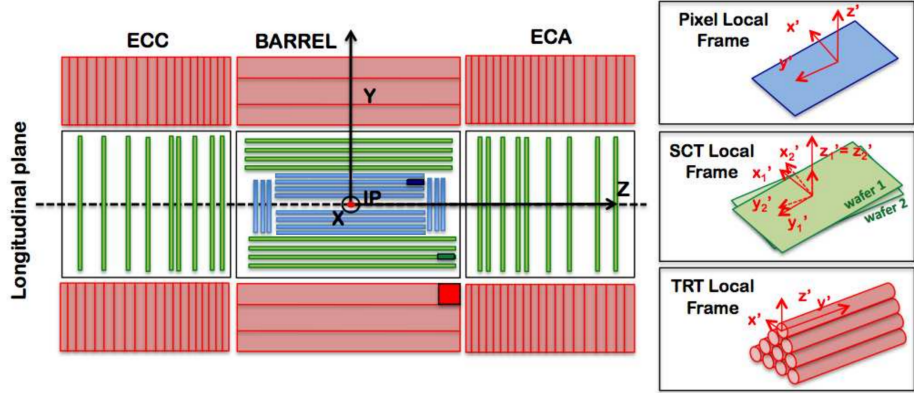


Figure 4.3: A schematic representation of the Inner Detector in the longitudinal plane with the global coordinate system overlaid on top. The Pixel detector and IBL are shown in blue, the SCT in green, and the TRT in red. The local coordinates for each subdetector module are inset on the right. Image taken from [38].

932 innermost layer of the Pixel detector, the Insertable B-Layer (IBL) [39]. TODO: This will certainly  
 933 be defined in the detector description, so maybe the citation and abbreviation are not needed These  
 934 changes to the ID required some detector components to be removed temporarily, and many elements  
 935 shifted relative to each other over the course of the maintenance process. In order to correct for these  
 936 large detector movements prior to  $\sqrt{s} = 13$  TeV collision data taking, an alignment was performed  
 937 using cosmic ray data collected in early 2015 [38]. This alignment was able to correct for the majority  
 938 of the large detector-wide misalignments as well as determine the global position of the IBL at the  
 939 micron level.

940 In June of 2015, shortly after the data taking period began, the first track-based alignment  
 941 of the refurbished ID was performed using  $\mathcal{L} = 7.9 \text{ pb}^{-1}$  of  $\sqrt{s} = 13$  TeV  $pp$  collision data [40].  
 942 Starting from the initial geometry determined by the cosmic ray alignment, referred to hereafter  
 943 as the *March alignment*, an improved set of alignment constants, called the *June alignment*, was  
 944 derived from a data set of approximately 1.4 million selected tracks. For comparison, a MC sample  
 945 containing approximately 2.7 million tracks was constructed from dijet events simulated using a  
 946 perfect detector geometry; the MC events are reweighted to match the  $\eta$  and  $p_T$  distributions found  
 947 in the data. Additional validation of the alignment results uses a set of cosmic ray data collected  
 948 by the detector during the LHC collisions.

---

**949 4.2.1 June alignment procedure**

950 The data set used as the input for the alignment contains a subset of physics events used for prompt  
 951 reconstruction recorded at a rate of 10 Hz. To ensure that only high quality tracks are used for the  
 952 alignment, each track is required to have transverse momentum  $p_T > 3$  GeV, contain at least one  
 953 hit in the Pixel detector, at least seven hits in the combined silicon detectors, and at least 25 hits  
 954 in the TRT.

955 A full L3 alignment of the IBL was included in the March alignment; however, a realignment  
 956 was necessary. Since the cosmic rays pass through the detector top-down, the staves on the sides of  
 957 the IBL could not be aligned as precisely as those on the top and bottom due to lower statistics.  
 958 Additionally, the IBL was operating at a temperature of  $-20^\circ\text{C}$  during the cosmic data taking  
 959 and at  $-10^\circ\text{C}$  for collision data taking. This proved to be significant, as it was observed that  
 960 the IBL staves experience a temperature-dependent, parabolic bowing in the local  $x'$ -direction of  
 961 approximately  $-10\mu\text{m/K}$  [41]. As a result, a full L3 alignment of the IBL was essential in order to  
 962 correct for the bowing. Due to it being a brand new element of the detector as well as its importance  
 963 in vertexing and  $b$  jet tagging, aligning the IBL sensors with a high degree of precision was of great  
 964 importance.

965 The June alignment was performed in two stages, with the first pass focusing on relative move-  
 966 ments of the big structures and correcting for the bowing of the IBL. The March alignment corrected  
 967 for these larger movements as well; however, it was observed during Run 1 that these sort of mis-  
 968 alignments are introduced by changing conditions in the detector [35], such as in the cooling system  
 969 or magnet power cycling, which may have occurred between the early cosmic data taking and the  
 970 first  $\sqrt{s} = 13$  TeV collisions. The silicon detectors were aligned at several different levels and the  
 971 IBL was aligned at the module level; the TRT detector was kept fixed to act as a global reference  
 972 frame. The full alignment chain for the first pass consisted of the following steps:

- 973 1. The IBL, Pixel, and SCT detectors were aligned at L1. The SCT barrel was not aligned in  
 974  $T_z$  in order to constrain global displacements along the  $z$ -axis, as the TRT is not sensitive to  
 975 that degree of freedom.
- 976 2. The IBL, and Pixel barrel and end-caps, and SCT barrel were aligned at L2. The SCT end-caps  
 977 were aligned at L1.
- 978 3. The IBL and pixel barrel were aligned at L27, using all six degrees of freedom. The Pixel  
 979 end-cap disks were only aligned in the plane ( $T_x$ ,  $T_y$ , and  $R_z$ ). The SCT was treated the same

980 as in the previous step.

981 4. The IBL was aligned at L3 using all six degrees of freedom for each module.

982 The primary goal for the second pass was to remove a bias in the transverse impact parameter  
 983  $d_0$  present in the March alignment. The resolution of  $d_0$  was also poorer than expected. In order  
 984 to correct for this, an additional constraint was passed to the alignment by adding an impact  
 985 parameter with respect to the beam spot as a pseudo-measurement [42]. When the alignment  
 986 algorithm minimizes the  $\chi^2$ , it will take care of the impact parameter minimization as well. Only  
 987 the IBL and Pixel detectors were aligned in this step. The stages of the second pass are listed below,  
 988 and the beam spot constraint was used in each:

989 1. The IBL and Pixel detectors were aligned at L2 with the SCT fixed.

990 2. The IBL was aligned at L27

991 3. The IBL and Pixel barrel and end-caps were aligned at L3.

992 The set of alignment constants obtained at the end of the second pass represents the June alignment.

993 The highest level of alignment over the course of the two passes for each subdetector is listed in  
 994 Table 4.2.

Detector	Highest level of alignment
IBL	L3
Pixel	Barrel
	End-caps
SCT	Barrel
	End-caps
TRT	None

Table 4.2: Summary of the highest level of alignment applied to each ID subsystem when deriving the June alignment.

### 995 4.2.2 Alignment results

996 The primary measure of alignment quality is assessed by looking at the track-hit residual distri-  
 997 butions. If the detector is well aligned, the residuals will be Gaussian-distributed with a mean  
 998 of zero and a width approximating the detector's resolution. The residual distributions are con-  
 999 structed from the same selection of tracks that were used to perform the alignment, and are the  
 1000 focus of Section 4.2.2.1. A second check on the alignment involves observables sensitive to the track

parameter resolution. In this case, cosmic rays are used, making use of a “split track” technique that takes advantage of the top-to-bottom cosmic ray trajectory (compared to the center-out trajectory of collision tracks). This method and the corresponding tests of the alignment are detailed in Section 4.2.2.2

Additionally, the effect of the beam spot constrained alignment on the impact parameter  $d_0$  needs to be checked. The  $d_0$  distributions for both the March and June alignments are compared to the MC simulation using a perfect geometry in Figure 4.4. In the March alignment, there is a bias of 18  $\mu\text{m}$  in the mean of the distribution and the width is nearly twice that of the perfect geometry. After the second pass of the June alignment, the mean has shifted to 1  $\mu\text{m}$  and the distribution has narrowed considerably. From this, it appears that the constrained alignment successfully removed the  $d_0$  bias.

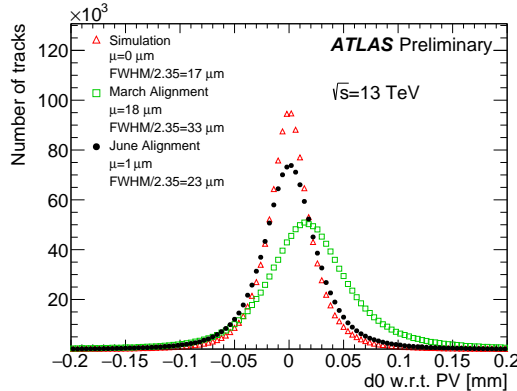


Figure 4.4: The  $d_0$  distributions with respect to the reconstructed primary vertex using the  $\sqrt{s} = 13$  TeV collision data sample reconstructed using the June (black) and March (green) alignments. The data is compared to a MC simulation using a perfect detector geometry (red). The distributions are normalized to the same number of entries.

#### 4.2.2.1 Residual distributions from collisions

As mentioned previously, the primary focus of the June alignment campaign was on the IBL and the Pixel detectors. The detectors are the closest to the beam line and have the finest resolutions of the ID subdetectors. The residual distributions in local  $x$  and  $y$  of the IBL planar sensors<sup>7</sup> are shown in Figure 4.5. These and subsequent figures in this section compare the June and March alignments to the perfectly-aligned MC simulation. Noticeable improvement in the distribution widths can be

<sup>7</sup>The IBL contains 12 planar sensors in the center of a stave, with four 3D sensors on either end. Only the planar sensors are shown here due to low statistics in the 3D sensors as well as poor MC modeling of these sensors.

seen in both the local  $x$ - and  $y$ -directions, nearly matching the simulation in local  $x$ , which is the most sensitive direction.

Due to the temperature-dependent bowing of the IBL, it is also interesting to look at the means of the residual distributions for each ring of IBL sensors along the beam line, as shown in Figure 4.6. A deformation is clearly visible in the March alignment in both measurement directions, and the shape in the local  $x$ -direction is consistent with an average stave bowing due to the different operating temperature of the IBL during the March alignment and the 13 TeV collisions. This feature was nearly eliminated in both directions through the L3 alignment of the IBL sensors.

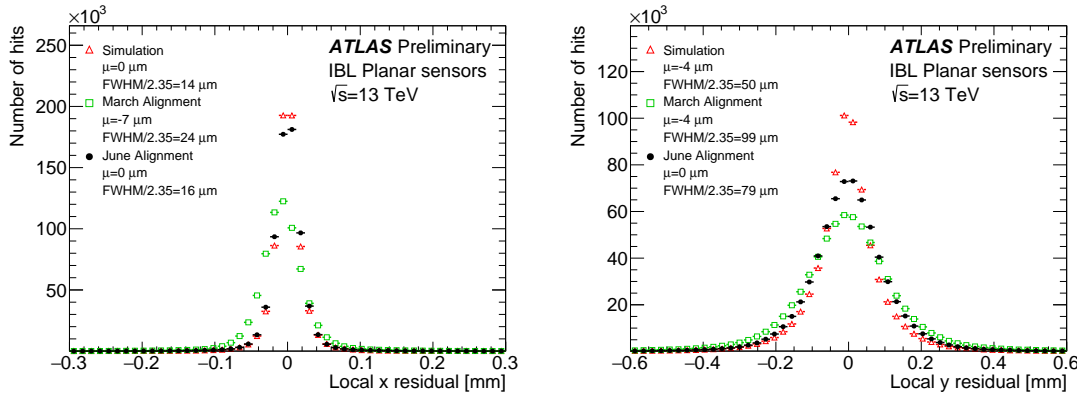


Figure 4.5: Local  $x$  (left) and local  $y$  (right) residual distributions of the IBL planar sensors using the  $\sqrt{s} = 13$  TeV collision data sample reconstructed using the June (black) and March (green) alignments. The data is compared to a MC simulation using a perfect detector geometry (red). The distributions are normalized to the same number of entries.

The local  $x$  and  $y$  residual distributions for the Pixel detector barrel and end-caps are shown in Figure 4.7. Even though the IBL is not included in the plots of the barrel, some of the noticeable improvement in the more sensitive local  $x$  direction is an effect of the improved IBL alignment. Similarly, the relatively broad local  $y$  residual distribution in the barrel likely indicates that further refinement of the IBL alignment was needed along that direction. Even so, the June alignment outperforms the March alignment and rivals the simulation in most of the plots.

Similar distributions for the SCT and TRT barrel and end-caps are shown in Figures 4.8 and 4.9, respectively. Much like with the Pixel residuals, there is a reduction in the width of the TRT residuals between the March and June alignments due to the alignment of the other subdetectors improving the quality of the track fit. Even though neither subdetector was aligned at module-level, the residuals indicate that the previous L3 alignment performed in Run 1 has not degraded

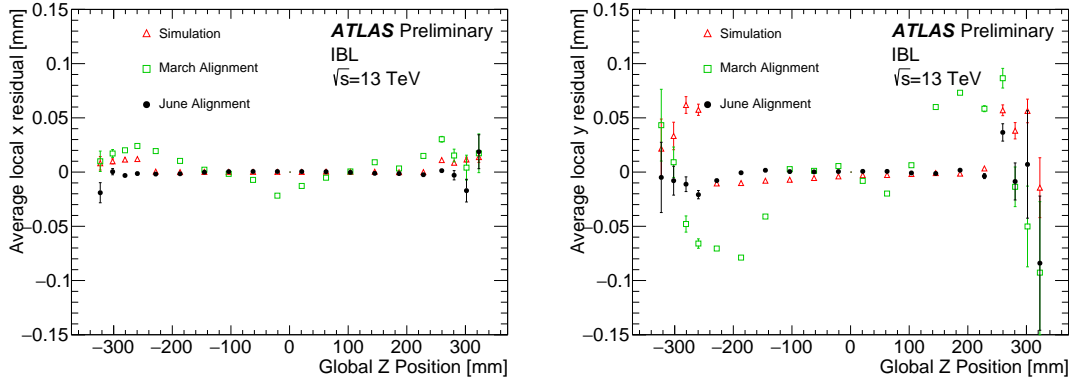


Figure 4.6: The mean of the local  $x$  (left) and local  $y$  (right) residual distributions as a function of the global  $z$  position of each IBL module using the  $\sqrt{s} = 13$  TeV collision data sample reconstructed using the June (black) and March (green) alignments. The data is compared to a MC simulation using a perfect detector geometry (red).

1037 significantly during the upgrade and maintenance period.

#### 1038 4.2.2.2 Track parameter resolution from cosmic rays

1039 Cosmic ray data is very useful as an independent check on the alignment in the barrel of the  
 1040 detector. While tracks from  $pp$  collisions originate within the detector and travel outwards, a cosmic  
 1041 ray that passes through the center of the detector leaves a track in both halves of the detector.  
 1042 If the cosmic ray is split in half, as in Figure 4.10, then it can be treated as two separate tracks  
 1043 each with nearly identical track parameters (some differences arise due to energy loss as the particle  
 1044 passes through the detector). The distribution of the difference in a given track parameter  $\Delta\tau$  is  
 1045 approximately Gaussian with a variance  $\sigma^2(\Delta\tau)$ . Since both tracks come from the same particle,  
 1046 each track individually has a variance equal to  $\sigma^2(\Delta\tau)/2$ . The resolution of the track parameter is  
 1047 then given by the root mean square of the distribution divided by  $\sqrt{2}$ .

1048 Cosmic rays whose split tracks each had transverse momentum  $p_T > 2$  GeV and at least one,  
 1049 eight, and 25 hits in the barrels of the Pixel, SCT, and TRT detectors, respectively, were selected to  
 1050 measure a collection of track parameters. Figure 4.11 shows the difference in the impact parameter  
 1051  $\Delta d_0$  and the charge divided by the transverse momentum  $\Delta q/p_T$  of the selected split-track cosmic  
 1052 rays for both the March and June alignments. Both distributions show a reduction in width in the  
 1053 June alignment, corresponding to an improvement in the resolution of each track parameter. The  
 1054  $\Delta d_0$  plot shows a significant improvement in the June alignment, further validating the removal of

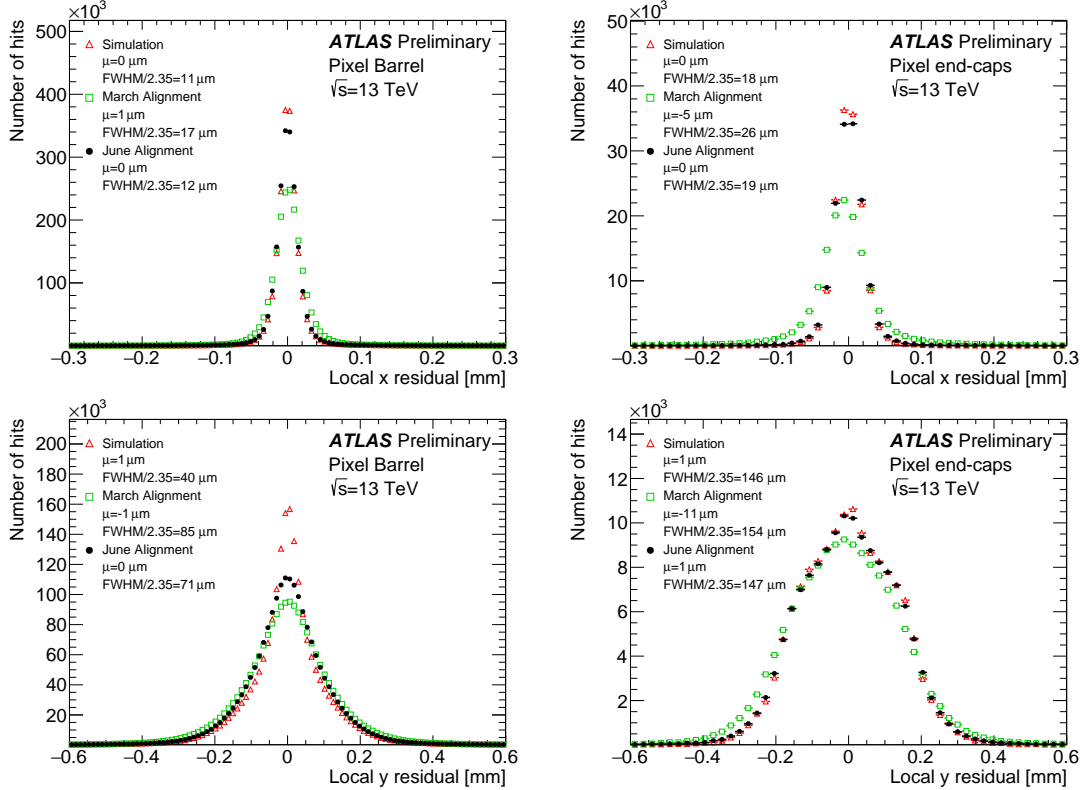


Figure 4.7: Local  $x$  (top) and local  $y$  (bottom) residual distributions for the Pixel barrel (excluding the IBL, left) and end-caps (right) using the  $\sqrt{s} = 13$  TeV collision data sample reconstructed using the June (black) and March (green) alignments. The data is compared to a MC simulation using a perfect detector geometry (red). The distributions are normalized to the same number of entries.

1055 the bias in the impact parameter.

### 1056 4.2.3 Error scaling

1057 The final step in preparing the new set of June alignment constants deals with the adjustment of  
 1058 the hit errors, or *error scaling*. Knowledge of the exact position of a hit measurement on a track  
 1059 is limited by the accuracy with which the sensors' positions are known. Let  $\sigma$  represent the hit  
 1060 uncertainty used in track fitting, and  $\sigma_0$  be the detector's intrinsic uncertainty. If  $\sigma = \sigma_0$ , the pull  
 1061 of the track-hit residual distributions should form a Gaussian distribution centered at zero with a  
 1062 standard deviation  $\sigma = 1$  [32]. In the case of residual misalignment, the pull distributions' standard  
 1063 deviations will stray from unity. The hit uncertainty can be written as:

$$\sigma = a \cdot \sigma_0 \oplus b \quad (4.12)$$

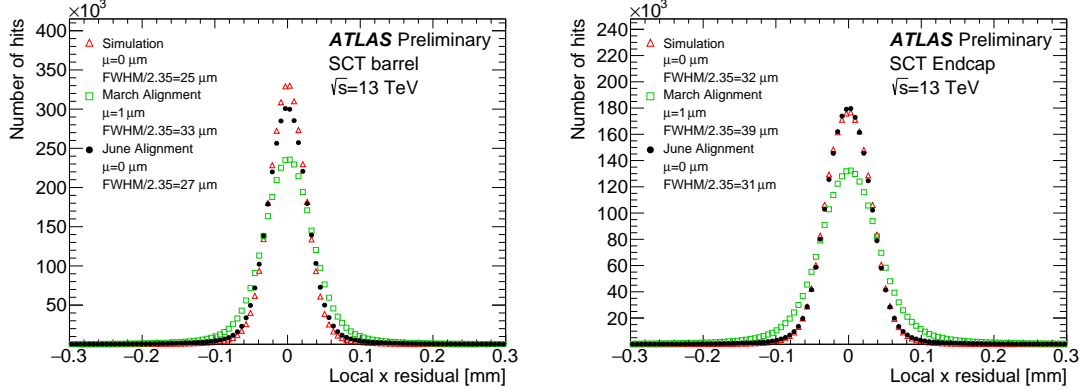


Figure 4.8: Local  $x$  residual distributions for the SCT barrel (left) and end-caps (right) using the  $\sqrt{s} = 13 \text{ TeV}$  collision data sample reconstructed using the June (black) and March (green) alignments. The data is compared to a MC simulation using a perfect detector geometry (red). The distributions are normalized to the same number of entries.

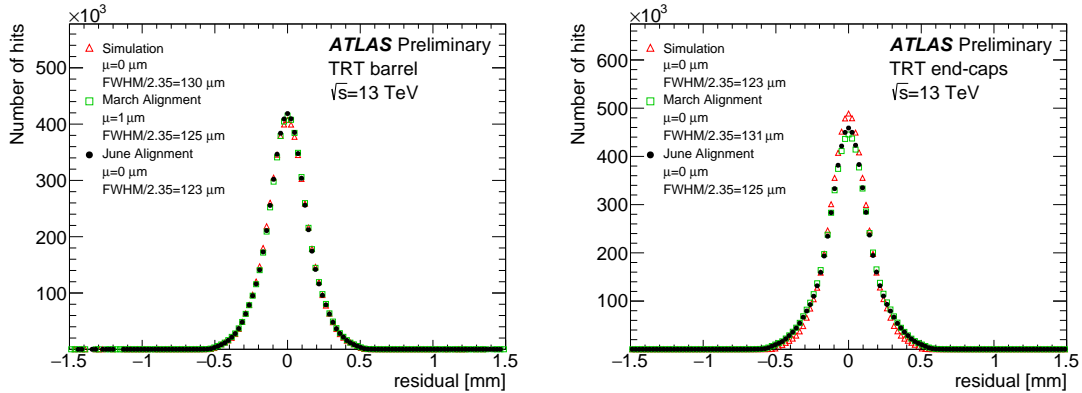


Figure 4.9: Residual distributions for the TRT barrel (left) and end-caps (right) using the  $\sqrt{s} = 13 \text{ TeV}$  collision data sample reconstructed using the June (black) and March (green) alignments. The data is compared to a MC simulation using a perfect detector geometry (red). The distributions are normalized to the same number of entries.

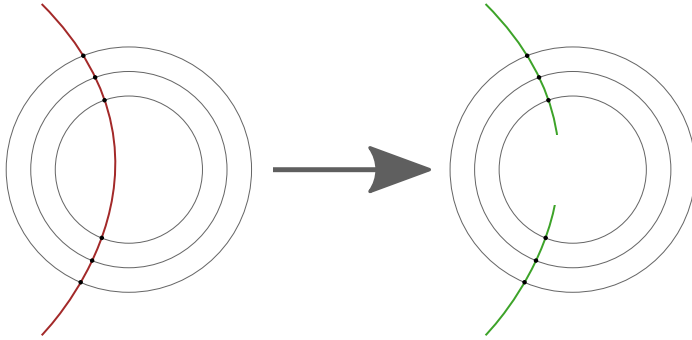


Figure 4.10: Representation of splitting a single cosmic ray track passing through the entire detector (left) into two separate tracks (right).

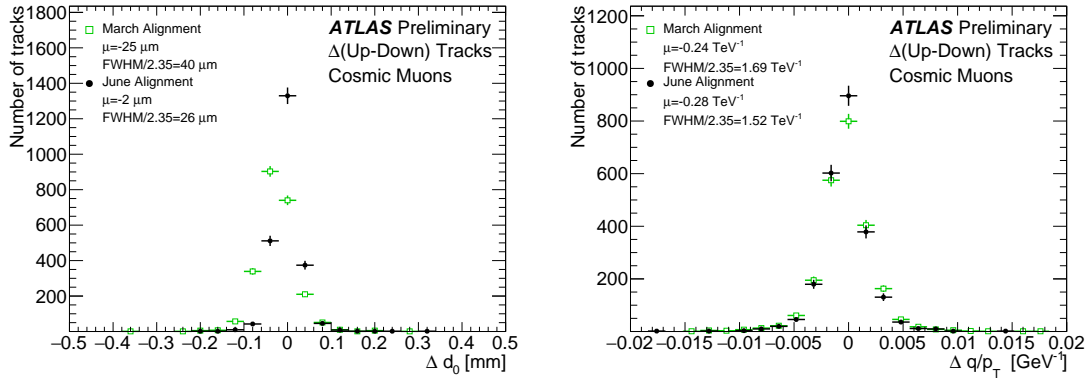


Figure 4.11: Distribution of the difference in the impact parameter  $\Delta d_0$  (left) and charge over transverse momentum  $\Delta q/p_T$  (right) between the two cosmic ray split tracks. The June (black) and March (green) alignments are compared. The distributions are normalized to the same number of entries.

1064 where  $a$  is a scaling factor, and  $b$  is a constant term which can be interpreted as a measure of any  
1065 remaining misalignment of the detector elements. In this alignment campaign, the value of  $a$  is fixed  
1066 at  $a = 1$  and  $b$  is evaluated from the residual pull distributions for each subdetector in its sensitive  
1067 directions.

1068 Once the value of  $b$  is determined, pull distributions derived from the new value of  $\sigma$  should  
1069 have unit width. The error scaling values for each subdetector are listed in Table 4.3, and the pull  
1070 distributions for the IBL after error scaling are shown in Figure 4.12.

Detector	Coordinate	$b(\mu\text{m})$
IBL	$x$	6.4
	$y$	43.6
Pixel	$x$	5.2
	$y$	28.6
Pixel	$x$	7.5
	$y$	0
SCT	$x$	10.8
	$x$	8.6
TRT	$r\phi$	0
	$r\phi$	0

Table 4.3: Estimated value of the error scaling term  $b$  for each subdetector component with the June alignment.

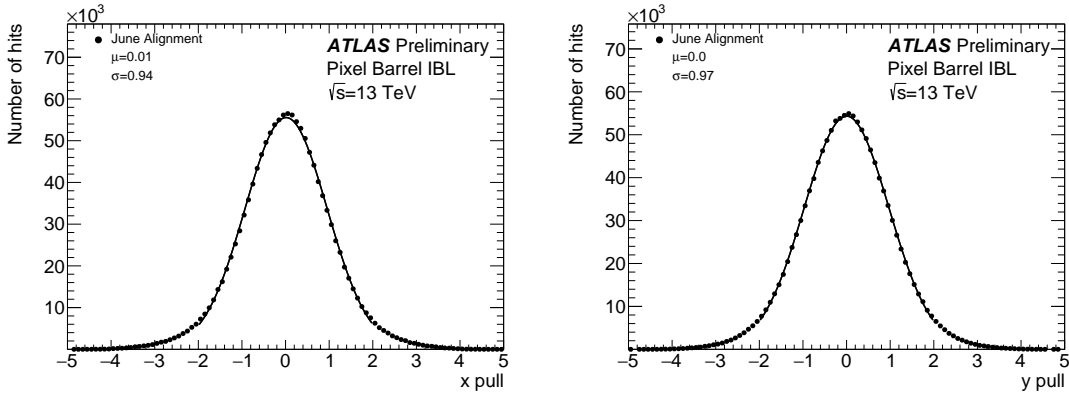


Figure 4.12: Pull distributions in local  $x$  (left) and  $y$  (right) for the IBL using the  $\sqrt{s} = 13$  TeV collision data sample after applying the error scaling.

### 1071 4.3 Level 2 alignment of the TRT

1072 During validation of the final end-of-year reprocessing of the 2015 data, a misalignment was found in  
 1073 the barrel of the TRT detector, as several modules (triangular clusters of straws) showed rotations in  
 1074 the local  $y$  coordinate. The then-best available constants included a full L3 alignment of the silicon  
 1075 detectors and a separate L2 alignment of the TRT. However, not all degrees of freedom were enabled  
 1076 when the TRT was aligned. To correct for these tilts, an additional four iterations of L2 alignment  
 1077 TRT was performed on the TRT enabling all available degrees of freedom ( $T_x$ ,  $T_y$ ,  $R_x$ ,  $R_y$ , and  $R_z$   
 1078 in the barrel, and  $T_x$ ,  $T_y$ , and  $R_z$  for the endcaps). Plots of the residual means from barrel  $\phi$  sectors  
 1079 containing modules affected by the tilt misalignment are shown in Figure 4.13 before and after the  
 1080 L2 alignment.

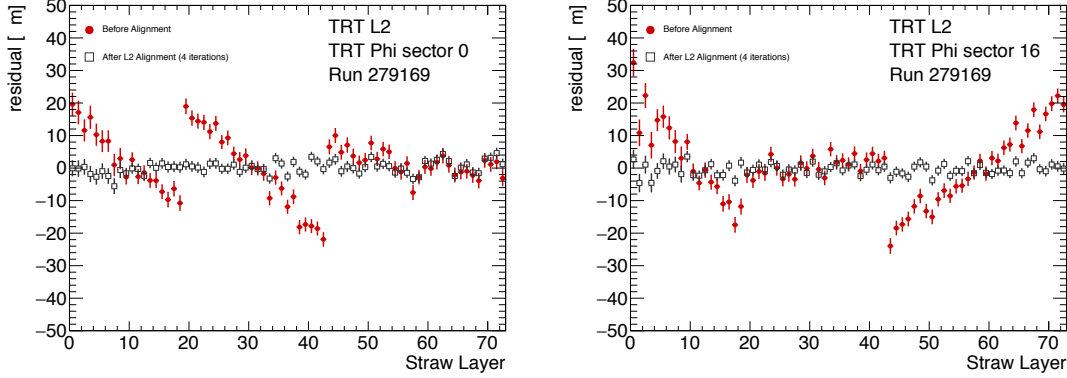


Figure 4.13: Residual means by straw layer in two TRT  $\phi$ -sectors affected by a tilt misalignment. The tilts in each of the three modules are clearly visible in the red points representing the reconstructed data prior to alignment. After four iterations of L2 alignment, the residual means in the gray points are flat.

Following the L2 alignment, some additional time was taken to determine if a full wire-by-wire L3 alignment of the TRT was necessary. The TRT was last aligned at L3 during Run 1, but initial alignment campaigns in Run 2 did not show signs of misalignment, as can be seen from the residual distributions in Figure 4.9. In order to assess the alignment more carefully, two dimensional residual maps in  $\phi$  and  $z$  were constructed for each layer in the TRT barrel and endcaps using the current alignment. These maps were compared to a similar set using the L3 alignment from 2010, from which it was determined that the straw-level alignment indeed hadn't degraded and a new L3 alignment was not needed. The maps for the first layer of the TRT barrel are shown in Figure 4.14 for both sets of alignment constants.

#### 4.4 Momentum bias from sagitta deformations

A variety of weak mode deformations can exist in the detector even after alignment. As mentioned previously, these weak modes consist of misalignments which don't affect the  $\chi^2$  of the residuals and thus are not handled by the basic alignment algorithm. In the presence of a weak mode, the description of the detector geometry can still provide efficient and high quality track fits, but there may also be systematic biases in one or more track parameters. Several weak modes, their impacts on the reconstruction, and the steps taken to eliminate them are detailed in [35, 43]. This section focuses specifically on sagitta distortions that result in a bias in the reconstructed track momentum.

These *sagitta* distortions consist of detector movements orthogonal to the trajectory of the outgo-

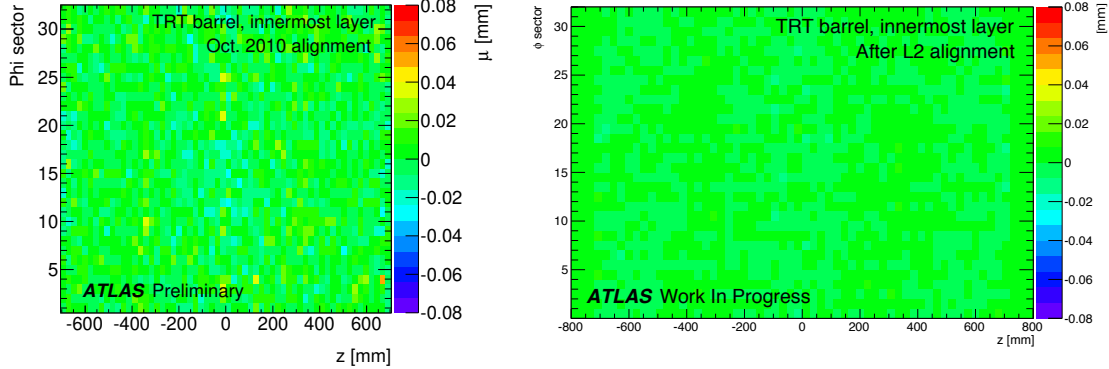


Figure 4.14: Two dimensional map of residuals in the first layer of the TRT barrel vs  $z$  and  $\phi$ . Each bin represents the mean of a Gaussian fit to the TRT residuals in that bin. The map on the left is after the L3 (wire-by-wire) alignment of the TRT performed in 2010, and the map on the right is after the L2 alignment at the end of 2015. The  $z$ -axis for both plots use the same scale. Left figure taken from [32].

1099 ing particle. The effect on the reconstructed track curvature is different for positively and negatively  
1100 charged particles, resulting in a charge-antisymmetric bias. This effect is illustrated in the curl  
1101 deformation shown in Figure 4.15.

1102 In the plane transverse to ATLAS’s magnetic field, outgoing particle tracks form circular arcs.  
1103 The sagitta is defined as the distance from the center of this arc to the center of its base, as shown in  
1104 Figure 4.16, and it represents the “amount of bending” in the track. In the case where the sagitta  $s$   
1105 is considerably smaller than the detector radius  $R_0$ , which is a valid assumption when working with  
1106 high momentum tracks, the transverse momentum of a particle of charge  $q$  can be written as [44]:

$$p_T \propto qB \frac{R_0^2}{8s} \quad (4.13)$$

1107 where  $B$  is the strength of the detector’s magnetic field. If a sagitta bias is present, the track’s  
1108 transverse momentum shifts by [43]:

$$q/p_T \rightarrow q/p_T + \delta_s \quad \text{or} \quad p_T \rightarrow p_T \cdot (1 + qp_T \delta_s)^{-1} \quad (4.14)$$

1109 where  $\delta_s$  is a universal bias parameter that uniquely defines the deformation. Finally, since the  
1110 reconstructed polar angle does not change under a sagitta deformation, the longitudinal component  
1111 of the momentum scales along with the transverse component, and an equivalent equation can be  
1112 written for the total momentum:

$$p \rightarrow p \cdot (1 + qp_T \delta_s)^{-1} \quad (4.15)$$

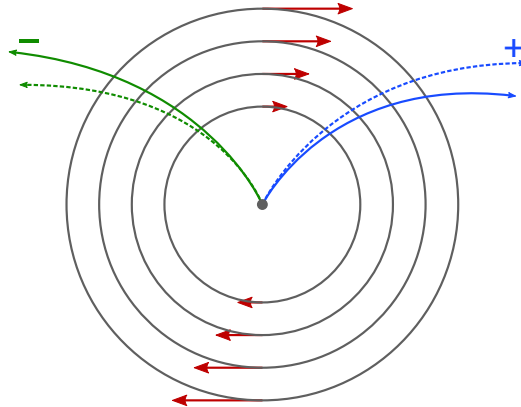


Figure 4.15: Representation of a curl distortion in the detector. The image shows a cutaway in the transverse plane. The deformation is represented by the red arrows, and the impact on the reconstructed positive (blue) and negative (green) tracks are shown. The dashed lines represent the true particle trajectories, and the solid lines represent the reconstructed trajectories.

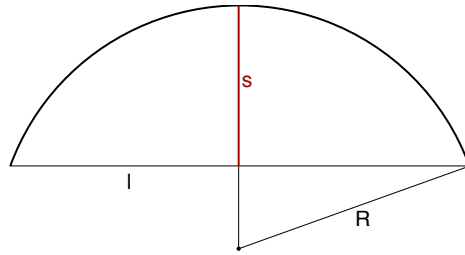


Figure 4.16: Geometric definition of the sagitta  $s$  in relation to the length of the chord  $l$  and the radius  $r$  of a circular arc.

#### 1113 4.4.1 Sagitta bias monitoring with electron $E/p$

1114 Since a sagitta bias results in changes in the momentum of particles' tracks as measured by the ID,  
 1115 they can be identified using independent measurements from other systems in the detector. One  
 1116 such method involves using the energy-momentum ratio of electrons ( $E/p$ ). Since the electron's  
 1117 energy is measured in ATLAS's calorimeter systems, it is not sensitive to any sagitta bias that may  
 1118 exist in the ID and the corresponding track momentum. Under the assumption that the calorimeter  
 1119 response is independent of the charge of incoming particles, a charge-dependent momentum bias in  
 1120 the ID will manifest as a difference in the  $E/p$  ratio for electrons and positrons.

1121 In the presence of a sagitta bias, the momentum will change according to Equation 4.15 and the  
 1122 average measured  $\langle E/p \rangle$  can be written as:

$$\langle E/p \rangle^\pm \rightarrow \langle E/p \rangle^\pm \pm \langle E_T \rangle \delta_s \quad (4.16)$$

1123 where the approximation  $p_T \approx E_T$  is used. Assuming that  $\langle E/p \rangle^+ = \langle E/p \rangle^-$  in the absense of a  
 1124 bias, the sagitta bias parameter can be written as:

$$\delta_s = \frac{\langle E/p \rangle^+ - \langle E/p \rangle^-}{2\langle E_T \rangle} \quad (4.17)$$

1125 If the kinematic selections for electrons and positrons are identical, the energy scale of the calorimeter  
 1126 will not factor into the  $\langle E/p \rangle$  difference; however, it will affect  $\langle E_T \rangle$  which would scale the measured  
 1127  $\delta_s$ . This is expected to be a small effect, as the energy scale for electrons has been measured at  
 1128  $\sqrt{s} = 13$  TeV with uncertainties on the per-mil level across the entire detector [45].

#### 1129 4.4.1.1 Measuring $\langle E/p \rangle$

1130 The  $E/p$  ratio is measured using electrons and positrons from  $Z \rightarrow e^\pm e^\mp$  events in order to obtain  
 1131 a high purity sample of electron candidates. They are required to pass a basic selection criteria to  
 1132 ensure they are well measured by both the ID and the calorimeters:

- 1133 •  $E_T > 25$  GeV
- 1134 •  $|\eta| < 2.47$ , excluding the calorimeter’s barrel-to-endcap transition region in  $1.37 < |\eta| < 1.52$
- 1135 • Pass MediumLH identification working point detailed in Section 3.2.4.3
- 1136 • Pass a selection of quality cuts, including a requirement that the electron be identified using  
 1137 cluster information in the calorimeter
- 1138 • The associated track must have at least one hit in the IBL, three in the Pixel detector, and  
 1139 five in the SCT detector.

1140 Events with exactly two opposite-charge electrons passing this selection with a dielectron invariant  
 1141 mass within 30 GeV of the  $Z$  boson mass are then used for the  $E/p$  calculation.

1142 Since the size of the sagitta bias  $\delta_s$  is not expected to be constant across the entire detector,  
 1143 a two-dimensional rectangular grid binned in detector  $\eta$  and  $\phi$  is constructed. From the selected  
 1144 events, separate distributions of  $E/p$  are made for electrons and positrons lying in each bin. Each  
 1145 distribution is fit with Crystal Ball function<sup>8</sup>, and the peak of the distribution is taken as the value  
 1146 of  $\langle E/p \rangle$ . If there is no bias on the track momentum in the bin, the peaks for electrons and positrons  
 1147 should match. Example  $E/p$  distributions including the Crystal Ball fits are shown in Figure 4.17.

---

<sup>8</sup>The Crystal Ball function is a probability density function consisting of a Gaussian core and a power-law tail.

1148 It is important to emphasize that deviations from one in the *ratio* of  $\langle E/p \rangle$  for electrons and  
 1149 positrons indicates that a momentum bias may be present. The value of  $\langle E/p \rangle$  itself is not expected  
 1150 to equal one exactly, as the track momentum on average tends to be slightly lower than the energy  
 1151 measurement in the calorimeter. This is due to the fact that if the electron were to radiate a photon,  
 1152 its momentum would change slightly, while it is likely that both the electron and the emitted photon  
 1153 would leave energy deposits near each other in the calorimeter and be reconstructed into the same  
 1154 object.

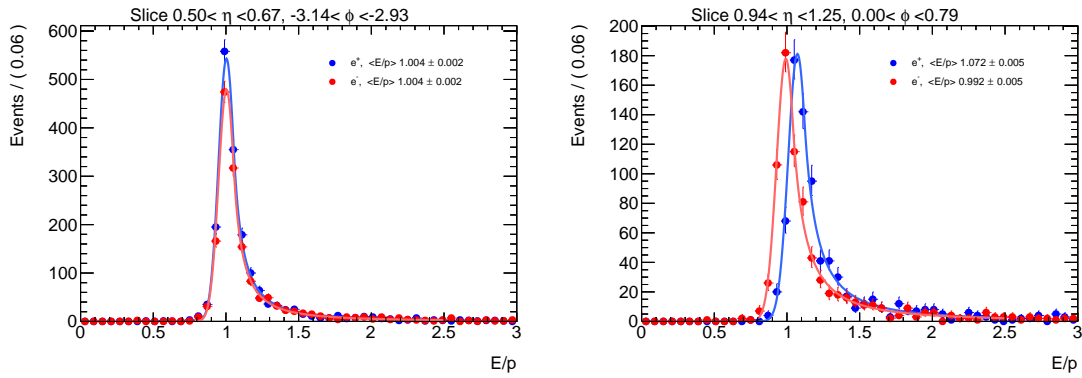


Figure 4.17:  $E/p$  distributions of electrons and positrons in two different  $\eta\text{-}\phi$  bins of the detector. The left hand plot is taken from a region with no momentum bias where  $\langle E/p \rangle^+ = \langle E/p \rangle^-$ , while the right hand plot shows an 8% disagreement in  $\langle E/p \rangle$  between electrons and positrons.

1155 Once the  $\langle E/p \rangle^\pm$  distributions in each  $\eta\text{-}\phi$  bin have been extracted from the fits, a two dimensional  
 1156 map of  $\delta_s$  can be constructed using Equation 4.17. The map gives an overview of sagitta  
 1157 biases that may be present in the detector, and can be used by the alignment algorithm to reduce  
 1158 the bias in the next iteration. In this case, the tracks fed to the alignment have their momenta  
 1159 corrected according to [43]:

$$q/p_{\text{corr}} = q/p_{\text{reco}}(1 - qp_T\delta_s) \quad (4.18)$$

1160 where  $p_{\text{reco}}$  is the reconstructed momentum of the track. The corrected momentum is then con-  
 1161 strained in the alignment.

#### 1162 4.4.1.2 Results in 13 TeV data

1163 The  $E/p$  method has been used to monitor sagitta biases in the detector several times over the  
 1164 course of Run 2. During this time, it has primarily served as an independent cross-check to a  
 1165 second method using  $Z \rightarrow \mu^\pm \mu^\mp$  events [43]. The  $Z \rightarrow \mu^\pm \mu^\mp$  method identifies individual track  
 1166 momentum biases through shifts in the reconstructed  $Z$  mass, which leaves it relatively insensitive

1167 to global sagitta biases. For this reason, the sagitta bias maps produced using this technique are  
 1168 normalized to those from the  $E/p$  method before being used to constrain the alignment.

1169 The results of two implementations of the  $E/p$  method are presented here.

- 1170 1. The first follows the end-of-year reprocessing of the entire ATLAS 2016 data set at  $\sqrt{s} =$   
 1171 13 TeV. Two sets of alignment constants are compared: the *prompt* alignment, which was  
 1172 derived shortly after each run was recorded, and the *reprocessed* alignment. The maps of the  
 1173 sagitta bias comparing the two alignments calculated using the  $E/p$  method are shown in  
 1174 Figure 4.18, and the comparison of the  $\eta$  projection of each map is shown in Figure 4.19.
- 1175 2. The second uses the 2017 data after reprocessing, and compares the effects of multiple it-  
 1176 erations of the method. In each iteration, the momenta of the electrons and positrons are  
 1177 corrected based on Equation 4.15 using the value of  $\delta_s$  computed in the previous iteration,  
 1178 and a new sagitta bias map is calculated. If the method is indeed characterizing the sagitta  
 1179 biases correctly, the corrections should converge quickly. The initial sagitta bias map is com-  
 1180 pared to the map after two such iterations in Figure 4.20, and the sagitta bias projected along  
 1181  $\eta$  for each iteration is shown in Figure 4.21. Indeed, after just two iterations,  $\delta_s$  is consistent  
 1182 with zero in nearly all bins.

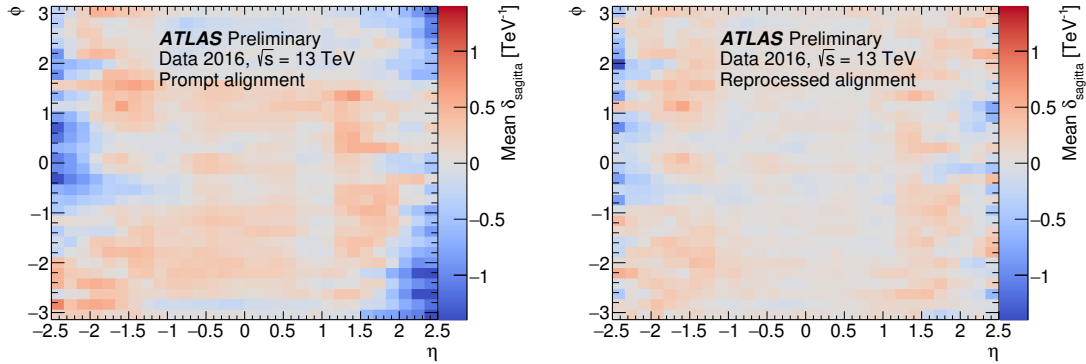


Figure 4.18: Sagitta bias in the  $\sqrt{s} = 13$  TeV data collected by ATLAS in 2016 as a function of  $\eta$  and  $\phi$  for the prompt (left) and reprocessed (right) alignments using the  $E/p$  method.

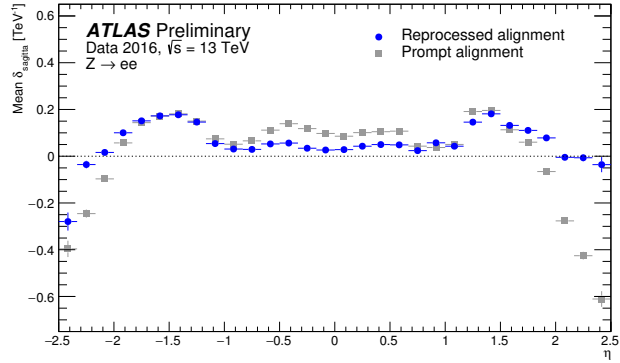


Figure 4.19: Sagitta bias in the  $\sqrt{s} = 13 \text{ TeV}$  data collected by ATLAS in 2016 projected along  $\eta$  for the prompt (gray) and reprocessed (blue) alignments using the  $E/p$  method.

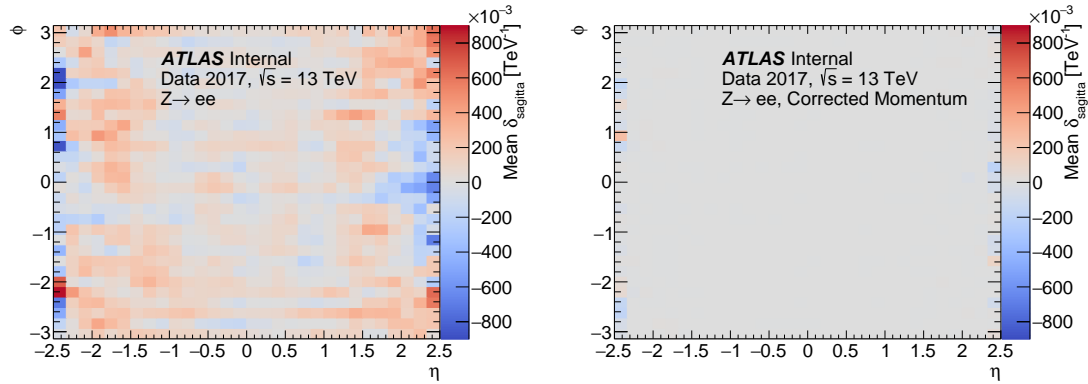


Figure 4.20: Sagitta bias in the  $\sqrt{s} = 13 \text{ TeV}$  data collected by ATLAS in 2017 as a function of  $\eta$  and  $\phi$  in reconstructed electrons (left) and after two iterations of momentum corrections (right) from the  $E/p$  method.

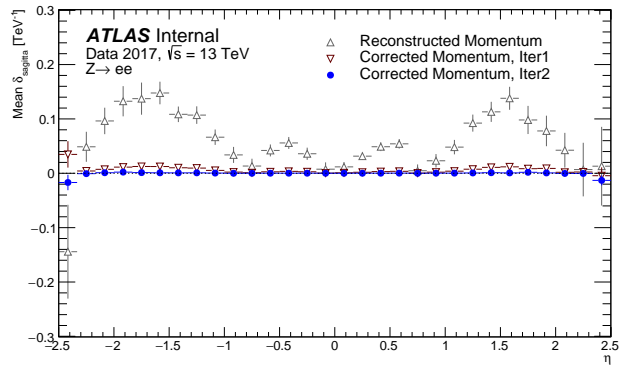


Figure 4.21: Sagitta bias in the  $\sqrt{s} = 13$  TeV data collected by ATLAS in 2017 projected along  $\eta$  in reconstructed electrons (gray) and after one (red) and two (blue) iterations of momentum corrections from the  $E/p$  method.

1183

## CHAPTER 5

1184

1185

# Measurement of same-sign $WW$ production at $\sqrt{s} = 13$ TeV with ATLAS

1186 Production of same-sign  $W$  boson pairs is a particularly interesting SM process. When produced  
1187 via vector boson scattering (VBS),  $W^\pm W^\pm jj$  is sensitive to the electroweak symmetry breaking  
1188 (EWSB) mechanism as well as potential Beyond the Standard Model (BSM) physics processes.  
1189  $W^\pm W^\pm jj$  events can be produced via electroweak-mediated (EWK) diagrams, of which VBS is a  
1190 subset, or QCD-mediated diagrams. The biggest advantage of same-sign  $W^\pm W^\pm jj$  over other VBS  
1191 processes lies in its ratio of electroweak (EWK) to QCD production cross sections. Despite the  
1192 opposite-sign  $W^\pm W^\mp$  having a larger total cross section, its EWK-mediated diagrams are much  
1193 smaller than its QCD-mediated diagrams, while for same-sign  $W^\pm W^\pm$  the EWK production is  
1194 considerably larger. This makes  $W^\pm W^\pm jj$  one of the premier channels for studying VBS at the  
1195 LHC.

1196 The first evidence of electroweak (EWK)  $W^\pm W^\pm jj$  production was seen by the ATLAS and CMS  
1197 experiments at  $\sqrt{s} = 8$  TeV with excesses of  $3.6\sigma$  [46] and  $2.0\sigma$  [47] over backgrounds, respectively.  
1198 More recently, ATLAS and CMS have both observed the EWK process at  $\sqrt{s} = 13$  TeV with  
1199 significances of  $6.9\sigma$  [48] and  $5.5\sigma$  [49], respectively. The ATLAS  $\sqrt{s} = 13$  TeV observation and  
1200 cross section measurement of EWK-produced  $W^\pm W^\pm jj$  is presented in this chapter [48, 50].

### 1201 5.0.1 Experimental overview of vector boson scattering

1202 VBS processes are very important to understand due to their sensitivity to the EWSB mechanism.  
1203 As explained in Section 2.3, in the absence of a light SM Higgs boson, the scattering amplitude of  
1204 longitudinally polarized vector bosons grows with center-of-mass energy. However, once the Higgs

1205 is introduced, the divergences cancel and the cross section no longer grows unbounded.

1206 With the discovery of the Higgs boson in 2012 [15, 16], the EWSB mechanism can now be directly  
 1207 studied. Due to the potential exchange of a Higgs boson in the VBS diagrams ( $W^\pm W^\pm jj$  itself does  
 1208 not contain an  $s$ -channel Higgs exchange), VBS processes are directly sensitive to properties of the  
 1209 Higgs. For example, the high-mass tail in the  $VV$  scattering system allows an approximation of the  
 1210 effective coupling strength of the Higgs to vector bosons that is independent of any assumptions  
 1211 on the Higgs width [51]. Additionally, the center of mass energy dependence of the  $VV$  scattering  
 1212 can reveal whether the Higgs boson unitarizes the longitudinal scattering amplitude fully or only  
 1213 partially [52].

1214 VBS events are characterized by two quarks from the colliding protons each radiating a vector  
 1215 boson which then scatter and decay in the detector. The incoming quarks carry a large amount of  
 1216 momentum and only deflect a small amount upon emitting the vector boson; as a result, they often  
 1217 enter the calorimeters very close to the beam line. Ignoring the decay products of the scattered  
 1218 bosons for now, these VBS events result in a final state of two vector bosons ( $V$ ) and two jets ( $j$ )  
 1219 at high pseudorapidities (called *forward jets* or *tag jets*) from the outgoing quarks. The shorthand  
 1220  $VVjj$  is used to represent this final state.

1221  $VVjj$  events can be produced via two different physical processes. The first involves purely  
 1222 electroweak interactions in the tree-level diagrams, of order  $\mathcal{O}(\alpha_{\text{EWK}}) = 6$  in the electroweak coupling  
 1223 constant, and will be referred to as *EWK production*. This can be further broken down into VBS  
 1224 and non-VBS events. In the VBS EWK production, the scattering occurs via triple or quartic gauge  
 1225 couplings, as well as the exchange of a Higgs boson. The non-VBS EWK production contains the  
 1226 same final state of two vector bosons and two outgoing quarks, but the bosons do not scatter. Due to  
 1227 gauge invariance, it is not possible to separate the VBS from the non-VBS productions [53]; therefore,  
 1228 both are included in the signal generation and are indistinguishable from one another. The second  
 1229 process involves a mix of the EWK and strong interactions, of order  $\mathcal{O}(\alpha_s) = 2 \otimes \mathcal{O}(\alpha_{\text{EWK}}) = 4$ , and  
 1230 will be referred to as *QCD production*. The tree-level Feynman diagrams for VBS EWK, non-VBS  
 1231 EWK, and QCD  $VVjj$  production are found in Figures 5.1, 5.2, and 5.3, respectively.

### 1232 5.0.2 Same-sign $W^\pm W^\pm$ scattering

1233 Same-sign  $W^\pm W^\pm jj$  scattering is considered to be one of the best channels for studying VBS at the  
 1234 LHC due to its favorable ratio of EWK to QCD production [51]. Since the VBS diagrams (which are  
 1235 a subset of the total EWK production) are the primary source of interest for an analysis, the QCD

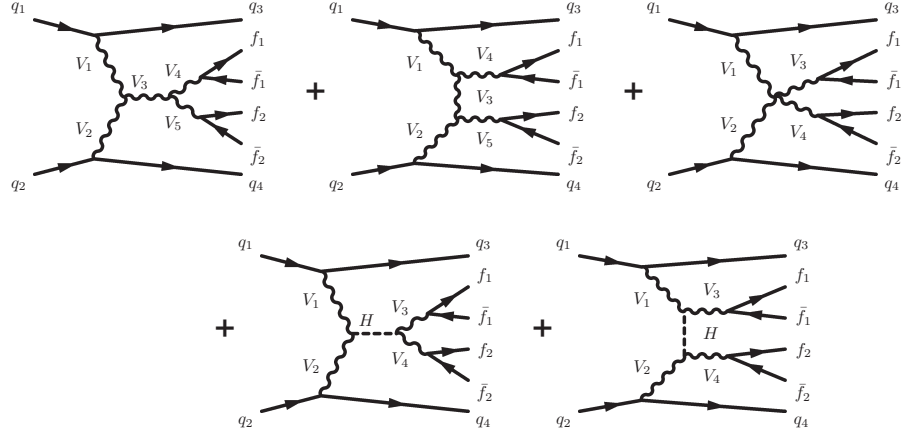


Figure 5.1: Tree-level Feynman diagrams for VBS EWK  $VVjj$  production including triple gauge couplings involving  $W$  and/or  $Z$  bosons (top left and top middle), quartic gauge coupling (top right), or the exchange of a Higgs boson ( $s$ -channel bottom left and  $t$ -channel bottom right). The labels are quarks ( $q$ ), fermions ( $f$ ), and gauge bosons ( $V = W, Z$ ).

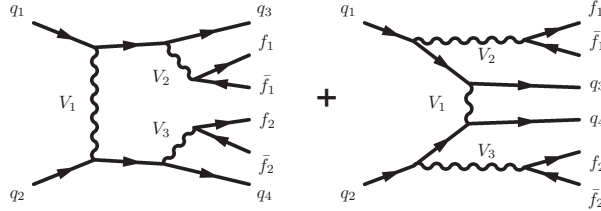


Figure 5.2: Tree-level Feynman diagrams for non-VBS EWK  $VVjj$  production. The labels are quarks ( $q$ ), fermions ( $f$ ), and gauge bosons ( $V = W, Z$ ).

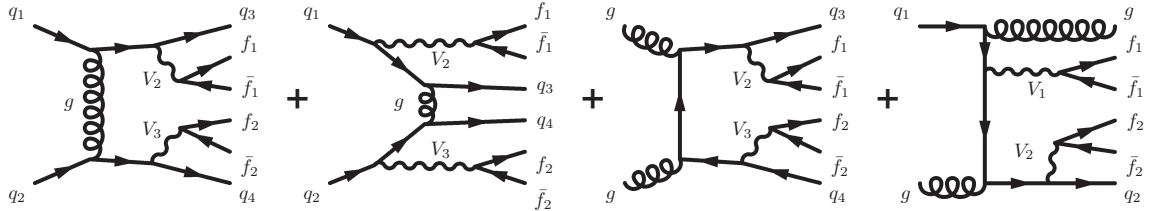


Figure 5.3: Tree-level Feynman diagrams for QCD  $VVjj$  production. The labels are quarks ( $q$ ), fermions ( $f$ ), and gauge bosons ( $V = W, Z$ ).

1236 production would be considered a background in an analysis. Therefore a higher EWK-to-QCD  
 1237 ratio results in increased sensitivity to VBS. EWK and QCD cross sections at  $\sqrt{s} = 13$  TeV for  
 1238 six leptonic  $VVjj$  final states were calculated using the **SHERPA** MC generator in a VBS-enriched  
 1239 fiducial phase space in [54]. Despite its relatively low total cross section compared to some other  
 1240  $VVjj$  processes, the EWK-to-QCD ratio for  $W^\pm W^\pm jj$  is 10-20 times higher than for other processes  
 1241 after applying VBS-enhancing selection criteria.

Final state	Process	$\sigma_{\text{EWK}}$ [fb]	$\sigma_{\text{QCD}}$ [fb]	$\sigma_{\text{EWK}}/\sigma_{\text{QCD}}$
$l^\pm l^\mp l^\pm l^\mp jj$	$ZZ$	0.098	0.100	0.98
$l^\pm l^\pm l^\mp \nu jj$	$W^\pm Z$	2.34	4.38	0.53
$l^\pm l^\mp \nu \nu jj$	$W^\pm W^\mp, ZZ$	12.3	21.8	0.56
$l^\pm l^\pm \nu \nu jj$	<b><math>W^\pm W^\pm</math></b>	<b>3.97</b>	<b>0.346</b>	<b>11.47</b>
$l^\pm \nu \nu \nu jj$	$W^\pm Z$	7.64	15.5	0.49
$\nu \nu \nu \nu jj$	$ZZ$	1.68	1.38	1.22

Table 5.1: Predicted cross sections for EQK and QCD production of diboson processes relevant to VBS at  $\sqrt{s} = 13$  TeV using the **SHERPA** MC generator. The numbers for the  $W^\pm W^\pm jj$  process are bolded. Leptons are required to have  $p_T \geq 25$  GeV and lie within  $|\eta| \leq 2.5$  with  $m_l > 20$  GeV, and at least two jets are required with  $p_T \geq 30$  GeV and  $|\eta| < 4.5$ . The VBS contributions are enhanced by requiring the dijet invariant mass  $m_{jj} > 500$  GeV and dijet separation  $\Delta y_{jj} > 2.4$ . Numbers taken from [54].

1242 This analysis studies  $W^\pm W^\pm jj$  scattering where both  $W$  bosons decay leptonically to  $e\nu$  or  $\mu\nu$ <sup>9</sup>.  
 1243 The  $W^\pm W^\pm jj$  VBS final state consists of two leptons with the same electric charge, two neutrinos,  
 1244 and two high energy forward jets with a large invariant mass. Tree-level Feynman diagrams of VBS  
 1245  $W^\pm W^\pm jj$  production can be found in Figure 5.4 and a visual representation of the VBS topology  
 1246 can be found in Figure 5.5.

1247 The two tag jets in the characteristic VBS signature also serve as a powerful tool to suppress  
 1248 the QCD production mode. In EWK events, the two jets tend to have much higher separation and  
 1249 a larger combined invariant mass than the two leading jets in a QCD event. The two plots shown  
 1250 in Figure 5.6 highlight the differences in these dijet quantities between the two production modes.  
 1251 Finally, an ATLAS event display of a real  $W^\pm W^\pm jj$  candidate event is shown in Figure 5.7.

### 1252 5.0.3 Overview of backgrounds

1253 In addition to QCD production of  $W^\pm W^\pm jj$  events, there are several other processes with a final  
 1254 state of two same-sign leptons, two neutrinos, and two jets. However, due to the  $\pm 2$  final state charge,

<sup>9</sup>Throughout the rest of this chapter, unless stated otherwise,  $l$  denotes either electrons ( $e$ ) or muons ( $\mu$ ), and  $\nu$  denotes a neutrino. Additionally,  $e$ ,  $\mu$ , and  $\nu$  with no charge or anti-particle designation refer interchangeably to either the particle or anti-particle.

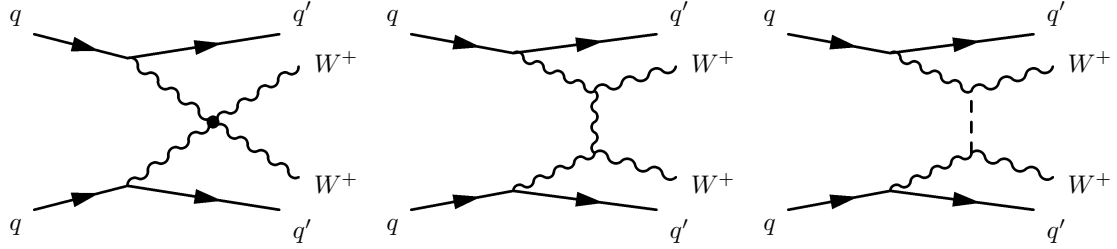


Figure 5.4: Leading order Feynman diagrams for VBS EWK production of  $W^\pm W^\pm jj$  events. The leftmost diagram contains a quartic gauge coupling vertex, and the rightmost diagram contains an exchange of a Higgs boson.

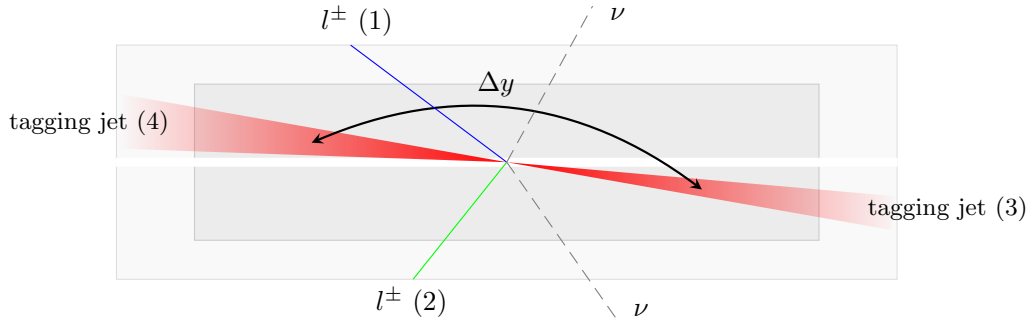


Figure 5.5:  $W^\pm W^\pm jj$  VBS event topology containing two leptons (1 and 2) with the same electric charge, two neutrinos, and two forward tagging jets (3 and 4) with large rapidity separation  $\Delta y$ .

1255 there is a considerable reduction in SM backgrounds (such as  $Z$  boson events) when compared to  
 1256 an analysis like opposite-sign  $W^\pm W^\mp jj$ .

1257 One of the largest sources of background involves processes with prompt leptons<sup>10</sup>. These are  
 1258 events that contain two leptons with the same electric charge and one or more additional leptons that  
 1259 are “lost”, either by failing the selection criteria or falling outside of the detector’s acceptance. The  
 1260 number of processes that can contribute is limited by the requirement of same-sign leptons, and as a  
 1261 result this background is dominated by multi-boson processes, with the largest contribution coming  
 1262 from  $WZ$  events and smaller contributions from  $ZZ$  and  $t\bar{t} + V$  events. Triboson events where one  
 1263 boson decays hadronically also contribute to this background; however, the jets are generally softer  
 1264 and more central than in a typical VBS event, and the cuts applied on the forward jets suppress  
 1265 these contributions.

<sup>10</sup>Prompt leptons are those that are produced in the primary collision and are a direct decay product of the process of interest. Non-prompt leptons originate from some secondary process, such as a  $b$ -hadron decay, or are jets that get mis-reconstructed as a lepton.

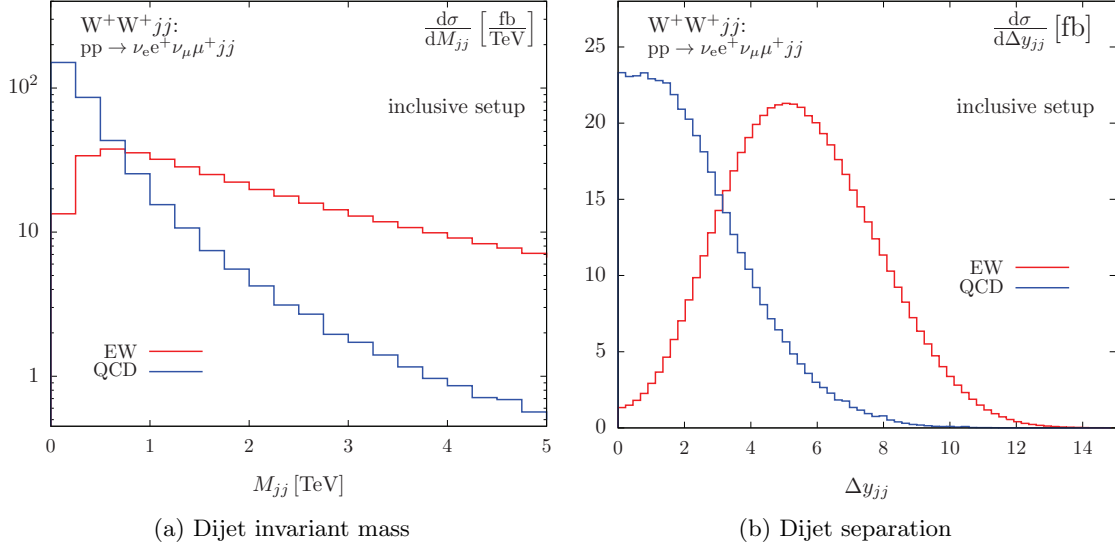


Figure 5.6: Generator level comparisons at  $\sqrt{s} = 7$  TeV of dijet invariant mass ( $M_{jj}$ , left) and dijet rapidity ( $\Delta y_{jj}$ , right) in EWK (red) and QCD (blue)  $W^\pm W^\pm jj$  events with no selection cuts applied. Plots taken from [55].

1266     The other dominant background comes from non-prompt, or “fake”, leptons. Here one or more  
 1267     leptons originate from the decay of another particle unrelated to the signal process, such as a heavy-  
 1268     flavor decay or photon conversion, or come from a jet that is misidentified as a lepton. This back-  
 1269     ground is mostly made up of events from  $t\bar{t}$  and  $W+jets$  processes, with a much smaller contribution  
 1270     from conversions in  $V\gamma$  events.

1271     Finally, opposite-sign lepton pairs can enter the signal region if one of the leptons is reconstructed  
 1272     with the wrong charge (called *charge misidentification*<sup>11</sup>). In practice, this only affects events with  
 1273     electrons, as the charge misidentification rate for muons is negligible [56]. This is a major background  
 1274     in events with two electrons, but it is a much smaller contribution for events with one electron and  
 1275     one muon.

## 1276     5.1 Data and Monte Carlo samples

1277     This analysis uses  $36.1 \text{ fb}^{-1}$  of  $\sqrt{s} = 13$  TeV proton-proton collisions recorded by ATLAS during  
 1278     the 2015 and 2016 data taking periods. The uncertainty in the combined integrated luminosity is  
 1279     2.1%. It is derived following a methodology similar to that detailed in [57] and using the LUCID-2

<sup>11</sup>Charge misidentification is also referred to interchangeably as *charge mis-ID* and *charge flip*.

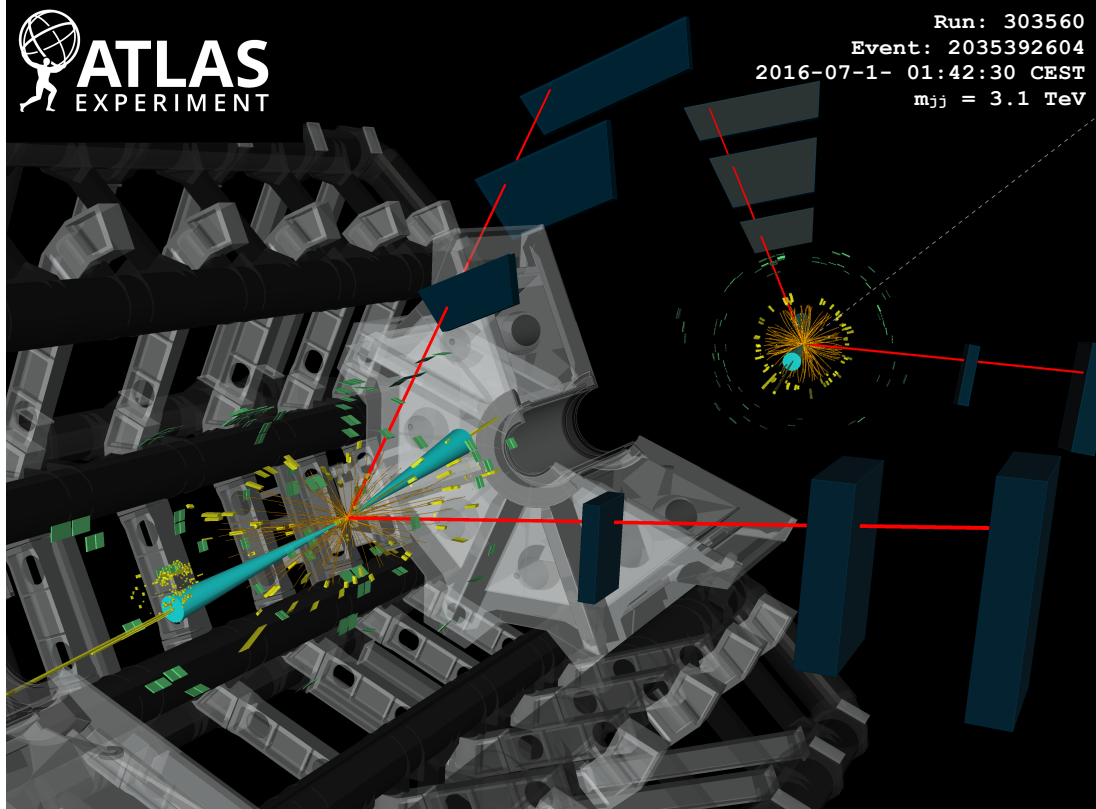


Figure 5.7: ATLAS event display of a  $pp \rightarrow W^+W^+ \rightarrow \mu^+\nu_\mu\mu^+\nu_\mu jj$  event. The muons are represented by the red lines travelling from the ID through the MS, and the forward jets are represented by the blue cones with yellow energy deposits in the calorimeters. The direction of the  $E_T^{\text{miss}}$  in the transverse plane is indicated by the gray dashed line in the inset image. Event display taken from [48].

1280 detector for the baseline luminosity measurements [58] from calibration of the luminosity scale using  
 1281  $x$ - $y$  beam-separation scans.

### 1282 5.1.1 Monte Carlo samples

1283 A number of Monte Carlo (MC) simulations are employed to model signal and background processes.  
 1284 In order to model the real collision data as closely as possible, each MC sample has been passed  
 1285 through a full simulation of the ATLAS detector in GEANT4 [59, 60], and events have been recon-  
 1286 structed using the same algorithms as the data. The simulation reproduces as closely as possible  
 1287 the momentum resolutions and calorimeter responses of the detector, and also includes the effects  
 1288 of pileup by including soft QCD interactions using PYTHIA v8.1 [61]. The MC samples used in this

Process	Generator	Comments
$W^\pm W^\pm jj$ (EWK)	SHERPA v2.2.2	Signal sample
$W^\pm W^\pm jj$ (EWK)	POWHEG-BOX v2	Systematics sample
$W^\pm W^\pm jj$ (QCD)	SHERPA v2.2.2	
Diboson	SHERPA v2.2.2	Both bosons decay leptonically ( $llll$ , $ll\nu\nu$ , $l\nu\nu\nu$ )
	SHERPA v2.2.1	One boson decays leptonically, the other hadronically
Triboson	SHERPA v2.1.1	
$W+jets$	SHERPA v2.2.1	
$Z+jets$	Madgraph5_aMC@NLO	
$V\gamma$	SHERPA v2.1.1	
$V\gamma jj$ (EWK)	SHERPA v2.2.4	
$t\bar{t}V$	Madgraph5_aMC@NLO	
$t\bar{t}$	POWHEG-BOX v2	
Single top	POWHEG-BOX v1	EWK $t$ -, $s$ -, & $Wt$ -channels

Table 5.2: Summary of MC samples used in the analysis.

analysis are detailed in this section and summarized in Table 5.2.

The  $W^\pm W^\pm jj$  samples are modeled using SHERPA v2.2.2 [62, 63, 64] with the NNPDF3.0 PDF set [65]. The EWK signal samples were generated by fixing the electroweak coupling constant to  $\mathcal{O}(\alpha_W) = 6$ , and a QCD background sample was also generated with  $\mathcal{O}(\alpha_W) = 4$ . SHERPA includes up to one parton at next-to-leading order (NLO) and up to three at leading order (LO) in the strong coupling constant  $\alpha_s$ . A second  $W^\pm W^\pm jj$  EWK sample was generated using POWHEG-BOX v2 [66] with the NNPDF3.0 PDF set and at NLO accuracy. This sample is only used for systematic studies, as POWHEG-BOX does not include resonant triboson contributions in its matrix element, which are non-negligible at NLO [67].

Diboson processes ( $VV$  where  $V = W, Z$ ) are simulated with SHERPA v2.2.2 for mixed hadronic and leptonic decays and SHERPA v2.2.1 for fully leptonic decays of the bosons. Similarly, triboson ( $VVV$ ) and  $V\gamma$  processes are simulated using SHERPA v2.1.1 with up to one parton at NLO and up to three at LO.  $W+jets$  processes are simulated with SHERPA v2.2.1 with up to two partons at NLO and four at LO. All the above SHERPA samples use the NNPDF3.0 PDF set and SHERPA's own parton showering. The  $Z+jets$  events are generated with Madgraph5\_aMC@NLO [68] at LO and interfaced with PYTHIA v8.1 for parton showering.

$t\bar{t}V$  events are generated using POWHEG-BOX v2 with the CT10 PDF set [69].  $t\bar{t}V$  samples are generated at NLO with Madgraph5\_aMC@NLO and the NNPDF3.0 PDF set interfaced with PYTHIA v8 for parton showering. Finally, single top events are generated with POWHEG-BOX v1 and the CT10f4 PDF set interfaced with PYTHIA v6 [70] for parton showering.

1309 **5.2 Object and event selection**

1310 This section details the selection criteria for objects used in the analysis as well as the selection for  
1311 signal events.

1312 **5.2.1 Object selection**

1313 Muons, electrons, and jets all must pass strict selection requirements to ensure that only high quality,  
1314 well measured objects are used. For leptons, a baseline selection is defined (called the *preselection*),  
1315 which all leptons must pass in order to be considered for the analysis. This preselection is an  
1316 intentionally loose set of criteria designed to have high acceptance in order to reject backgrounds  
1317 with additional leptons (i.e.  $WZ \rightarrow 3l\nu jj$ ). Signal leptons are then required to satisfy a much  
1318 tighter *signal selection* aimed at suppressing backgrounds from non-prompt or fake leptons. A third  
1319 set of lepton selection criteria, the *loose selection*, defines a sample enriched in non-prompt leptons,  
1320 and it is used in the fake-factor method for estimating the non-prompt background, discussed in  
1321 detail in Section 5.3.4. Jets are only required to pass one set of selection criteria. These selections  
1322 are detailed in the following sections and summarized in Table 5.3 for muons, Table 5.4 for electrons,  
1323 and Table 5.5 for jets.

1324 **5.2.1.1 Muon candidate selection**

1325 Cuts on muon  $p_T$  serve to reject low momentum leptons from background processes and additional  
1326 collisions from pileup events. Preselected muons must have transverse momentum  $p_T > 6$  GeV, and  
1327 the signal muons must pass  $p_T > 27$  GeV. The  $p_T$  requirement for loose muons is lower than for  
1328 signal muons, at  $p_T > 15$  GeV, for reasons that are discussed in Section 5.3.4.3. Muons are required  
1329 to fall within the detector's  $\eta$  acceptance:  $|\eta| < 2.7$  for preselected muons, which is tightened to  
1330  $|\eta| < 2.5$  for the signal muons.

1331 Cuts on the transverse and longitudinal impact parameters are applied to ensure that the can-  
1332 didate muon originated from the primary particle interaction and not some other source, such as a  
1333 heavy flavor decay. The preselection and the loose selection both have relaxed requirements on the  
1334 transverse impact parameter significance ( $d_0/\sigma_{d_0}$ ) than the signal selection; all three have the same  
1335 requirement on the transverse impact parameter ( $|z_0 \times \sin \theta|$ ).

1336 Finally, the muon candidates are required to pass a particle identification and an isolation criteria  
1337 as defined in [71]. The methods used in constructing the identification and isolation working points  
1338 are described in more detail in Section 3.2.4.2. The muon identification serves to select prompt

1339 muons with high efficiency and well measured momenta. This analysis uses two different working  
 1340 points: **Loose** for preselected muons and **Medium** for loose and signal muons, where **Medium** muons  
 1341 are a tighter subset of those that pass the **Loose** requirement. Muon isolation is a measurement  
 1342 of detector activity around the muon candidate, and it is measured with both track-based and  
 1343 calorimeter-based variables. The isolation working point used for the signal muons, **Gradient**, is  
 1344 defined such that there is 90% or better background rejection efficiency for 25 GeV muons, and 99%  
 1345 efficiency at 60 GeV. There is no minimum isolation requirement for preselected or loose muons.  
 1346 Loose muons are additionally required to fail one or both of the signal transverse impact parameter  
 1347 cut and signal isolation requirement.

Muon preselection	
Momentum cut	$p_T > 6$ GeV
Angular acceptance	$ \eta  < 2.7$
Longitudinal impact parameter	$ z_0 \times \sin \theta  < 0.5$ mm
Transverse impact parameter	$d_0/\sigma_{d_0} < 10$
Particle identification	<b>Loose</b>

Muon signal selection	
Momentum cut	$p_T > 27$ GeV
Angular acceptance	$ \eta  < 2.5$
Longitudinal impact parameter	$ z_0 \times \sin \theta  < 0.5$ mm
Transverse impact parameter	$d_0/\sigma_{d_0} < 3$
Particle identification	<b>Medium</b>
Particle isolation	<b>Gradient</b>

Muon loose selection	
Momentum cut	$p_T > 15$ GeV
Angular acceptance	$ \eta  < 2.5$
Longitudinal impact parameter	$ z_0 \times \sin \theta  < 0.5$ mm
Transverse impact parameter	$d_0/\sigma_{d_0} < 10$
Particle identification	<b>Medium</b>
Fail signal transverse impact parameter and/or isolation cuts	

Table 5.3: Muon selection criteria. All muons are required to pass the preselection (top), and then either the signal (middle) or loose (bottom) criteria is applied to the preselected electrons.

### 1348 5.2.1.2 Electron candidate selection

1349 The electron candidate selections are very similar to those for muons. The  $p_T$  cut starts at  $p_T >$   
 1350 6 GeV for the preselection, increases to  $p_T > 20$  GeV for loose electrons, and finally to  $p_T > 27$  GeV

for signal electrons. The  $|\eta|$  cut for electrons requires  $|\eta| < 2.47$  for all electrons, with the region  $1.37 \leq |\eta| \leq 1.52$  removed from loose and signal electrons. This is where the electromagnetic calorimeter transitions from the barrel to the endcaps and is not fully instrumented. Both the transverse and longitudinal impact parameter cuts are the same for all electron selections.

The electron particle identification uses a multivariate likelihood technique (LH) [72] detailed in Section 3.2.4.3. Preselected electrons must pass the `LooseLH` working point with an additional requirement that there be a reconstructed track hit in the first layer of the pixel detector (a so-called  $B$ -layer hit). The LH requirement for the loose and signal electrons increases in tightness using `MediumLH` and `TightLH` electrons, respectively. As for isolation, the `Gradient` working point is required for signal electrons only. The loose electrons must fail one or both of the signal identification and isolation requirements.

Electron preselection	
Momentum cut	$p_T > 6$ GeV
Angular acceptance	$ \eta  < 2.47$
Longitudinal impact parameter	$ z_0 \times \sin \theta  < 0.5$ mm
Transverse impact parameter	$d_0/\sigma_{d_0} < 5$
Particle identification	<code>LooseLH</code> + $B$ -layer hit

Electron signal selection	
Momentum cut	$p_T > 27$ GeV
Angular acceptance	$ \eta  < 2.47$ , excluding $1.37 \leq  \eta  \leq 1.52$
Longitudinal impact parameter	$ z_0 \times \sin \theta  < 0.5$ mm
Transverse impact parameter	$d_0/\sigma_{d_0} < 5$
Particle identification	<code>TightLH</code>
Particle isolation	<code>Gradient</code>

Electron loose selection	
Momentum cut	$p_T > 20$ GeV
Angular acceptance	$ \eta  < 2.47$ , excluding $1.37 \leq  \eta  \leq 1.52$
Longitudinal impact parameter	$ z_0 \times \sin \theta  < 0.5$ mm
Transverse impact parameter	$d_0/\sigma_{d_0} < 5$
Particle identification	<code>MediumLH</code>
Fail signal identification and/or isolation cuts	

Table 5.4: Electron selection criteria. All electrons are required to pass the preselection (top), and then either the signal (middle) or loose (bottom) criteria is applied to the preselected electrons.

---

1362   **5.2.1.3 Jet candidate selection**

1363   The final objects that need to pass selection are jets. Jets are clustered using the anti- $k_t$  algo-  
1364   rithm [73] within a radius of  $\Delta R = 0.4$ . The jets are then calibrated using  $E_T$ - and  $\eta$ -dependent  
1365   correction factors that are trained using MC simulations [74]. The calibrated jets are required to have  
1366    $p_T > 30$  GeV if they lie in the forward regions of the detector ( $2.4 < |\eta| < 4.5$ ) and  $p_T > 25$  GeV in  
1367   the central region ( $|\eta| \leq 2.4$ ). In order to suppress pileup jets, the so-called jet-vertex-tagger (JVT)  
1368   discriminant associates a jet with the primary interaction vertex [75]; central jets with  $p_T > 60$  GeV  
1369   are required to pass the `Medium` JVT working point, which corresponds to an average efficiency  
1370   of over 92%. Finally, the jets are required to be separated from the selected leptons by at least  
1371    $\Delta R(j, l) > 0.3$ .

Jet selection	
Momentum cut	$p_T > 30$ GeV for $2.4 <  \eta  < 4.5$ $p_T > 60$ GeV for $ \eta  < 2.4$
JVT cut	<code>Medium</code>
Jet-lepton separation	$\Delta R(j, l) > 0.3$

Table 5.5: Jet selection criteria. All jets are required to pass the above selection in order to be used in the analysis.

---

1372   **5.2.1.4 Treatment of overlapping objects**

1373   In the event that one or more objects are reconstructed very close to each other, there is the possibility  
1374   for double-counting if both originated from the same object. The procedure by which this ambiguity  
1375   is resolved is called *overlap removal* (OR). The standard ATLAS recommendation for OR [76, 77]  
1376   is implemented in this analysis and is summarized in Table 5.6.

1377   Since electrons leave a shower in the EM calorimeter, every electron has a jet associated with  
1378   it. Therefore, any jets close to an electron (within  $\Delta R(e, j) < 0.2$ ) are rejected due to the high  
1379   probability that they are the same object. On the other hand, when jets and electrons overlap  
1380   within a larger radius of  $0.2 < \Delta R(e, j) < 0.4$ , it is likely that the electron and jet both are part of  
1381   a heavy-flavor decay, and the electron is rejected.

1382   High energy muons can produce photons via bremsstrahlung radiation or collinear final state  
1383   radiation which result in nearby energy deposits in the calorimeters. Non-prompt muons from  
1384   hadronic decays produce a similar signature; however, in this case the jet has a higher track multi-  
1385   plicity in the ID. It is possible to address both cases simultaneously by rejecting the jet when the ID

1386 track multiplicity is less than three—and otherwise rejecting the muon—for jets and muons within  
 1387  $\Delta R(\mu, j) < 0.4$ .

1388 In addition to the case above where muon bremsstrahlung results in a nearby reconstructed jet,  
 1389 the ID track from the muon and the calorimeter energy deposit can lead to it being reconstructed  
 1390 as an electron. In this case, if both a muon and an electron share a track in the ID, the muon is  
 1391 kept and the electron is rejected, unless the muon is calorimeter-tagged<sup>12</sup>, in which case the muon  
 1392 is removed in favor of the electron.

Overlap	Check	Result (remove → keep)
Electron & Jet	$\Delta R(e, j) < 0.2$	Jet → Electron
	$0.2 < \Delta R(e, j) < 0.4$	Electron → Jet
Muon & Jet	$\Delta R(\mu, j) < 0.4$ and Jet $N_{ID}$ tracks $< 3$	Jet → Muon
	$\Delta R(\mu, j) < 0.4$ and Jet $N_{ID}$ tracks $\geq 3$	Muon → Jet
Electron & Muon	Shared ID track	Electron → Muon
	Shared ID track & muon is calo-tagged	Muon → Electron

Table 5.6: Summary of the overlap removal procedure used in the analysis. If the criteria in the “check” column is met, in the “result” column, the object on the left of the arrow is removed in favor of the object on the right.

### 1393 5.2.2 Signal event selection

1394 After the objects have been selected, cuts are applied on a per-event level to select  $W^\pm W^\pm jj$  signal  
 1395 events. The event selection is summarized in Table 5.8.

1396 The initial event selection chooses events that pass one or more of the trigger requirements listed  
 1397 in Table 5.7. At least one signal lepton is “matched” to a passed trigger in order to ensure that  
 1398 it was indeed a signal lepton that fired the trigger. A collection of *event cleaning* cuts must also  
 1399 be passed in order to remove events collected during periods in which one or more components of  
 1400 the detector was not operating optimally. Finally, the events are required to contain at least one  
 1401 interaction vertex. An event can have multiple reconstructed vertices from additional proton-proton  
 1402 collisions that occurred in the same bunch crossing. In this case, the *primary vertex* is determined  
 1403 by choosing the vertex with the largest sum of the  $p_T^2$  of its associated tracks.

1404 Events are then required to contain exactly two signal leptons with the same electric charge.  
 1405 The dilepton pair must have a combined invariant mass of  $m_{ll} \geq 20$  GeV in order to suppress low  
 1406 mass Drell-Yan backgrounds. Two additional selections are applied to events in the ee-channel:

<sup>12</sup>A calorimeter-tagged (CT) muon is a muon that is identified by matching an ID track to a calorimeter energy deposit. CT muons have relatively low reconstruction efficiency compared to those measured by the MS, but can be used to recover acceptance in regions of the detector where the MS does not have full coverage [71].

	2015 data	2016 data
Electrons	$p_T > 24$ GeV and Medium ID	$p_T > 26$ GeV and Tight ID and Loose isolation
	$p_T > 60$ GeV and Medium ID	$p_T > 60$ GeV and Medium ID
	$p_T > 120$ GeV and Loose ID	$p_T > 140$ GeV and Loose ID
Muons	$p_T > 20$ GeV and Loose isolation $p_T > 50$ GeV	$p_T > 26$ GeV and Medium isolation $p_T > 50$ GeV

Table 5.7: Summary of trigger requirements for electrons and muons for  $\sqrt{s} = 13$  TeV data collected in 2015 and 2016. At least one of the triggers must be satisfied.

1407 both electrons are required to have  $|\eta| < 1.37$  with an invariant mass at least 15 GeV away from  
 1408 the  $Z$ -boson mass to reduce events where one electron is reconstructed with the wrong charge (this  
 1409 background will be discussed in more detail in Section 5.3.3). To suppress backgrounds from final  
 1410 states with more than two leptons, such as  $WZ$  or  $ZZ$ , events with more than two leptons passing  
 1411 the preselection are vetoed.

1412 Missing transverse energy ( $E_T^{\text{miss}}$ ) represents any particles that escape the detector without being  
 1413 measured, such as neutrinos, and it is defined as the magnitude of the vector sum of transverse  
 1414 momenta of all reconstructed objects. It can be difficult to calculate accurately, as it involves  
 1415 measurements from all subsystems within the detector, and it is sensitive to any corrections that  
 1416 may be applied to the reconstructed physics objects [78]. These corrections, including the momentum  
 1417 smearing for muons, energy scale and smearing for electrons, and jet calibrations, are propagated  
 1418 to the  $E_T^{\text{miss}}$  calculation. Events are required to contain  $E_T^{\text{miss}} > 30$  GeV in order to account for the  
 1419 two neutrinos from the  $W$  boson decays.

1420 At least two jets are required. The leading and subleading jets must have  $p_T > 65$  GeV and  
 1421  $p_T > 35$  GeV, respectively, and are referred to as the *tagging jets*. Events are vetoed if they contain  
 1422 one or more jets that have been tagged as a  $b$ -jet to suppress backgrounds from heavy flavor decays  
 1423 (especially top quark events). The  $b$ -tagging algorithm used by ATLAS is a boosted decision tree  
 1424 (BDT) called MV2c10, and this analysis uses a working point with 85% efficiency [79].

1425 Finally, cuts are applied on the VBS signature outlined in Section 5.0.2. The tagging jets are  
 1426 required to have a dijet invariant mass  $m_{jj} > 200$  GeV and be separated in rapidity by  $|\Delta y_{jj}| > 2.0$ .  
 1427 This preferentially selects the VBS EWK events over the QCD-produced  $W^\pm W^\pm jj$  events.

### 1428 5.3 Background estimations

1429 The major sources of background events are summarized in Section 5.0.3, and the methods used to  
 1430 estimate them are detailed in this section. Prompt backgrounds from  $ZZ$  and  $t\bar{t} + V$  are estimated

Event selection	
Event preselection	Pass at least one trigger with a matched lepton Pass event cleaning At least one reconstructed vertex
Lepton selection	Exactly two leptons passing signal selection Both signal leptons with the same electric charge $ \eta  < 1.37$ and $ M_{ee} - M_Z  > 15$ GeV (ee-channel only) Veto events with more than two preselected leptons
Missing transverse energy	$E_T^{\text{miss}} \geq 30$ GeV
Jet selection	At least two jets Leading jet $p_T > 65$ GeV Subleading jet $p_T > 35$ GeV $m_{jj} > 200$ GeV $N_{b\text{-jet}} = 0$ $ \Delta y_{jj}  > 2.0$

Table 5.8: The signal event selection.

1431 directly from MC simulations. The shape of the  $WZ$  and  $V\gamma$  backgrounds are taken from MC, and  
 1432 the predicted yeilds are normalized to the data predictions in dedicated control regions, as outlined  
 1433 in Sections 5.3.1 and 5.3.2, respectively. Opposite sign events with a charge misidentified electron  
 1434 are estimated by a data-driven background method which is summarized in Section 5.3.3. Finally, a  
 1435 *fake-factor* method is used to estimate the contributions from non-prompt backgrounds and is the  
 1436 subject of Section 5.3.4.

### 1437 5.3.1 Estimation of the $WZ$ background

1438 The dominant background involving prompt leptons comes from  $WZ$ +jets events. The contribution  
 1439 is estimated from MC simulation and normalized to data in a control region enriched in  $WZ$  events.  
 1440 This region is defined by the same event selection as the signal region in Table 5.8, with the following  
 1441 changes applied to increase the purity of the  $WZ$  process:

- 1442 • The third lepton veto is inverted, requiring a third lepton with  $p_T > 15$  GeV
- 1443 • Two of the leptons must make a same-flavor opposite-sign pair. If more than one pair exists,  
 1444 the one with  $m_{ll}$  closest to the  $Z$  boson mass is chosen.
- 1445 • The trilepton invariant mass is required to be  $m_{lll} > 106$  GeV to reduce contributions from  
 1446  $Z\gamma$  and  $Z$ +jets

Once the event yields in the control region are calculated, they are propagated to the final signal region fit, detailed in Section 5.4.1, in a single bin combining all the lepton channels. The systematic uncertainties of the  $WZ$  background are also calculated at this time. The event yields for the  $WZ$  control region are listed in Table 5.9, and distributions of the leading lepton  $p_T$  and  $\eta$  as well as trilepton invariant mass  $m_{lll}$  are found in Figures 5.9 and 5.8, respectively.

Event yields in the $WZ$ control region	
$WZ$	$197.9 \pm 1.4$
$ZZ$	$14.1 \pm 0.3$
Triboson	$1.26 \pm 0.1$
top	$10.8 \pm 1.1$
$Z\gamma$	$3.1 \pm 1.1$
$Z+jets$	$2.5 \pm 1.4$
Total prediction	$229.7 \pm 2.5$
Data	$201 \pm 14.2$

Table 5.9: Event yields in the  $WZ$  control region before normalization. All lepton flavor channels are combined.

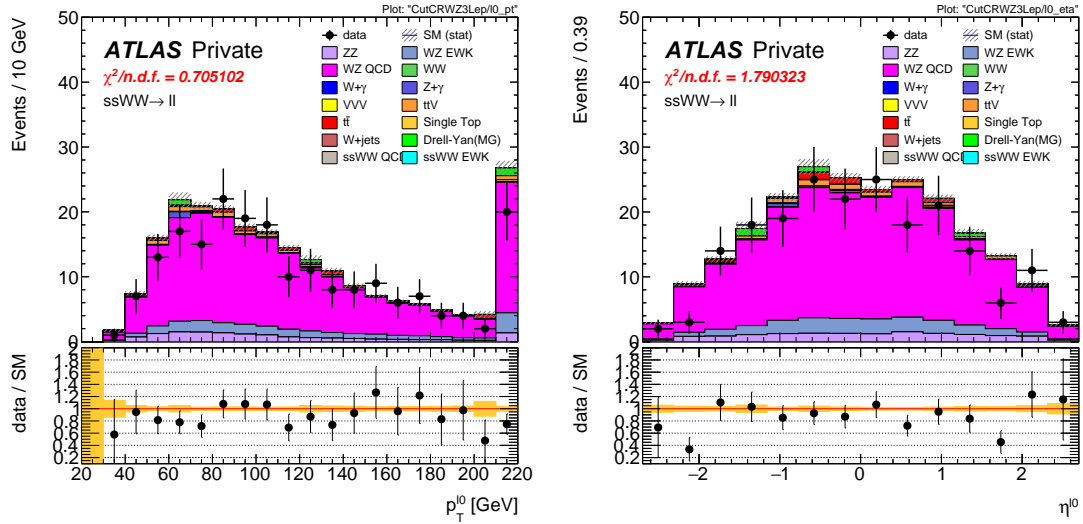


Figure 5.8: Leading lepton  $p_T$  (left) and  $\eta$  (right) distributions in the  $WZ$  control region before normalization. All lepton channels are combined.

### 5.3.2 Estimation of the $V\gamma$ background

Events from  $V\gamma$  processes can pass selection if the photon converts into an  $e^+e^-$  pair and one of the electrons passes the selection criteria. The background is estimated from MC simulations which are

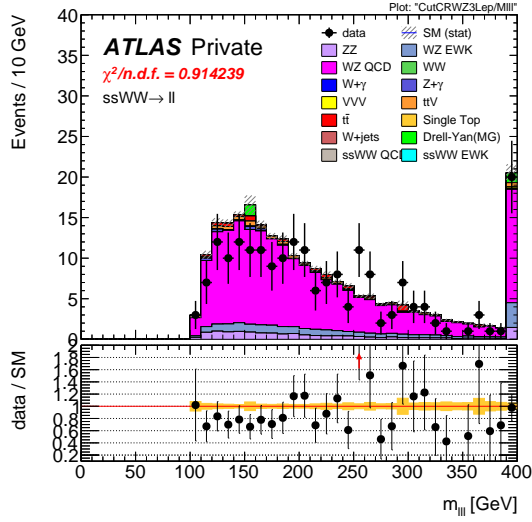


Figure 5.9: Trilepton invariant mass  $m_{lll}$  distribution in the  $WZ$  control region before normalization. All lepton channels are combined.

1455 then scaled by a normalization factor calculated from a control region enriched in  $Z(\mu^+\mu^-)\gamma$  events.  
 1456 This control region selects two opposite-sign muons and an additional electron that is assumed to  
 1457 come from the photon conversion. The full event selection is detailed in Table 5.10.

$V\gamma$ control region
Exactly two muons with $p_T > 27$ GeV and $p_T > 20$ GeV
Exactly one additional electron with $p_T > 15$ GeV
Remove overlap between $Z+jets$ and $Z\gamma$
Di-muon + photon invariant mass $75 < M_{\mu\mu\gamma} < 100$ GeV
$E_T^{\text{miss}} < 30$ GeV

Table 5.10: Selection criteria for the  $V\gamma$  control region.

1458 The  $Z\gamma$  MC samples available do not cover the full range of  $p_T^\gamma$  and  $\Delta R(\gamma, l)$ ; thus, additional  
 1459 Drell-Yan samples ( $Z+jets$ ) are used to fill out the phase space. Overlap between the two samples  
 1460 are removed based to avoid double counting. Events with final state photons are checked at truth  
 1461 level<sup>13</sup> to ensure that the photon did not originate from a hadronic decay. Cuts on  $p_T^\gamma > 10$  GeV and  
 1462  $\Delta R(\gamma, l) > 0.1$  are then applied at generator level, and  $Z\gamma$  events that fail this additional selection  
 1463 and  $Z+jets$  events that pass it are removed.

1464 The normalization factor is calculated directly from the event yields in the  $V\gamma$  control region

<sup>13</sup>Truth particles are the particles produced directly by the MC generator before being passed through the full detector simulation, at which point they are considered *reconstruction-level* (or *reco-level*) particles.

rather than in the signal fit, as is done for the  $WZ$  background. The event yields are listed in Table 5.11, and the normalization factor is determined to be 1.77. No MC events from  $Z\gamma$  processes survive the full event selection; thus, the scaling is only applied to the  $W\gamma$  background in the signal region. A systematic uncertainty of 44% is assigned to the background based off of the uncertainties in the calculation of the normalization factor.

Event yields in the $V\gamma$ control region	
$Z\gamma$	$24.6 \pm 3.3$
$Z+jets$	$3.0 \pm 1.5$
diboson + triboson	$6.7 \pm 0.3$
top	$1.5 \pm 0.5$
Total prediction	$35.8 \pm 3.7$
Data	$57 \pm 7.6$

Table 5.11: Event yields in the  $V\gamma$  control region. The  $V\gamma$  scale factor of 1.77 is calculated by scaling up the  $Z\gamma$  and  $Z+jets$  backgrounds to account for the difference between the data and predicted total background.

### 5.3.3 Estimation of backgrounds from charge misidentification

If an electron's charge is mis-reconstructed, it can lead to a real opposite-sign lepton pair passing the same-sign requirement in the event selection. There are two primary reasons this can occur:

1. An electron emits a photon via bremsstrahlung which then converts into an electron-positron pair, and the conversion track with the wrong electric charge is matched to the original electron. This is the dominant process leading to charge flip, and it is highly dependent on the electron  $\eta$  due to the different amount of detector material the electron passes through.
2. The curvature of the electron's track is mis-measured, resulting in the wrong charge being assigned. This process is dependent on the momentum of the electron, as its track becomes more straight as the momentum of the electron increases.

In order to estimate this background, the rate at which an electron's charge is misidentified is calculated from  $Z \rightarrow e^+e^-$  MC simulation. It is known that the MC does not perfectly model the material effects leading to charge flip; as a result, scale factors are applied to the MC in order for it to better reflect the real performance. These scale factors are obtained from the ratio of charge mis-ID rates in data and uncorrected MC in [50] following the method outlined in [80]. Once the scale factors are applied, the charge misidentification rate  $\varepsilon$  can be extracted by comparing the

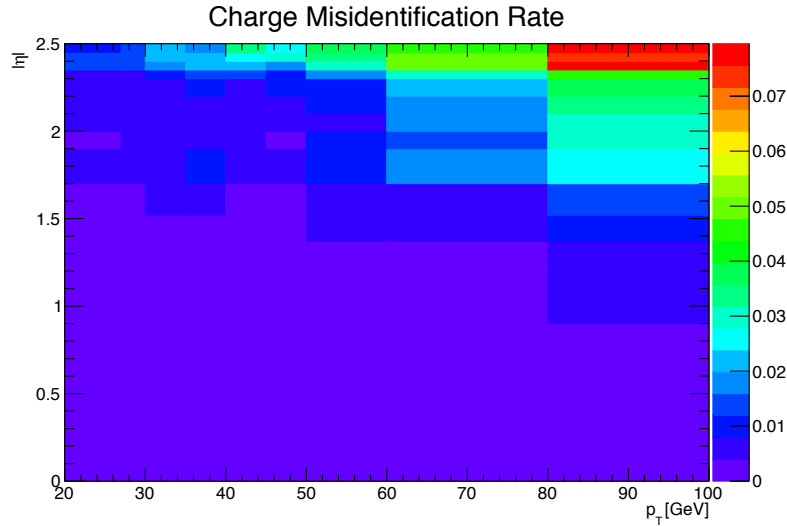


Figure 5.10: Charge misidentification rates for electrons as a function of  $|\eta|$  and  $p_{\text{T}}$ . Rates are calculated from  $Z \rightarrow e^+e^-$  MC after applying scale factors to approximate the charge mis-ID rates in data.

1486 electron's reconstructed charge with the charge of its truth particle:

$$\varepsilon(\eta, p_{\text{T}}) = \frac{N_{\text{wrong charge}}}{N_{\text{prompt electrons}}} \quad (5.1)$$

1487 The charge mis-ID rate is calculated in bins of electron  $|\eta|$  and  $p_{\text{T}}$ , and it varies from below 0.1%  
 1488 in the central region of the detector up to 8% in the forward regions for high  $p_{\text{T}}$  (above 90 GeV)  
 1489 electrons. A two-dimensional plot of  $\varepsilon$  can be found in Figure 5.10.

1490 Given the charge flip rate  $\varepsilon(\eta, p_{\text{T}})$ , the rate at which an electron has its charge correctly recon-  
 1491 structed is  $(1 - \varepsilon)$ . Thus there are three possible combinations of charge identification, assuming a  
 1492 two-electron event:

- 1493 1. Both electrons are reconstructed correctly:  $(1 - \varepsilon)^2$
- 1494 2. Both electrons are mis-reconstructed:  $\varepsilon^2$
- 1495 3. Only one electron is mis-reconstructed:  $2\varepsilon(1 - \varepsilon)$

1496 In order to estimate the size of the background from charge misidentification, opposite-sign events  
 1497 are selected using the default event selection for a given signal or control region with the same-sign  
 1498 requirement inverted. These events are then weighted by the probability for one of the electrons to

1499 be reconstructed with the wrong charge:

$$\omega = \frac{\varepsilon_1(1 - \varepsilon_2) + \varepsilon_2(1 - \varepsilon_1)}{(1 - \varepsilon_1)(1 - \varepsilon_2) + \varepsilon_1\varepsilon_2} \quad (5.2)$$

1500 where the subscripts 1 and 2 refer to the leading and subleading electrons, respectively, and  $\varepsilon_i$  is a  
 1501 function of the  $\eta$  and  $p_T$  of the  $i^{\text{th}}$  electron. In the case of an event with only one electron and one  
 1502 muon, Equation 5.2 simplifies:

$$\omega = \frac{\varepsilon}{1 - \varepsilon} \quad (5.3)$$

1503 This method assumes that there is little contamination from fake electrons in the opposite-sign  
 1504 sample, and this has been verified with MC simulation.

1505 Additionally, charge-flipped electrons tend to be reconstructed with lower energy when compared  
 1506 to electrons with the correct charge. This is due to energy loss from the material interactions that  
 1507 can cause the charge to be misidentified in the first place. A correction factor is calculated from  
 1508 MC simulations, comparing the  $p_T$  of the truth electron to its reconstructed counterpart:

$$\alpha = \frac{\left(\frac{p_T^{\text{reco}}}{p_T^{\text{truth}}} - 1\right)_{\text{correct charge}}}{\left(\frac{p_T^{\text{reco}}}{p_T^{\text{truth}}} - 1\right)_{\text{wrong charge}}} \quad (5.4)$$

1509 The correction is then applied to the  $p_T$  of the charge-flipped electron via

$$p_T = p_T^0 / (1 + \alpha) + dE \quad (5.5)$$

1510 where  $p_T^0$  is the uncorrected  $p_T$  of the electron and  $dE$  is a gaussian smearing factor centered at zero  
 1511 with a width related to the energy resolution. Since which electron is mis-reconstructed is never  
 1512 determined in this method, in the case of a two-electron event, the energy correction is applied  
 1513 randomly to one of the two electrons based on the probabilities for them to be charge-flipped. This  
 1514 also determines the overall sign of the event; the charge of the electron that does not receive the  
 1515 correction is taken to be the charge for both.

1516 Systematic uncertainties on the charge mis-ID rates are calculated by generating two additional  
 1517 sets of rates with the uncertainties on the scale factors varied up and down. The size of the esti-  
 1518 mated charge flip background without the energy correction applied is also taken as a systematic  
 1519 uncertainty. These systematic uncertainties are estimated to be approximately  $\pm 15\%$ .

### 1520 5.3.3.1 Validation of the charge misidentification estimate

1521 The performance of the charge misidentification estimation is tested in the same-sign inclusive  
 1522 validation region (VR), defined in Table 5.12. For  $ee$  events, the mass of the dilepton pair is required

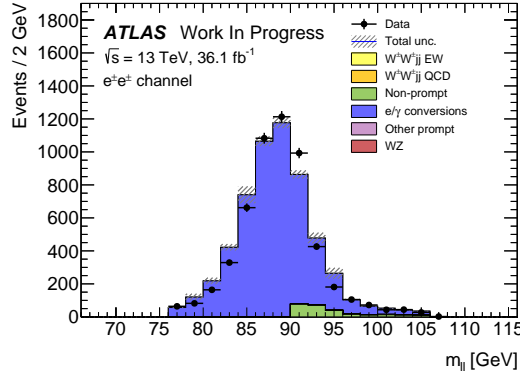


Figure 5.11: Dilepton invariant mass distribution  $m_{ll}$  for the  $ee$  channel in the same-sign inclusive VR.

1523 to lie within 15 GeV of the  $Z$  boson mass to increase the purity of the charge flip background.  
 1524  $t\bar{t}$  production, which can contribute to both the charge mis-ID and fake lepton backgrounds, is  
 1525 suppressed by the  $b$ -jet veto. The di-electron invariant mass is shown in Figure 5.11, and distributions  
 1526 of the leading and subleading electron  $p_T$  in the  $ee$ -channel are shown in Figure 5.12 with the  $Z$   
 1527 mass cut inverted. Agreement between data and prediction is seen within the total statistical and  
 1528 systematic uncertainties in the VR.

Same-sign inclusive VR
Exactly 2 same-sign signal leptons
$p_T > 27$ GeV for both leptons
$m_{ll} > 20$ GeV
$ m_{ee} - m_Z  > 15$ GeV ( $e^\pm e^\pm$ -channel only)
$N_{b\text{-jet}} = 0$

Table 5.12: Selection criteria for the same-sign inclusive validation region.

### 1529 5.3.4 Estimation of non-prompt backgrounds with the fake-factor method

1530 Events with one prompt lepton produced in association with hadronic jets can pass the event selection  
 1531 if a jet is misidentified as a charged lepton or if a non-prompt lepton from the decay of a heavy  
 1532 flavor particle (such as  $b$ - and  $c$ -hadrons) passes the signal lepton criteria. These misidentified jets  
 1533 and non-prompt leptons are collectively referred to as *fake leptons*, or simply *fakes*. The rate at  
 1534 which a fake lepton is misidentified is generally not modelled well enough by the MC to accurately  
 1535 estimate their contributions directly from simulation. Therefore, a data-driven technique called the

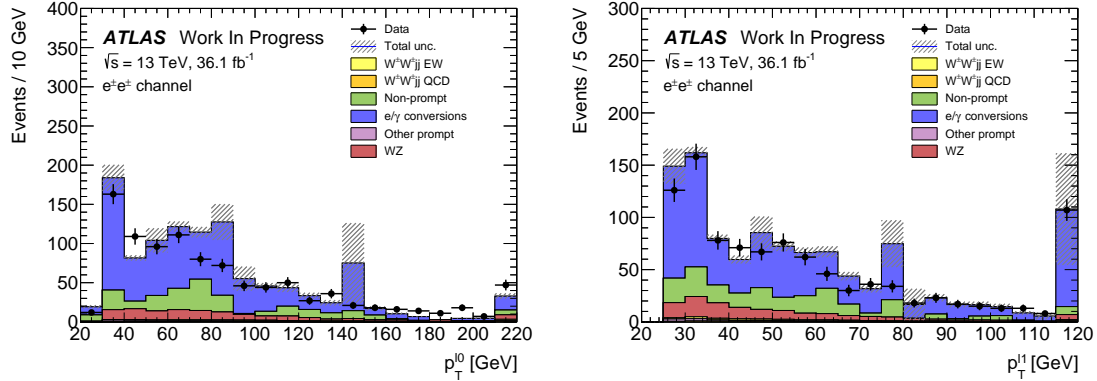


Figure 5.12:  $p_T$  distributions for the leading (left) and subleading (right) electron for the  $ee$  channel in the same-sign inclusive VR. In these plots, the cut requiring  $m_{ee}$  to fall within the  $Z$  mass window has been inverted in order to test the modelling away from the  $Z$  peak.

1536 *fake-factor* is used to estimate the size and shape of background processes from fake leptons. In  
 1537 this analysis, a new modification to the fake-factor is used involving the particle isolation variables;  
 1538 the method is outlined in the context of the *default* fake-factor in Section 5.3.4.1, and the modified  
 1539 fake-factor is outlined in Section 5.3.4.2.

#### 1540 5.3.4.1 Overview of the default fake-factor method

1541 The goal of the fake-factor method is to measure the fake rate from real collision events in a region  
 1542 enriched in fake leptons and use it to estimate the size of the fake lepton background in a chosen  
 1543 signal or control region. This is done by creating two samples using different lepton definitions:

- 1544 1. The *nominal* sample is made up of leptons passing the signal selection.  
 1545 2. The *loose* sample is made up of leptons that fail the signal selection while still passing a  
 1546 loosened set of criteria. This sample is enriched in fake leptons and is orthogonal to the set of  
 1547 signal leptons.

1548 Using the sets of nominal and loose leptons, a fake-factor  $f$  can be calculated in a region enriched  
 1549 in processes that are prone to producing fake leptons:

$$f = \frac{N_{\text{nominal}}}{N_{\text{loose}}} \quad (5.6)$$

1550 Since the fake rate is not expected to be constant over the entire phase space, the fake-factor can  
 1551 be divided into bins:

$$f(b) = \frac{N_{\text{nominal}}(b)}{N_{\text{loose}}(b)} \quad (5.7)$$

1552 where  $b$  represents the bin number. In this analysis, the fake-factor is binned in lepton  $p_T$ .

1553 In order to estimate the fake background contribution in a given signal or control region, the  
 1554 fake-factor is applied to a second control region with a selection identical to the region of interest  
 1555 except one of the leptons required to satisfy the loose criteria. The region for which the background  
 1556 is estimated contains two nominal leptons and is referred to as *nominal+nominal* ( $NN$ ), and the  
 1557 associated control region where the fake-factor is applied contains one nominal and one loose lepton  
 1558 and is referred to as *nominal+loose* ( $NL$ ). The fake background in a  $NN$  region can then be  
 1559 calculated as:

$$N_{NN}^{\text{fake bkg.}} = \sum_b f(b) N_{NL}(b) \quad (5.8)$$

1560 Backgrounds containing two prompt leptons can also enter the  $NL$  region if one of the leptons  
 1561 passes the nominal selection and the other passes the loose selection. Since the fake-factor method  
 1562 estimates the fake background by scaling the amount of non-prompt events in the  $NL$  region, if these  
 1563 prompt contributions are not removed, they will be included in the scaling and the background  
 1564 will be overpredicted. The final estimate of the fake background becomes:

$$N_{NN}^{\text{fake bkg.}} = \sum_b f(b) (N_{NL}(b) - N_{NL}^{\text{prompt}}(b)) \quad (5.9)$$

#### 1565 5.3.4.2 The fake-factor with $p_T^{\text{cone}}$

1566 When a jet produces a non-prompt lepton, that lepton only carries a fraction of the underlying jet's  
 1567 total momentum. Due to the isolation cut applied to the nominal leptons, they typically carry a  
 1568 much larger percentage of the underlying jet momentum than the loose leptons. Since the isolation  
 1569 essentially sets a limit on the amount of detector activity allowed around the lepton, if other nearby  
 1570 particles carried a significant amount of momentum, the lepton would likely fail this cut.

1571 This discrepancy in the underlying jet momentum fraction can cause problems in the calculation  
 1572 of the fake-factor  $f$ . Consider the case where two separate events have jets of identical momentum,  
 1573 but one produces a non-prompt lepton that passes the nominal selection, and the other produces a  
 1574 non-prompt lepton that passes the loose selection. The loose lepton on average will have lower  $p_T$   
 1575 than the nominal lepton despite both originating from jets with the same momentum. This can be  
 1576 seen explicitly when comparing the  $p_T$  of a muon to its associated truth jet:

$$\Delta p_T(\mu, j) = \frac{p_T(j) - p_T(\mu)}{p_T(j) + p_T(\mu)} \quad (5.10)$$

1577 Since muons are not included in the jet reconstruction algorithm,  $\Delta p_T$  approximates the momentum  
 1578 of the muon compared to the rest of the jet. For muons that carry more than 50% of the jet's

momentum,  $\Delta p_T$  will be negative and vice-versa. The  $\Delta p_T$  distributions for nominal and loose muons in  $t\bar{t}$  MC events is shown Figure 5.13, where a 50 GeV jet on average corresponds to a 35 GeV nominal muon and a 20 GeV loose muon<sup>14</sup>.

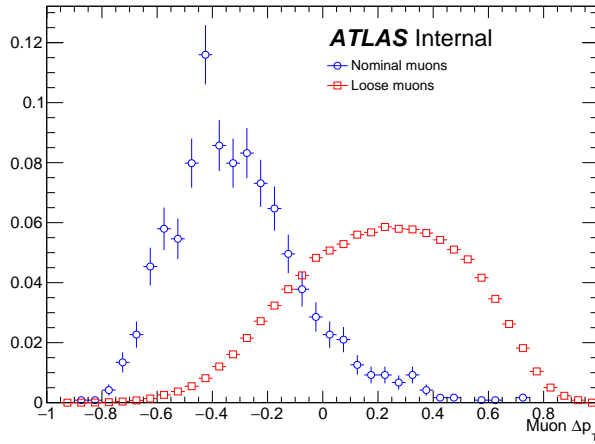


Figure 5.13:  $\Delta p_T$  distributions for nominal (blue) and loose (red) muons in simulated  $t\bar{t}$  events. Each muon has been matched to a truth-level jet. Both distributions are normalized to unit area.

Since the default fake-factor defined in Equation 5.7 is binned in lepton  $p_T$ , within a given bin, the underlying jet  $p_T$  spectrum can differ substantially between the numerator and the denominator. Additionally, these differences can vary depending on the process producing the non-prompt leptons or on the specific kinematic selections of the signal or control regions where the fake-factor is applied.

Fortunately, the majority of the jet momentum not carried by the non-prompt lepton (excluding neutrinos) can be recovered using isolation variables. A track-based isolation is chosen, referred to as  $p_T^{\text{cone}}$ , and it contains the sum of the  $p_T$  of all particle tracks originating from the primary vertex within a cone of  $\Delta R < 0.3$  around the lepton. Thus, the sample of loose leptons in the denominator of the fake-factor calculation is binned in  $p_T + p_T^{\text{cone}}$  rather than simply lepton  $p_T$ . Adding the isolation cone greatly reduces the difference in the fraction of the underlying jet momentum carried by the nominal and loose leptons. To check this, a new  $\Delta p_T$  is calculated between a lepton and its matched truth jet, where the truth jet  $p_T$  has been corrected to include all muons within a cone of  $\Delta R < 0.4$ :

$$p_T(j) = p_T(j_{\text{truth}}) + \sum_{\Delta R < 0.4} p_T(\mu_{\text{truth}}) \quad (5.11)$$

<sup>14</sup>To better illustrate the point, here the muon is added back into the jet  $p_T$ , and the corresponding muon  $p_T$  is obtained via  $\Delta p_T(\mu, j) = \frac{(p_T(j) - p_T\mu) - p_T(\mu)}{(p_T(j) - p_T\mu) + p_T(\mu)} = \frac{p_T(j) - 2p_T(\mu)}{p_T(j)}$ .

1595 The  $\Delta p_T$  distributions comparing  $p_T$  and  $p_T + p_T^{\text{cone}}$  for nominal and loose leptons using the corrected  
 1596 jet  $p_T$  are found in Figure 5.14, and better agreement is seen between the numerator (nominal) and  
 1597 denominator (loose with  $p_T + p_T^{\text{cone}}$ ) distributions.

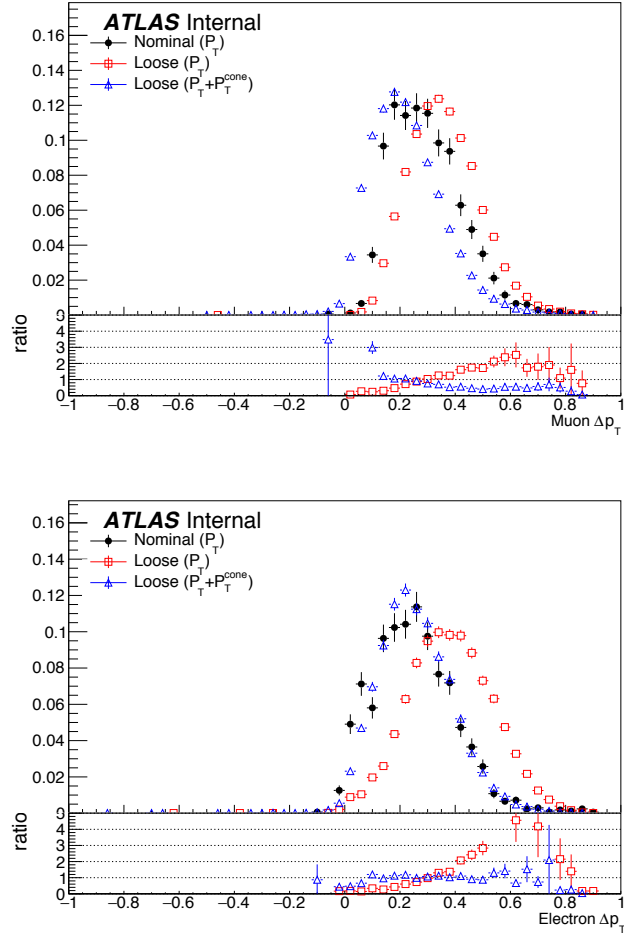


Figure 5.14:  $\Delta p_T$  distributions for muons (top) and electrons (bottom) in simulated  $t\bar{t}$  events. Each lepton has been matched to a truth-level jet, and that truth jet has had its  $p_T$  corrected to include all truth muons within a cone of  $\Delta R < 0.4$ . The nominal leptons are in black.  $\Delta p_T$  is calculated for the loose leptons using  $p_T$  (red) and  $p_T + p_T^{\text{cone}}$  (blue).

1598 The numerator remains binned in lepton  $p_T$ , due to the fact that it is meant to mirror the signal  
 1599 region as closely as possible, and the signal lepton selection does not use  $p_T + p_T^{\text{cone}}$ . The impact of  
 1600 this is expected to be negligible due to the  $p_T^{\text{cone}}$  isolation being small for signal leptons, as shown

for muons in Figure 5.15. Finally, the fake-factor  $f$  becomes:

$$f(b) = \frac{N_{\text{nominal}}(b(p_T))}{N_{\text{loose}}(b(p_T + p_T^{\text{cone}}))} \quad (5.12)$$

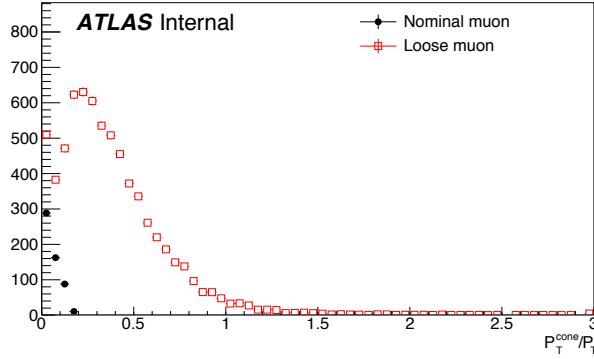


Figure 5.15: Distributions of  $p_T^{\text{cone}}/p_T$  for nominal (black) and loose (red) muons in simulated  $t\bar{t}$  events.

#### 5.3.4.3 Application of the fake-factor

The fake-factor itself is measured from a sample of events passing a dijet selection requiring exactly one lepton (either passing the nominal or loose selections) and at least one jet. The leading jet must also be  $b$ -tagged and approximately back-to-back with the lepton in order to enhance non-prompt lepton contributions while reducing contributions from processes involving  $W$  and  $Z$  bosons.  $W$  boson events are further suppressed by requiring the sum of the  $E_T^{\text{miss}}$  and the transverse mass of the lepton to be less than 50 GeV. The full event selection for the dijet region is summarized in Table 5.13.

The numerator sample is constructed from dijet events in which the lepton passes the nominal (signal) selection and is binned in the lepton  $p_T$ . Similarly, the denominator sample is made up of the remaining dijet events where the lepton passes the loose selection and is binned in the lepton  $p_T + p_T^{\text{cone}}$ . The nominal and loose leptons pass the signal selection<sup>15</sup> and loose selection, respectively, defined earlier in Table 5.3 for muons and Table 5.4 for electrons. Backgrounds from  $W + \text{jets}$ ,  $Z + \text{jets}$ ,  $t\bar{t}$ , and single top processes are estimated from MC simulations requiring one lepton to be prompt using the truth information; these contributions are subtracted from the dijet data. The

<sup>15</sup>The  $p_T > 27$  GeV cut in the signal lepton selection is dropped in favor of the  $p_T > 15$  GeV requirement in the dijet selection.

Dijet event selection
Event preselection
Exactly one lepton with $p_T > 15$ GeV
$N_{\text{jet}} > 0$
Leading jet is $b$ -tagged
$p_T^{\text{lead. jet}} > 25$ GeV
$p_T^{\text{lead. jet}} > 30$ GeV if $ \eta_j  > 2.5$
$ \Delta\phi(l, \text{lead. jet})  > 2.8$
$m_T(l, E_T^{\text{miss}}) + E_T^{\text{miss}} < 50$ GeV

Table 5.13: Event selection for the dijet region used for calculating the fake-factor. The selected lepton can pass either the nominal (signal) or loose selections. In the case of the nominal leptons, the  $p_T > 27$  GeV requirement is replaced with  $p_T > 15$  GeV.

1617 fake-factor is then calculated using Equation 5.12 for muons and for central and forward electrons  
 1618 separately. The muon fake-factor is shown in Figure 5.16, and the two electron fake-factors are shown  
 1619 in Figure 5.17. The numerical values of the fake-factors, including their systematic uncertainties  
 1620 which will be discussed in Section 5.3.4.4, are listed in Table 5.14.

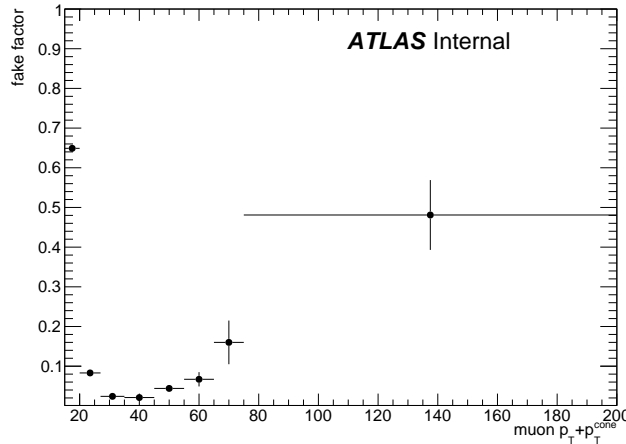


Figure 5.16: The measured fake-factor as a function of muon  $p_T + p_T^{\text{cone}}$ . The error bars represent the statistical uncertainty only.

1621 In order to properly account for the denominator being binned in  $p_T + p_T^{\text{cone}}$ , special care needs  
 1622 to be taken when estimating the fake background from the  $NL$  regions. For the purposes of the  
 1623 fake-factor calculation, it is perhaps more intuitive to consider a loose *object* with  $p_T = p_T + p_T^{\text{cone}}$   
 1624 instead of simply a loose *lepton*, as the lepton and the underlying jet are treated as a whole with this  
 1625 method. When the lepton  $p_T$  cuts required by a particular signal or control region are applied to

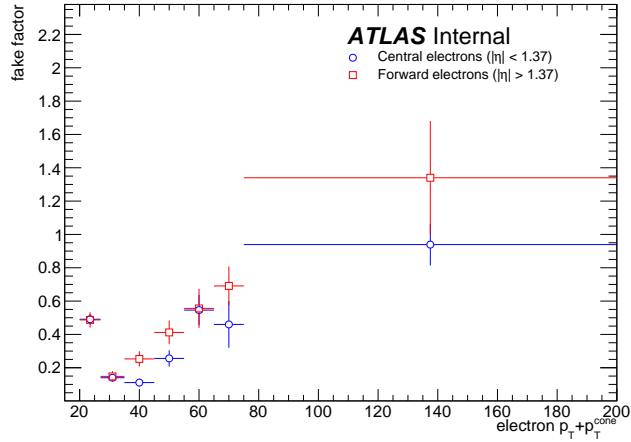


Figure 5.17: The measured fake-factor as a function of electron  $p_T + p_T^{\text{cone}}$  in the central ( $|\eta| < 1.37$ , blue) and forward ( $|\eta| > 1.37$ , red) regions of the detector. The error bars represent the statistical uncertainty only.

nominal and loose leptons, the cut is applied to the  $p_T$  of the nominal lepton and to the  $p_T + p_T^{\text{cone}}$  of the loose object. Similarly, when looking up the fake-factor weight for a given  $NL$  event, the value taken from the bin corresponding to the  $p_T + p_T^{\text{cone}}$  of the loose object. Finally, when applying the weight to the event,  $p_T + p_T^{\text{cone}}$  is assigned as the  $p_T$  of the loose object. Figure 5.18 contains a graphical representation of this procedure.

Finally, it should be noted that the addition of  $p_T^{\text{cone}}$  to the loose object may cause the loose leptons in the denominator sample to migrate into higher bins. This results in an overall decrease in the number of loose objects in the lower  $p_T + p_T^{\text{cone}}$  bins due to there not being additional leptons at lower  $p_T$  to replace them. Since the fake-factor is a ratio of the number of events in a bin, this effect causes the first few bins of the fake-factor to increase, as can be seen clearly in Figure 5.16. However, the signal and control regions (and their corresponding  $NL$  regions) contain a  $p_T > 27$  GeV cut that prevents these migrations from negatively impacting the fake estimation.

#### 5.3.4.4 Systematic uncertainties

Four sources of systematic uncertainty are considered: the dijet event selection, the prompt background subtraction, the jet flavor composition, and residual dependence on the underlying jet  $p_T$  spectrum. In order to measure the impact of these systematics, new fake-factors are computed with each of the systematic variations and the differences from the nominal values are taken as the

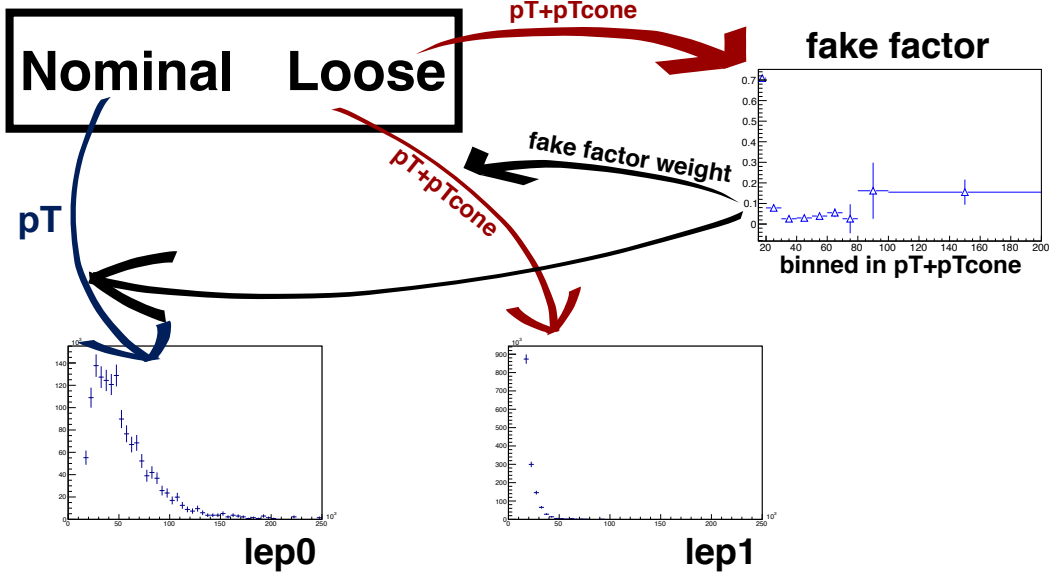


Figure 5.18: Graphical representation of the fake-factor application using  $p_T + p_T^{\text{cone}}$ . The value of  $p_T + p_T^{\text{cone}}$  for the loose lepton is used to “look up” the fake-factor weight which is then applied to the event. The loose lepton’s  $p_T$  becomes  $p_T + p_T^{\text{cone}}$  for the purpose of the fake background estimation.

1643 uncertainty.

- 1644 1. In order to estimate uncertainties due to the dijet selection, the cut on  $M_T + E_T^{\text{miss}}$  is varied  
1645 by  $\pm 5$  GeV, the jet-lepton separation  $\Delta\phi(l, j)$  by  $\pm 0.1$ , and the jet  $p_T$  cut by  $+5$  GeV.
- 1646 2. To estimate the systematic uncertainty on the prompt background subtraction, the MC pre-  
1647 dictions in a  $W$ +jets control region is compared to data. The discrepancy between data and  
1648 MC is found to be approximately 10% [50]. Therefore, the prompt background used for the  
1649 subtraction is scaled up and down by  $\pm 10\%$ .
- 1650 3. The difference in the jet flavor composition between the dijet events and the events in the  
1651  $NL$  regions can affect the accuracy of the fake background estimation. The dijet sample is  
1652 dominated by light jets, while the  $NL$  regions tend to be dominated by heavy flavor from  $t\bar{t}$ .  
1653 To account for this, the fake-factor is computed with a  $b$ -jet veto.
- 1654 4. To measure any residual dependence on the underlying jet  $p_T$  spectrum, the leading jet  $p_T$   
1655 distribution is reweighted to match the  $p_T$  spectrum of truth jets that produce fake leptons  
1656 in MC simulations. This results in an increase in the number of nominal and loose leptons at  
1657 high momentum [50].

fake-factor	$p_T$ [15, 20]	$p_T$ [20, 27]	$p_T$ [27, 35]	$p_T$ [35, 45]	$p_T$ [45, 55]	$p_T$ [55, 65]	$p_T$ [65, 75]	$p_T$ [75, 200]
nominal	0.649 ± 0.007	0.083 ± 0.002	0.024 ± 0.002	0.021 ± 0.003	0.044 ± 0.007	0.067 ± 0.018	0.160 ± 0.055	0.481 ± 0.088
MT+MET	0.649 ± 0.007	0.082 ± 0.002	0.082 ± 0.002	0.020 ± 0.003	0.045 ± 0.007	0.068 ± 0.018	0.207 ± 0.062	0.523 ± 0.086
$\Delta\phi(\ell, j)$	0.645 ± 0.008	0.083 ± 0.003	0.024 ± 0.002	0.021 ± 0.004	0.045 ± 0.008	0.064 ± 0.021	0.064 ± 0.058	0.438 ± 0.092
Jet $p_T$	0.650 ± 0.007	0.083 ± 0.002	0.024 ± 0.002	0.021 ± 0.003	0.045 ± 0.007	0.069 ± 0.018	0.159 ± 0.018	0.481 ± 0.088
$N_{b\text{-jet}} = 0$	0.724 ± 0.003	0.094 ± 0.001	0.035 ± 0.001	0.025 ± 0.002	0.022 ± 0.004	0.060 ± 0.015	0.026 ± 0.053	0.044 ± 0.134
Bkg. subtraction	0.648 ± 0.007	0.083 ± 0.002	0.024 ± 0.002	0.019 ± 0.003	0.037 ± 0.007	0.044 ± 0.019	0.096 ± 0.062	0.370 ± 0.082
Jet $p_T$ Reweighting	0.539 ± 0.077	0.093 ± 0.007	0.025 ± 0.004	0.043 ± 0.019	0.063 ± 0.014	0.085 ± 0.025	0.141 ± 0.110	1.962 ± 0.492

(a) fake-factor for muons.

fake-factor	$p_T$ [20, 27]	$p_T$ [27, 35]	$p_T$ [35, 45]	$p_T$ [45, 55]	$p_T$ [55, 65]	$p_T$ [65, 75]	$p_T$ [75, 200]
nominal	0.491 ± 0.031	0.140 ± 0.020	0.111 ± 0.023	0.256 ± 0.049	0.546 ± 0.091	0.460 ± 0.140	0.939 ± 0.125
MT+MET	0.493 ± 0.030	0.138 ± 0.019	0.115 ± 0.022	0.261 ± 0.045	0.559 ± 0.084	0.656 ± 0.091	0.802 ± 0.016
$\Delta\phi(\ell, j)$	0.488 ± 0.032	0.137 ± 0.020	0.110 ± 0.025	0.283 ± 0.053	0.503 ± 0.097	0.351 ± 0.149	1.117 ± 0.255
Jet $p_T$	0.489 ± 0.035	0.134 ± 0.021	0.105 ± 0.025	0.224 ± 0.048	0.593 ± 0.093	0.356 ± 0.144	0.928 ± 0.177
$N_{b\text{-jet}} = 0$	0.506 ± 0.029	0.140 ± 0.018	0.111 ± 0.022	0.260 ± 0.046	0.545 ± 0.084	0.546 ± 0.120	0.882 ± 0.103
Bkg. subtraction	0.493 ± 0.032	0.146 ± 0.021	0.115 ± 0.024	0.259 ± 0.049	0.550 ± 0.091	0.460 ± 0.140	0.939 ± 0.125
$N_{b\text{-jet}} = 0$	0.387 ± 0.009	0.130 ± 0.008	0.321 ± 0.012	0.473 ± 0.015	0.716 ± 0.180	0.716 ± 0.180	0.716 ± 0.180
Bkg. subtraction	0.488 ± 0.031	0.138 ± 0.020	0.106 ± 0.023	0.248 ± 0.049	0.529 ± 0.092	0.434 ± 0.143	0.888 ± 0.115
Jet $p_T$ Reweighting	0.493 ± 0.031	0.142 ± 0.020	0.115 ± 0.023	0.264 ± 0.049	0.563 ± 0.090	0.485 ± 0.136	0.989 ± 0.132

(b) fake-factor for central electrons ( $|\eta| < 1.37$ ).

fake-factor	$p_T$ [20, 27]	$p_T$ [27, 35]	$p_T$ [35, 45]	$p_T$ [45, 55]	$p_T$ [55, 65]	$p_T$ [65, 75]	$p_T$ [75, 200]
nominal	0.487 ± 0.046	0.148 ± 0.031	0.253 ± 0.046	0.412 ± 0.071	0.556 ± 0.117	0.691 ± 0.117	1.340 ± 0.340
MT+MET	0.483 ± 0.045	0.152 ± 0.031	0.241 ± 0.043	0.443 ± 0.070	0.565 ± 0.106	0.668 ± 0.117	1.075 ± 0.189
$\Delta\phi(\ell, j)$	0.495 ± 0.047	0.156 ± 0.033	0.271 ± 0.052	0.364 ± 0.074	0.664 ± 0.107	0.749 ± 0.056	0.885 ± 0.084
Jet $p_T$	0.471 ± 0.051	0.158 ± 0.035	0.247 ± 0.051	0.474 ± 0.085	0.283 ± 0.107	0.546 ± 0.149	1.189 ± 0.266
$N_{b\text{-jet}} = 0$	0.478 ± 0.042	0.170 ± 0.031	0.274 ± 0.046	0.389 ± 0.066	0.645 ± 0.104	0.757 ± 0.102	1.319 ± 0.326
Bkg. subtraction	0.523 ± 0.048	0.149 ± 0.033	0.235 ± 0.045	0.429 ± 0.073	0.555 ± 0.117	0.691 ± 0.117	1.340 ± 0.340
$N_{b\text{-jet}} = 0$	0.525 ± 0.011	0.234 ± 0.013	0.644 ± 0.016	0.710 ± 0.014	0.274 ± 0.316	0.274 ± 0.316	0.274 ± 0.316
Bkg. subtraction	0.484 ± 0.046	0.146 ± 0.031	0.248 ± 0.046	0.406 ± 0.071	0.545 ± 0.118	0.676 ± 0.118	1.317 ± 0.337
Jet $p_T$ Reweighting	0.328 ± 0.068	0.124 ± 0.048	0.297 ± 0.100	0.234 ± 0.061	0.680 ± 0.092	0.452 ± 0.138	2.385 ± 1.729

(c) fake-factor for forward electrons ( $1.37 < |\eta|$ ).Table 5.14: Values of the fake-factor in each  $p_T$  bin and for each individual systematic source.

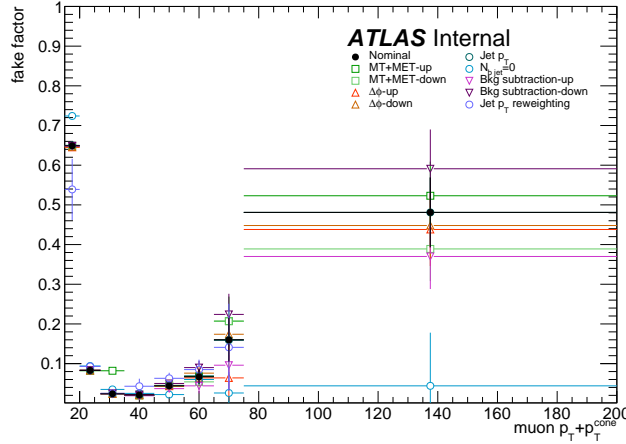


Figure 5.19: Systematic variations in the fake-factor as a function of muon  $p_T + p_T^{\text{cone}}$ . The individual fake-factors obtained for each systematic variation are displayed with their statistical uncertainties.

#### 1658 5.3.4.5 Results of the fake-factor

1659 The fake background contribution in the signal region is estimated by applying the fake-factors  
 1660 to the equivalent  $NL$  region using Equation 5.9, where the fake-factor used corresponds to the  
 1661 flavor of the loose lepton in the event. As usual, the prompt background is subtracted from the  
 1662  $NL$  events using MC simulation. Charge misidentification is handled using the same method as  
 1663 in Section 5.3.3, with an additional set of charge flip rates calculated for loose leptons. The fake  
 1664 background yields in the signal region are listed in Table 5.15. An overall uncertainty of 50% is  
 1665 assigned to the fake background estimation in  $\mu^\pm\mu^\pm$  events, and between 40% to 90% for  $e^\pm e^\pm$  and  
 1666  $\mu^\pm e^\pm$  events, including both statistical and systematic effects.

	estimated yield	$f_e$ stat. up	$f_e$ stat. dn	$f_e$ syst. up	$f_e$ syst. dn	$f_\mu$ stat. up	$f_\mu$ stat. dn	$f_\mu$ syst. up	$f_\mu$ syst. dn
$e^\pm e^\pm$	$11.42 \pm 3.13$	1.69	-1.69	1.67	-5.56	—	—	—	—
$\mu^\pm\mu^\pm$	$4.82 \pm 0.77$	—	—	—	—	0.65	-0.65	3.64	-0.61
$\mu^\pm e^\pm$	$37.08 \pm 5.16$	4.90	-4.90	5.59	-14.34	1.39	-1.39	16.10	-1.98

Table 5.15: Estimated yields for the fake lepton background. The estimated yield is shown in the first column together with the statistical uncertainty followed by the systematic uncertainties from variations of the the fake-factors within their statistical (stat.) and systematic (syst.) uncertainties. The labels  $f_e$  and  $f_\mu$  indicate the fake-factors for electrons and muons, respectively.

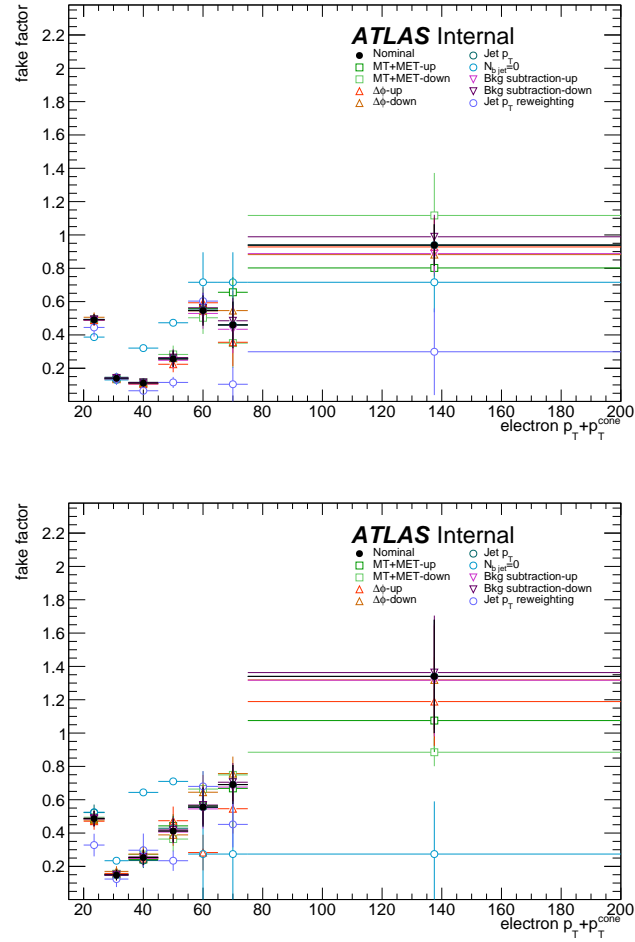


Figure 5.20: Systematic variations in the fake-factor as a function of electron  $p_T + p_T^{\text{cone}}$  in the central ( $|\eta| < 1.37$ , top) and forward ( $|\eta| > 1.37$ , bottom) regions of the detector. The individual fake-factors obtained for each systematic variation are displayed with their statistical uncertainties.

1667 **5.3.4.6 Validation of the fake-factor**

1668 The accuracy of the fake-factor method is tested in several validation regions, the most sensitive  
 1669 of which is the same-sign top fakes VR (SS top VR), defined in Table 5.16. This region inverts  
 1670 the signal region's  $b$ -jet veto to accept events with exactly one  $b$ -jet. Due to this requirement, the  
 1671 dominant source of events comes from the  $t\bar{t}$  process where a  $b$ -jet fakes an isolated lepton. The  
 1672 distribution of the subleading lepton  $p_T$  in this VR is shown in Figure 5.21 for all lepton flavor  
 1673 combinations. There is good agreement between the data and the prediction, even when only taking  
 1674 into account the statistical uncertainty and not the large systematic uncertainties assigned to the  
 1675 fake estimation.

Same-sign top fakes VR
Exactly 2 same-sign signal leptons
$p_T > 27$ GeV for both leptons
$m_{ll} > 20$ GeV
$ m_{ee} - m_Z  > 15$ GeV ( $e^\pm e^\pm$ -channel only)
$N_{b\text{-jet}} = 1$
$N_{\text{jet}} \geq 2$
Leading jet $p_T > 65$ GeV
Subleading jet $p_T > 35$ GeV

Table 5.16: Selection criteria for the same-sign top fakes validation region.

1676 **5.3.5 Reduction of  $WZ$  background using custom overlap removal**

1677 The dominant source of prompt background in this analysis comes from  $WZ$  events where both  
 1678 bosons decay leptonically. Traditionally, the background is dealt with by imposing a veto on any  
 1679 event with a third lepton passing some loose identification criteria (the so-called *trilepton veto*).  
 1680 In the case of this analysis, if one or more leptons in addition to the two signal leptons pass the  
 1681 preselection criteria, the event is rejected. However,  $WZ$  events can still enter the signal region if  
 1682 one of the leptons fails the preselection or falls outside of the detector's acceptance.

1683 In order to understand the sources of  $WZ$  events that are not removed by the trilepton veto, a  
 1684 study was performed on truth-level leptons in  $W^\pm W^\pm jj$  and  $WZ$  MC samples. Events with three  
 1685 truth leptons were selected, and each was matched to its reconstruction-level partner by finding the  
 1686 closest  $\Delta R(\text{truth}, \text{reco})$  and  $\Delta p_T(\text{truth}, \text{reco})$  match. For events surviving the trilepton veto, the  
 1687 two signal leptons were removed, and the remaining leptons represent real leptons that failed to  
 1688 be selected for the veto. Between 40-50% of these leptons fall outside of the eta acceptance of the

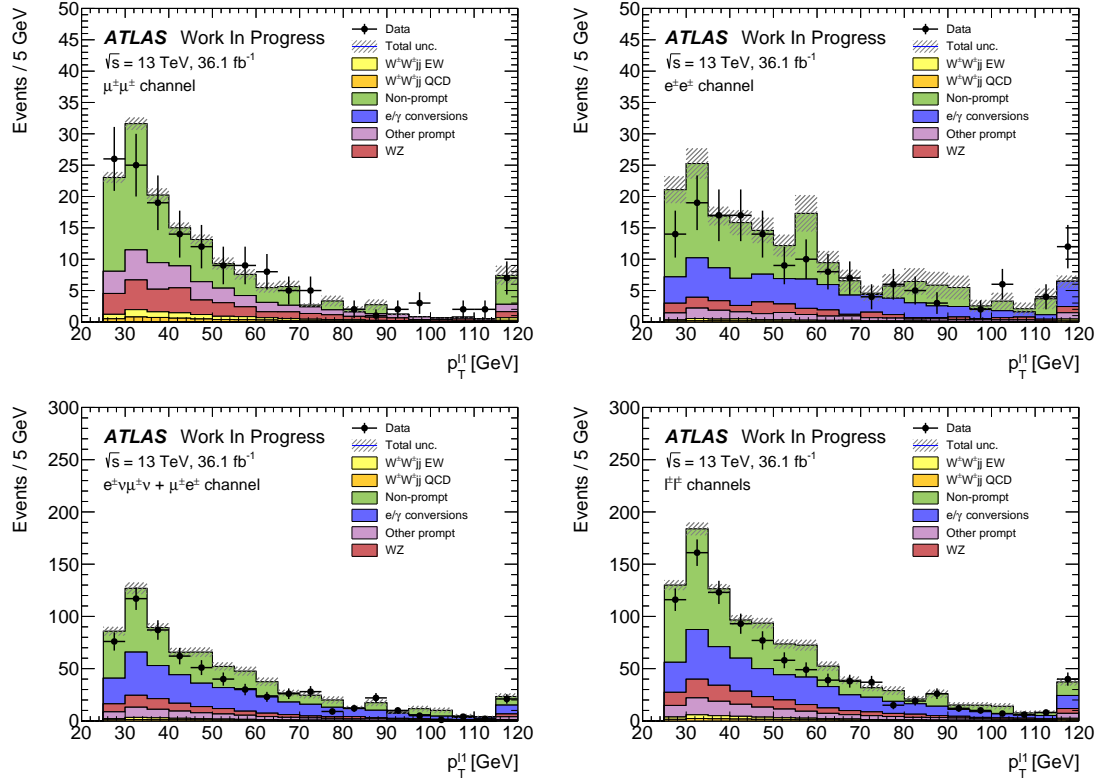


Figure 5.21: Distributions of the subleading lepton  $p_T$  in the same-sign top fakes VR for  $\mu^\pm\mu^\pm$  events (top right),  $e^\pm e^\pm$  events (top left),  $\mu^\pm e^\pm$  events (bottom left), and all events combined (bottom right). All errors are statistical only.

analysis (see Figure 5.22) and are unrecoverable. The second largest source of leptons failing the preselection is the OR, defined in Section 5.2.1.4. The standard OR procedure appears to be too aggressive in removing leptons in favor of jets, causing many three lepton events to “lose” their third lepton and pass the trilepton veto. Therefore a *custom OR* is investigated which would replace the standard OR in the preselection and allow for better  $WZ$  rejection by removing fewer third leptons.

In order to construct this custom OR, a new quantity is defined between a lepton ( $l$ ) and a nearby jet ( $j$ )

$$p_{T,\text{ratio}}(l, j) = \frac{p_{T,l}}{p_{T,j}} \quad (5.13)$$

which, along with  $\Delta R(l, j)$ , will make up the custom OR criteria. The idea behind including  $p_{T,\text{ratio}}$  is to be able to preferentially remove background leptons originating from jets (i.e. those that carry a low percentage of the total jet momentum) instead of removing *any* lepton near a jet. The distributions of  $p_{T,\text{ratio}}$  and the associated efficiency curves for muons and electrons can be found

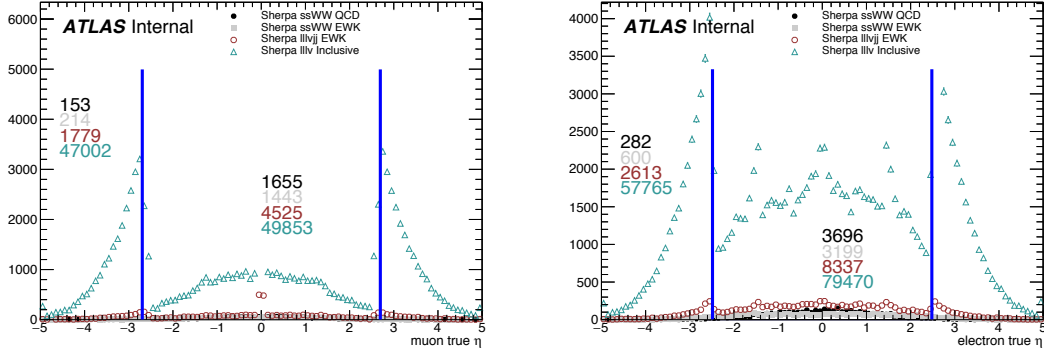


Figure 5.22: Pseudorapidity ( $\eta$ ) distributions of truth muons (top) and electrons (bottom) for Sherpa  $W^\pm W^\pm jj$  and  $WZ$  MC samples. The blue vertical lines represent the allowed  $\eta$  range for each lepton flavor. The numbers correspond to the number of raw MC events that fall within and outside of the allowed  $\eta$  range for each MC sample.

1700 in Figures 5.23 and 5.25, respectively, and the distributions for  $\Delta R(\mu, j)$  for muons can be found in  
 1701 Figure 5.24. Since all electrons have an associated jet in the calorimeters, the  $\Delta R(e, j)$  variable is  
 1702 not a good quantity to use for this custom OR.

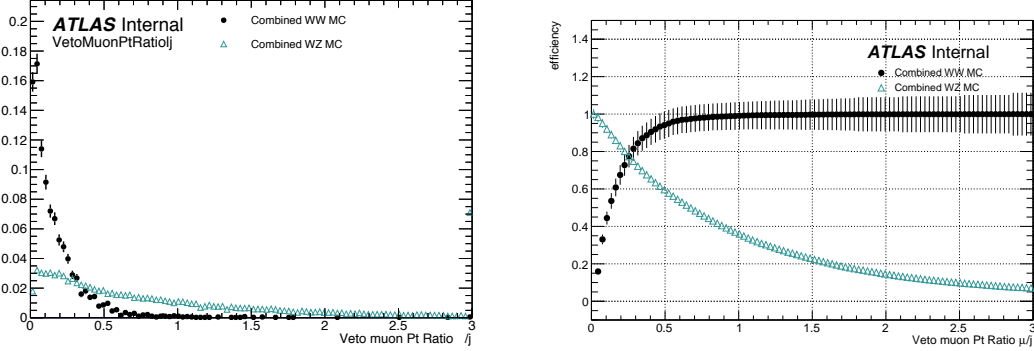


Figure 5.23: Distributions of  $p_{T,\text{ratio}}(\mu, j)$  for EWK and QCD  $W^\pm W^\pm jj$  signal (black) and  $WZ$  background (teal) for truth-matched third muons in events that pass the trilepton veto. Both distributions are normalized to unit area. The associated efficiency curves are on the right where efficiency is defined as the percentage of total events that would pass a cut on  $p_{T,\text{ratio}}(\mu, j)$  at a given value on the  $x$ -axis.

1703 A working point for the Custom OR was chosen by requiring 90% signal retention for muons  
 1704 and 90% background rejection for electrons. The cut on electrons was allowed to be much tighter  
 1705 because the number of signal events with a third electron is considerably smaller than for muons.  
 1706 It should be emphasized that the signal events present in Figures 5.23-5.25 do not represent the full

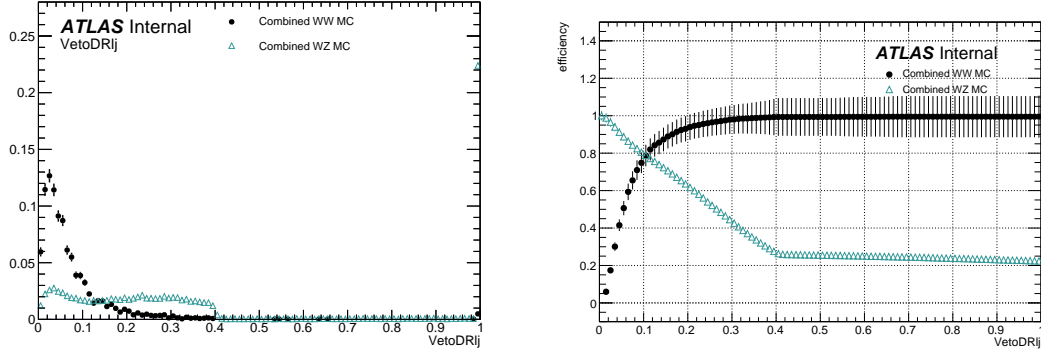


Figure 5.24: Distributions of  $\Delta R(\mu, j)$  for EWK and QCD  $W^\pm W^\pm jj$  signal (black) and  $WZ$  background (teal) for truth-matched third muons in events that pass the trilepton veto. Both distributions are normalized to unit area. The associated efficiency curves are on the right where efficiency is defined as the percentage of total events that would pass a cut on  $\Delta R(\mu, j)$  at a given value on the  $x$ -axis.

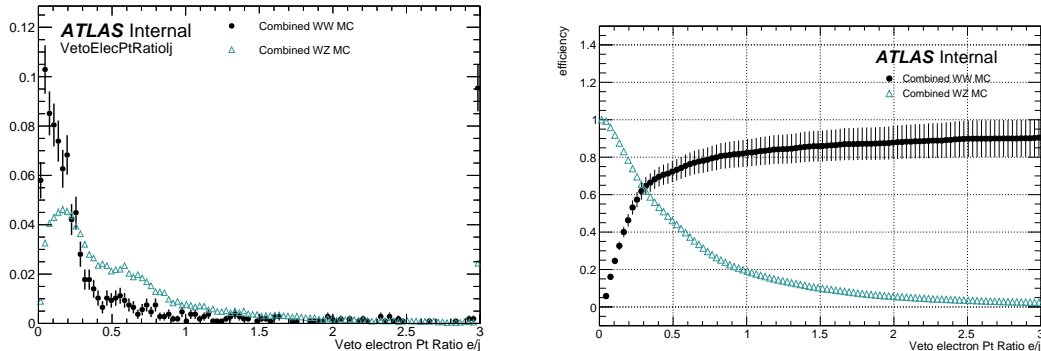


Figure 5.25: Distributions of  $p_{T,\text{ratio}}(e, j)$  for EWK and QCD  $W^\pm W^\pm jj$  signal (black) and  $WZ$  background (teal) for truth-matched third electrons in events that pass the trilepton veto. Both distributions are normalized to unit area. The associated efficiency curves are on the right where efficiency is defined as the percentage of total events that would pass a cut on  $p_{T,\text{ratio}}(e, j)$  at a given value on the  $x$ -axis.

set of signal events, but only those with a real third lepton (which must come from some source other than the signal  $W^\pm W^\pm jj$  process). For muons, a logical ‘or’ of  $p_{T,\text{ratio}}(\mu, j)$  and  $\Delta R(\mu, j)$  is used to maximize the third lepton acceptance due to correlations between the quantities, as shown in Figure 5.26; for electrons, only a cut on  $p_{T,\text{ratio}}(e, j)$  is used. The Custom OR working point is defined in Table 5.17.

Custom OR Definition	
Muons	$p_{T,\text{ratio}}(\mu, j) > 0.40$ or $\Delta R(\mu, j) > 0.15$
Electrons	$p_{T,\text{ratio}}(e, j) > 0.18$

Table 5.17: Custom OR definition. Leptons must pass this selection in order to be counted for the trilepton veto.

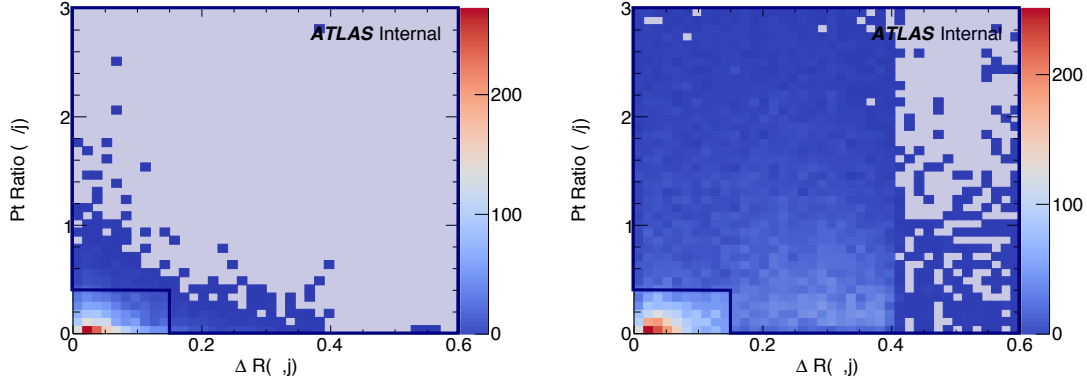


Figure 5.26: Two-dimensional plots of  $p_{T,\text{ratio}}(\mu, j)$  vs  $\Delta R(\mu, j)$  for truth-matched third muons in events that pass the trilepton veto for EWK and QCD  $W^\pm W^\pm jj$  signal (left) and  $WZ$  background (right). The blue overlay indicates the area in which the third leptons will pass the custom OR and result in the event failing the trilepton veto.

Initial tests of the performance of the Custom OR yielded promising results, with approximately 20% reduction in  $WZ$  background compared to less than 2% signal loss in the signal region. Unfortunately, due to differences between the primary analysis framework and the one used for testing, in practice the gains in  $WZ$  rejection were not nearly as substantial, and ultimately the Custom OR was not included in the final analysis. However, it is still a potentially useful tool for improving background rejection based on lepton counting in analyses with overly aggressive OR procedures.

1718 **5.4 Cross section measurement**

1719 The  $W^\pm W^\pm jj$  EWK cross section is extracted from the signal region using a maximum-likelihood  
 1720 fit applied simultaneously to four  $m_{jj}$  bins in the signal region as well as to the low- $m_{jj}$  and  $WZ$   
 1721 control regions. For the fit and cross section extraction, the signal region is defined as in Table 5.8  
 1722 with the dijet invariant mass requirement raised to  $m_{jj} > 500$  GeV. The low- $m_{jj}$  region is defined  
 1723 to mirror the signal region exactly with the dijet invariant mass inverted to  $200 < m_{jj} < 500$  GeV,  
 1724 and the  $WZ$  control region is defined previously in Section 5.3.1.

1725 The signal and low- $m_{jj}$  regions are split into six channels based on the flavor and charge of  
 1726 the dilepton pair:  $\mu^+\mu^+$ ,  $\mu^-\mu^-$ ,  $\mu^+e^+$ ,  $\mu^-e^-$ ,  $e^+e^+$ , and  $e^-e^-$ . This split by charge increases the  
 1727 sensitivity of the measurement due to the  $W^+/W^-$  charge asymmetry at hadron colliders favoring  
 1728 the production of  $W^+$  bosons [81]. Since the signal events contain two  $W$  bosons, the signal strength  
 1729 compared to charge-symmetric backgrounds is much greater in the  $++$  channels for both charges  
 1730 combined. The  $WZ$  control region is included in the fit as a single bin ( $l^\pm l^\mp l^\pm$ ).

1731 The maximum likelihood fit and cross section extractions are outlined in Sections 5.4.1 and  
 1732 5.4.3, respectively. The results of the cross section measurement and of the analysis as a whole are  
 1733 presented in Section 5.6.

1734 **5.4.1 Maximum likelihood fit**

1735 The number of predicted signal events in each channel  $c$  and  $m_{jj}$  bin  $b$  can be calculated from the SM  
 1736 predicted total production cross section  $\sigma_{\text{theo}}^{\text{tot}}$  scaled by the total integrated luminosity  $\mathcal{L}$ , the signal  
 1737 acceptance  $\mathcal{A}$ , and the efficiency corrections  $\mathcal{C}(\theta)$ . Here  $\theta$  represents the set of nuisance parameters  
 1738 that parameterize the effects of each systematic uncertainty on the signal and background expec-  
 1739 tations. The acceptance and efficiency corrections will be covered in more detail in Section 5.4.2.  
 1740

$$N_{cb}^{\text{sig}}(\theta) = \sigma_{\text{theo}}^{\text{tot}} \mathcal{A}_b \mathcal{C}_b(\theta) \mathcal{L} \quad (5.14)$$

1741 A signal strength parameter  $\mu$  is defined as the ratio of the measured cross section to the SM  
 1742 predicted cross section. The expected number of events in a given channel and bin can then be  
 1743 expressed as the sum of the estimated background ( $N_{cb}^{\text{bkg}}(\theta)$ ) and the number of predicted signal  
 1744 events scaled by  $\mu$ :

$$\begin{aligned} N_{cb}^{\text{exp}}(\theta) &= \mu N_{cb}^{\text{sig}}(\theta) + N_{cb}^{\text{bkg}}(\theta) \\ &= \mu \sigma_{\text{theo}}^{\text{tot}} \mathcal{A}_b \mathcal{C}_b(\theta) \mathcal{L} + N_{cb}^{\text{bkg}}(\theta) \end{aligned} \quad (5.15)$$

1745 The nuisance parameters are constrained by Gaussian probability distribution functions, and  
 1746 the normalization of the  $WZ$  background mentioned in Section 5.3.1 is included in the fit as a free  
 1747 parameter. The expected yields for signal and background processes are adjusted by the set of  
 1748 nuisance parameters within the constraints of the systematic uncertainties. The yields after the fit  
 1749 correspond to the value that best matches the observed data.

1750 The number of events per channel and bin after the fit can be written as a sum of the predicted  
 1751 event yields for each sample  $s$ :

$$\nu_{cb}(\phi, \theta, \gamma_{cb}) = \gamma_{cb} \sum_s [\eta_{cs}(\theta) \phi_{cs}(\theta) \lambda] h_{cbs}(\theta) \quad (5.16)$$

1752 In this equation, the fitted number of events in a given channel and bin is obtained by weighting  
 1753 the histogram of predicted yields  $h_{cbs}$  by the product of a given luminosity  $\lambda$  and any normalization  
 1754 factors  $\phi_{cs}$  that may be given for each channel and sample. The input histogram and the normaliza-  
 1755 tion factors may depend on the nuisance parameters  $\theta$  taking into account sources of systematic  
 1756 uncertainty. Uncertainties on the normalization factors  $\eta_{cs}(\theta)$  are also included. Finally, bin-by-bin  
 1757 scale factors  $\gamma_{cb}$  are included to parameterize the statistical uncertainties of the MC predictions.

1758 The binned likelihood function is given by a product of Gaussian functions for the luminosity  
 1759 and for the background uncertainties and a product of Poisson functions for the number of observed  
 1760 events in each bin and channel:

$$L(\mu|\theta) = \mathcal{G}(\mathcal{L}|\theta_{\mathcal{L}}, \sigma_{\mathcal{L}}) \cdot \prod_c \prod_b \mathcal{P}(N_{cb}^{\text{meas.}}|\nu_{cb}(\mu)) \prod_p \mathcal{G}(\theta_p^0|\theta_p) \quad (5.17)$$

1761 where  $\mathcal{G}$  and  $\mathcal{P}$  are the Gaussian and Poisson functions, respectively. As before,  $\mathcal{L}$  represents the  
 1762 integrated luminosity with uncertainty  $\sigma_{\mathcal{L}}$  and associated nuisance parameter  $\theta_{\mathcal{L}}$ . The number of  
 1763 measured events in a given bin and channel is represented by  $N_{cb}^{\text{meas.}}$ , and  $\nu_{cb}(\mu)$  is the predicted  
 1764 number of events defined in Equation 5.16 expressed as a function of the signal strength  $\mu$ . Finally,  
 1765 the set of nuisance parameters  $\theta$  and any auxiliary measurements used to constrain them ( $\theta^0$ ) are  
 1766 multiplied for each parameter  $p$ .

1767 The profile likelihood ratio is defined as

$$q_{\mu} = -2 \ln \frac{L(\mu, \hat{\theta}_{\mu})}{L(\hat{\mu}, \hat{\theta})} \quad (5.18)$$

1768 where  $\hat{\mu}$  and  $\hat{\theta}$  are the unconditional maximum likelihood estimates, and  $\hat{\theta}$  is the conditional maxi-  
 1769 mum likelihood estimate for a given value of  $\mu$ . The fitted signal strength  $\hat{\mu}$  is obtained by maximiz-  
 1770 ing the likelihood function with respect to all parameters. The compatibility of the observed data

1771 with the background-only hypothesis can then be calculated by setting  $\mu = 0$ . Observation of the  
 1772  $W^\pm W^\pm jj$  EWK process is claimed if the data is found to be inconsistent with the background-only  
 1773 hypothesis by more than  $5\sigma$ .

1774 **5.4.2 Definition of the fiducial volume**

1775 Before extracting the cross section, it is necessary to define the fiducial volume, or the phase space  
 1776 of measureable events. It is a subset of the total phase space defined by selection requirements  
 1777 designed to mirror those applied in the analysis as closely as possible. The selection criteria for the  
 1778 fiducial volume are listed in Table 5.18.

Fiducial region selection	
Lepton selection	Two prompt leptons ( $e, \mu$ ) $p_T > 27$ GeV and $ \eta  < 2.5$ for both leptons Both leptons with the same electric charge Dilepton invariant mass $m_{ll} > 20$ GeV Dilepton separation $\Delta R(ll) > 0.3$
Missing transverse energy	Two neutrino system with $p_T^{\nu\nu} > 30$ GeV
Jet selection	At least two jets Leading jet $p_T > 65$ GeV Subleading jet $p_T > 35$ GeV Leading and subleading jet $ \eta  < 4.5$ Jet-lepton separation $\Delta R(l, j) > 0.3$ Dijet invariant mass $m_{jj} > 500$ GeV Dijet separation $\Delta y_{jj} > 2.0$

Table 5.18: Definition of the fiducial volume.

1779 In MC simulations the total phase space is generated, providing the total theoretical cross section  
 1780  $\sigma_{\text{theo}}^{\text{tot}}$  and the total number of signal events  $\mathcal{N}_{\text{sig}}^{\text{tot}}$ <sup>16</sup>. After applying the fiducial selection at truth  
 1781 level, the total number of signal events in the fiducial region  $\mathcal{N}_{\text{sig}}^{\text{fid}}$  is obtained. An acceptance factor  
 1782  $\mathcal{A}$  is used to represent the efficiency of events falling inside the fiducial region at truth level:

$$\mathcal{A} = \frac{\mathcal{N}_{\text{sig}}^{\text{fid}}}{\mathcal{N}_{\text{sig}}^{\text{tot}}} \quad (5.19)$$

1783 A correction factor  $\mathcal{C}$  is also necessary to translate from the truth level fiducial volume to the  
 1784 reconstruction level signal region and is defined in terms of the number of reconstruction level MC  
 1785 events in the signal region  $N_{\text{sig}, \text{MC}}^{\text{SR}}$ :

$$\mathcal{C} = \frac{N_{\text{sig}, \text{MC}}^{\text{SR}}}{\mathcal{N}_{\text{sig}}^{\text{fid}}} \quad (5.20)$$

<sup>16</sup>For the purpose of clarity, the number of events at truth level is represented by a script  $\mathcal{N}$ , and the number of events at reconstruction level uses a regular  $N$ .

1786 Since the fit is binned in  $m_{jj}$ , the acceptance and efficiency correction factors must be as well.  
 1787 Therefore,  $\mathcal{A}_i$  and  $\mathcal{C}_{ij}$  are written in terms of truth  $m_{jj}$  bins  $i$  and reconstruction  $m_{jj}$  bins  $j$ . A  
 1788 graphical representation of these regions and the use of the acceptance and correction factors can  
 1789 be seen in Figure 5.27.

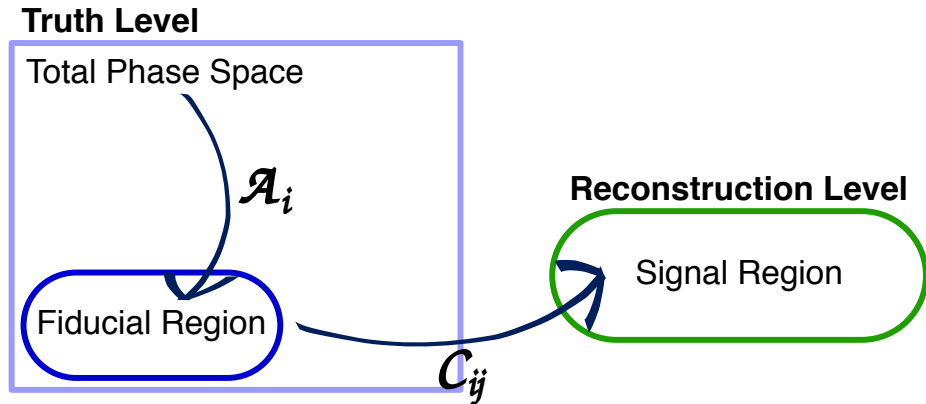


Figure 5.27: Visual representation of the different kinematic regions relevant to the cross section measurement. The acceptance factor  $\mathcal{A}$  converts from the truth level total phase space to the truth level fiducial region, and the efficiency correction  $\mathcal{C}$  translates the fiducial region into the reconstruction level signal region.

#### 1790 5.4.3 Cross section extraction

1791 The  $W^\pm W^\pm jj$  EWK fiducial cross section is measured using the signal strength parameter  $\mu$  that is  
 1792 determined by the maximum likelihood fit. This parameter is dependent on the nuisance parameters  
 1793  $\theta$  and can be written explicitly in terms of the measured and theoretical cross sections as:

$$\mu(\theta) = \frac{\sigma_{\text{meas}}^{\text{SR}}}{\sigma_{\text{theo}}^{\text{SR}}} \quad (5.21)$$

1794 In the simple case with only one bin, the equation for the total number of expected events in the  
 1795 signal region first introduced in Equation 5.15 can be written as:

$$N_{\text{exp}}^{\text{SR}}(\theta) = \mu(\theta) \cdot \sigma_{\text{theo}}^{\text{tot}} \cdot \mathcal{L} \cdot \mathcal{A} \cdot \mathcal{C}(\theta) + N_{\text{bkg}}^{\text{SR}}(\theta) \quad (5.22)$$

1796 with the non-binned versions of  $\mathcal{A}$  and  $\mathcal{C}$  defined in Equations 5.19 and 5.20, respectively.

1797 If the measured fiducial cross section is written as:

$$\sigma_{\text{meas}}^{\text{fid}} = \mu \cdot \mathcal{A} \cdot \sigma_{\text{theo}}^{\text{tot}} \quad (5.23)$$

1798 then Equation 5.22 can be rearranged to read:

$$\sigma_{\text{meas}}^{\text{fid}} = \frac{N_{\text{exp}}^{\text{SR}}(\theta) - N_{\text{bkg}}^{\text{SR}}(\theta)}{\mathcal{L} \cdot \mathcal{C}(\theta)} \quad (5.24)$$

1799 The measured fiducial cross section can finally be rewritten in terms of  $\hat{\mu}$ , which is the best estimator  
1800 of the signal strength as extracted from the fit:

$$\begin{aligned} \sigma_{\text{meas}}^{\text{fid}} &= \hat{\mu}(\theta) \cdot \sigma_{\text{theo}}^{\text{tot}} \cdot \mathcal{A} \\ &= \hat{\mu}(\theta) \cdot \sigma_{\text{theo}}^{\text{fid}} \end{aligned} \quad (5.25)$$

1801 In practice, however, the cross section is not extracted from a single bin, and Equation 5.22  
1802 becomes:

$$N_{\text{exp}}^{\text{SR}}(\theta) = \mu(\theta) \cdot \sigma_{\text{theo}}^{\text{tot}} \cdot \mathcal{L} \cdot \sum_i \mathcal{A}_i \cdot \sum_j \mathcal{C}_{ij} + \sum_j N_{\text{bkg},j}^{\text{SR}}(\theta) \quad (5.26)$$

1803 for a single channel in truth and reconstruction level  $m_{jj}$  bins  $i$  and  $j$ , respectively, where the binned  
1804 versions of  $\mathcal{A}_i$  and  $\mathcal{C}_{ij}$  are used. This equation can be extended to include all the analysis channels  
1805 by increasing the number of bins  $i$  and  $j$ . Additionally, it can be shown that Equation 5.25 holds  
1806 for this more complex case as well [50], provided care is taken to ensure that all the uncertainties  
1807 are handled properly.

## 1808 5.5 Summary of uncertainties

1809 Systematic uncertainties enter the final fit as nuisance parameters which can impact the estimated  
1810 signal and background yields and the shapes of the  $m_{jj}$  distributions. These uncertainties can arise  
1811 from the experimental methods or from the theoretical calculations used in the analysis. This section  
1812 summarizes the systematic uncertainties; the experimental uncertainties are detailed in Section 5.5.1,  
1813 and the theoretical uncertainties are covered in Section 5.5.2. The impacts of the systematic uncer-  
1814 tainties on the final cross section measurement are summarized in Table 5.19.

### 1815 5.5.1 Experimental uncertainties

1816 Experimental uncertainties include detector effects as well as uncertainties on the background es-  
1817 timation methods. Sources of systematic uncertainty on the measurement of physics objects are  
1818 listed in Table 5.20, grouped by the relevant object type. For backgrounds estimated from MC  
1819 simulations, variations in these sources of uncertainty are propagated through the analysis to obtain  
1820 the corresponding uncertainties on the event yields. Additional experimental uncertainties include

Source	Impact [%]
Reconstruction	$\pm 4.0$
Electrons	$\pm 0.5$
Muons	$\pm 1.2$
Jets and $E_T^{\text{miss}}$	$\pm 2.8$
$b$ -tagging	$\pm 2.0$
Pileup	$\pm 1.5$
Background	$\pm 5.0$
Misid. leptons	$\pm 3.9$
Charge misrec.	$\pm 0.3$
$WZ$	$\pm 1.3$
$W^\pm W^\pm jj$ QCD	$\pm 2.8$
Other	$\pm 0.8$
Signal	$\pm 3.6$
Interference	$\pm 1.0$
EW Corrections	$\pm 1.3$
Shower, Scale, PDF & $\alpha_s$	$\pm 3.2$
Total	$\pm 7.4$

Table 5.19: Impact of various systematic effects on the fiducial cross section measurement. The impact of a given source of uncertainty is computed by performing the fit with the corresponding nuisance parameter varied up or down by one standard deviation from its nominal value.

1821 the integrated luminosity, the photon conversion rate from Section 5.3.2, and the data driven charge  
 1822 misidentification and fake lepton background estimations from Sections 5.3.3 and 5.3.4.5, respec-  
 1823 tively.

1824 The largest sources of experimental uncertainty on the MC estimations come from the jet-related  
 1825 uncertainties and the  $b$ -tagging efficiency, while the largest uncertainty on the background estimation  
 1826 comes from the fake-factor. The effects of the uncertainties on the  $W^\pm W^\pm jj$  EWK signal and the  
 1827 dominant MC estimated background,  $WZ$ , are listed in Tables 5.21 and 5.22, respectively. Since  
 1828 the overall contributions from other processes estimated with MC are small, the uncertainties on  
 1829 these backgrounds have a lesser impact on the final measurement; these tables can be found in  
 1830 Appendix A.1.

### 1831 5.5.2 Theoretical uncertainties

1832 It is also necessary to consider uncertainties on the theoretical predictions in the fiducial region. They  
 1833 include the choice of PDF set, the value of the strong coupling constant  $\alpha_s$ , the renormalization  
 1834 scale  $\mu_R$ , the factorization scale  $\mu_F$ , and the parton showering. The size of these uncertainties  
 1835 are measured by generating new samples with variations in a chosen parameters and comparing

Experimental uncertainties	
Electrons	Energy resolution
	Energy scale
	Identification efficiency
	Isolation efficiency
	Reconstruction efficiency
	Trigger efficiency
Muons	Energy scale
	Identification efficiency
	Inner detector track resolution
	Muon spectrometer resolution
	Trigger efficiency
$E_T^{\text{miss}}$	Resolution
	Scale
Jets	Energy resolution
	Energy scale
	JVT cut efficiency
	$b$ -tagging efficiency
	Jets from pileup

Table 5.20: List of sources of experimental uncertainties on the reconstruction of physics objects.

$W^\pm W^\pm jj$ EWK	$e^\pm e^\pm$ % Yield	$\mu^\pm e^\pm$ % Yield	$\mu^\pm \mu^\pm$ % Yield
Jet-related Uncertainties	2.28	2.22	2.28
$b$ -tagging efficiency	1.81	1.76	1.74
Pile-up	0.48	0.97	2.42
Trigger efficiency	0.02	0.08	0.47
Lepton reconstruction/ID	1.45	1.14	1.83
MET reconstruction	0.26	0.17	0.21

Table 5.21: Impact of experimental uncertainties for the  $W^\pm W^\pm jj$  EWK processes in all channels.

$WZ$	$e^\pm e^\pm$ % Yield	$\mu^\pm e^\pm$ % Yield	$\mu^\pm \mu^\pm$ % Yield
Jet-related Uncertainties	9.58	5.03	8.45
$b$ -tagging efficiency	2.49	2.23	2.40
Pile-up	2.99	3.49	3.33
Trigger efficiency	0.03	0.09	0.43
Lepton reconstruction/ID	1.52	1.24	3.07
MET reconstruction	0.93	0.79	1.63

Table 5.22: Impact of experimental uncertainties for the  $WZ$  process in all channels.

them to samples using the nominal choice of the parameter. Internal variations on the PDF sets and using a different set entirely results in a relative uncertainty of up to 2.25% on the nominal sample. The impact from varying  $\alpha_s$  is very small, on the order of < 0.01%. The factorization and renormalization scales are independently varied between 0.5-2.0 from their nominal values of 1.0. This results in relative uncertainties on the prediction of up to 15%. Finally, varying the parameters in the parton showering results in up to 8% uncertainty.

#### 5.5.2.1 Uncertainties from EWK-QCD interference

As mentioned in Section 5.0.1,  $W^\pm W^\pm jj$  production consists of both EWK processes. The two production modes cannot be naively separated due to cross terms in the matrix element calculation. These cross terms are referred to as *interference* terms. Since the  $W^\pm W^\pm jj$  EWK production is the focus of the analysis, and the signal region is designed to preferentially select those events, it is important to measure the size of the EWK-QCD interference contributions.

The interference effects are estimated using the `MadGraph` MC generator, as it has a feature that allows direct modelling of the interference term. This allows four samples to be generated:

1. Inclusive: All available diagrams are used in the matrix element calculation
2. EWK only: Only EWK diagrams ( $\mathcal{O}(\alpha_{\text{EWK}}) = 4$ ) are used
3. QCD only: Only QCD diagrams ( $\mathcal{O}(\alpha_s) = 2 \otimes \mathcal{O}(\alpha_{\text{EWK}}) = 2$ ) are used
4. Interference: Only the interference terms are used

A minimal set of generator level cuts, listed in Table 5.23, is applied in order to avoid biasing the sample towards either production mode. The cross sections for each of the four channels can be found in Table 5.24. The size of the interference is found to be approximately 6% of the total cross section and is taken as a systematic uncertainty.

Generator level cuts
$\Delta\eta_{jj} < 10$
Jet $p_T > 20$ GeV
$M_{jj} > 10$ GeV

Table 5.23: The set of generator level cuts used for generating the interference samples with `MadGraph`.

Sample	$\sigma$ (fb)
Inclusive	$3.646 \pm 0.0012$
EWK only	$2.132 \pm 0.0005$
QCD only	$1.371 \pm 0.0008$
Interference	$0.227 \pm 0.0002$

Table 5.24: Cross sections for each different  $W^\pm W^\pm jj$  production mode (inclusive, EWK only, QCD only, and interference only) generated using `MadGraph`. The cross sections are calculated using a minimal set of generator level cuts from events where the  $W$  decays to a muon.

## 1858 5.6 Results

1859 After running the full analysis chain, the event yields in the signal region, low- $m_{jj}$  control region,  
 1860 and  $WZ$  control region as well as associated nuisance parameters representing the uncertainties are  
 1861 passed to the maximum likelihood fit. From this fit, the normalization factor for the  $WZ$  control  
 1862 region  $\mu_{WZ}$  and the signal strength parameter in the signal region  $\mu_{\text{obs}}$  are determined, and the  
 1863 predicted yields in each input bin have been shifted according to the process detailed in Section 5.4.1.

1864 The  $WZ$  normalization factor is measured to be:

$$\mu_{WZ} = 0.88^{+0.07}_{-0.07}(\text{stat})^{+0.31}_{-0.21}(\text{theory})^{+0.22}_{-0.11}(\text{sys}) \quad (5.27)$$

1865 and is constrained primarily by the number of data events in the  $WZ$  control region. The observed  
 1866 signal strength of  $W^\pm W^\pm jj$  EWK production, defined in Equation 5.21, is extracted from the fit  
 1867 and measured with respect to the prediction of the `SHERPA v2.2.2` MC generator:

$$\mu_{\text{obs}} = 1.45^{+0.25}_{-0.24}(\text{stat})^{+0.06}_{-0.08}(\text{theory})^{+0.27}_{-0.22}(\text{sys}) \quad (5.28)$$

1868 This corresponds to a rejection of the background-only hypothesis with a significance of  $6.9\sigma$ .

1869 The observed number of data events are compared to the predicted signal and background yields  
 1870 in the signal region in Table 5.25 before applying the fit and in Table 5.26 after the fit. 122 candidate  
 1871 events are observed compared to a prediction of 60 signal and 69 background events.

1872 The  $m_{jj}$  distributions for data and prediction are shown in Figure 5.28 after the fit, and the  
 1873 fitted event yields in the low- $m_{jj}$  and  $WZ$  control regions are shown in Figure 5.29. Additional  
 1874 distributions can be found in Appendix A.

1875 The last ingredient necessary to measure the  $W^\pm W^\pm jj$  EWK cross section is the theory predicted  
 1876 cross section in the fiducial region defined in Table 5.18. `SHERPA v2.2.2` is used for the calculation,  
 1877 and the cross section in the total generator phase space is  $40.81 \pm 0.05$  fb, and the fiducial cross section  
 1878 is  $2.01 \pm 0.02$  fb. This corresponds to an acceptance factor of  $\mathcal{A} = 0.0493 \pm 0.0002$ . Uncertainties on

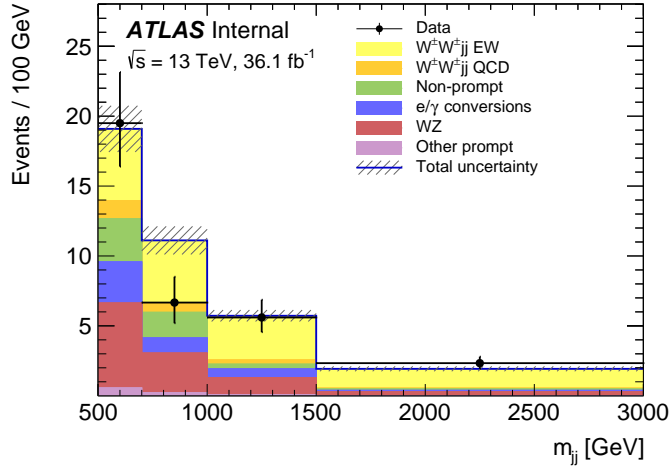


Figure 5.28: The dijet invariant mass  $m_{jj}$  distributions for data and predicted signal and background in the signal region after the fit. The shaded band represents the statistical and systematic uncertainties added in quadrature. Note that the bins have been scaled such that they represent the number of events per 100 GeV in  $m_{jj}$ . The background estimations from the fake-factor are included in the “Non-prompt” category, and backgrounds from  $V\gamma$  production and electron charge misidentification are combined in the “ $e/\gamma$  conversions” category. Finally,  $ZZ$ ,  $VVV$ , and  $t\bar{t} + V$  backgrounds are combined in the “Other prompt” category.

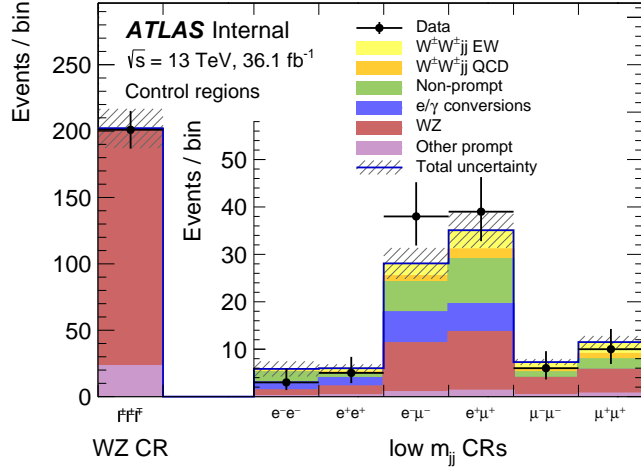


Figure 5.29: The event yields for data and predicted signal and background in the  $WZ$  and low- $m_{jj}$  control regions after the fit. The shaded band represents the statistical and systematic uncertainties added in quadrature. The background estimations from the fake-factor are included in the “Non-prompt” category, and backgrounds from  $V\gamma$  production and electron charge misidentification are combined in the “ $e/\gamma$  conversions” category. Finally,  $ZZ$ ,  $VVV$ , and  $t\bar{t}V$  backgrounds are combined in the “Other prompt” category.

	$e^+e^+$	$e^-e^-$	$\mu^+e^+$	$\mu^-e^-$	$\mu^+\mu^+$	$\mu^-\mu^-$	combined
$WZ$	$1.9 \pm 0.6$	$1.3 \pm 0.4$	$14 \pm 4$	$8.9 \pm 2.6$	$5.5 \pm 1.6$	$3.6 \pm 1.1$	$35 \pm 10$
Non-prompt	$4.1 \pm 2.3$	$2.3 \pm 1.7$	$9 \pm 5$	$6 \pm 4$	$0.57 \pm 0.15$	$0.67 \pm 0.25$	$23 \pm 10$
$e/\gamma$ conversions	$1.74 \pm 0.29$	$1.8 \pm 0.4$	$6.1 \pm 1.6$	$3.7 \pm 0.8$	—	—	$13.4 \pm 2.5$
Other prompt	$0.17 \pm 0.05$	$0.14 \pm 0.04$	$0.90 \pm 0.19$	$0.60 \pm 0.14$	$0.36 \pm 0.10$	$0.19 \pm 0.05$	$2.4 \pm 0.5$
$W^\pm W^\pm jj$ QCD	$0.38 \pm 0.13$	$0.16 \pm 0.05$	$3.0 \pm 1.0$	$1.2 \pm 0.4$	$1.8 \pm 0.6$	$0.76 \pm 0.25$	$7.3 \pm 2.5$
Expected background	$8.2 \pm 2.4$	$5.7 \pm 1.8$	$33 \pm 7$	$21 \pm 5$	$8.2 \pm 1.8$	$5.3 \pm 1.2$	$81 \pm 14$
$W^\pm W^\pm jj$ EWK	$3.8 \pm 0.6$	$1.49 \pm 0.22$	$16.5 \pm 2.5$	$6.5 \pm 1.0$	$9.1 \pm 1.4$	$3.5 \pm 0.5$	$41 \pm 6$
Data	10	4	44	28	25	11	122

Table 5.25: Table of the data and prediction event yields in the signal region before the fit. Numbers are shown for the six lepton flavor and charge channels and for all channels combined. Here the  $WZ$  background yields are normalized to the data in the  $WZ$  control region. The background estimations from the fake-factor are included in the “Non-prompt” category, and backgrounds from  $V\gamma$  production and electron charge misidentification are combined in the “ $e/\gamma$  conversions” category. Finally,  $ZZ$ ,  $VVV$ , and  $t\bar{t} + V$  backgrounds are combined in the “Other prompt” category.

	$e^+e^+$	$e^-e^-$	$\mu^+e^+$	$\mu^-e^-$	$\mu^+\mu^+$	$\mu^-\mu^-$	combined
$WZ$	$1.49 \pm 0.30$	$1.10 \pm 0.26$	$11.7 \pm 1.7$	$8.0 \pm 1.3$	$5.0 \pm 0.6$	$3.5 \pm 0.6$	$31 \pm 4$
Non-prompt	$2.2 \pm 1.3$	$1.2 \pm 0.7$	$5.7 \pm 2.8$	$4.5 \pm 1.8$	$0.57 \pm 0.06$	$0.65 \pm 0.14$	$15 \pm 6$
$e/\gamma$ conversions	$1.6 \pm 0.4$	$1.6 \pm 0.5$	$6.3 \pm 1.6$	$4.3 \pm 1.1$	—	—	$13.8 \pm 2.9$
Other prompt	$0.16 \pm 0.04$	$0.14 \pm 0.04$	$0.90 \pm 0.19$	$0.63 \pm 0.13$	$0.39 \pm 0.09$	$0.22 \pm 0.05$	$2.4 \pm 0.5$
$W^\pm W^\pm jj$ QCD	$0.35 \pm 0.13$	$0.15 \pm 0.05$	$2.9 \pm 1.0$	$1.2 \pm 0.4$	$1.8 \pm 0.6$	$0.76 \pm 0.25$	$7.2 \pm 2.4$
Expected background	$5.8 \pm 1.5$	$4.1 \pm 1.1$	$27 \pm 4$	$18.7 \pm 2.6$	$7.7 \pm 0.8$	$5.1 \pm 0.6$	$69 \pm 7$
$W^\pm W^\pm jj$ EWK	$5.6 \pm 1.0$	$2.2 \pm 0.4$	$24 \pm 5$	$9.4 \pm 1.8$	$13.5 \pm 2.5$	$5.2 \pm 1.0$	$60 \pm 11$
Data	10	4	44	28	25	11	122

Table 5.26: Table of the data and prediction event yields in the signal region after the fit. Numbers are shown for the six lepton flavor and charge channels and for all channels combined. The background estimations from the fake-factor are included in the “Non-prompt” category, and backgrounds from  $V\gamma$  production and electron charge misidentification are combined in the “ $e/\gamma$  conversions” category. Finally,  $ZZ$ ,  $VVV$ , and  $t\bar{t}V$  backgrounds are combined in the “Other prompt” category.

1879 the simulation are estimated using variations of the scale, parton shower, and PDF set. The final  
 1880 prediction used in the cross section measurement including uncertainties from Section 5.5.2 is:

$$\sigma_{\text{SHERPA}}^{\text{fid}} = 2.01 \pm 0.02(\text{stat}) \begin{array}{l} +0.29 \\ -0.23 \end{array} (\text{scale}) \begin{array}{l} +0.16 \\ -0.02 \end{array} (\text{parton shower}) \begin{array}{l} +0.05 \\ -0.03 \end{array} (\text{PDF}) \text{ fb} \quad (5.29)$$

1881 Combining this **SHERPA** prediction with the measured signal strength  $\mu_{\text{obs}}$  from Equation 5.28,  
 1882 the measured fiducial cross section  $\sigma_{\text{meas}}^{\text{fid}}$  can be calculated using Equation 5.25:

$$\sigma_{\text{meas}}^{\text{fid}} = 2.91 \begin{array}{l} +0.51 \\ -0.47 \end{array} (\text{stat}) \begin{array}{l} +0.12 \\ -0.16 \end{array} (\text{theory}) \begin{array}{l} +0.24 \\ -0.23 \end{array} (\text{sys}) \begin{array}{l} +0.08 \\ -0.06 \end{array} (\text{luminosity}) \text{ fb} \quad (5.30)$$

1883 A plot comparing the measured fiducial cross section to two theoretical calculations is shown in  
 1884 Figure 5.30. The measured value is compared to the **SHERPA v2.2.2** prediction used to calculate  
 1885  $\mu_{\text{obs}}$  as well as to **POWHEG-BOX v2**. As mentioned in Section 5.1.1, this **POWHEG** sample does not  
 1886 include the resonant triboson diagrams and is only used here for a visual comparison.

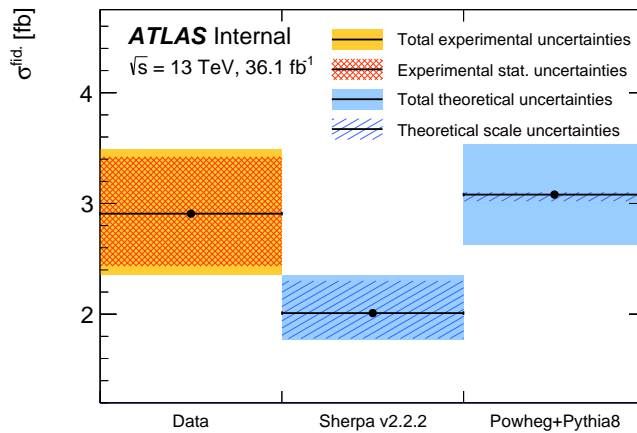


Figure 5.30: Comparison of the measured  $W^\pm W^\pm jj$  EWK fiducial cross section with theoretical calculations from **SHERPA v2.2.2** and **POWHEG-BOX v2**. The light orange band represents the total experimental uncertainty on the measured value, and the dark orange hashed band is the statistical uncertainty. For the simulations, the light blue band represents the total theoretical uncertainty, and the dark blue hashed band are the scale uncertainties. The theory predictions do not include the interference between the EWK and QCD production.

## CHAPTER 6

---

# Prospects for same-sign $WW$ at the High Luminosity LHC

---

1890 On December 3, 2018, Run 2 of the LHC officially ended, and the collider was shut down to begin  
 1891 the first of two scheduled extended maintenance periods [82]. During these two long shutdowns,  
 1892 the Phase-I and Phase-II upgrades of the LHC and ATLAS will occur in order to prepare for the  
 1893 High-Luminosity LHC (HL-LHC) which is scheduled to begin operation in 2026 [83].

1894 The HL-LHC is planned to run at a center-of-mass energy of  $\sqrt{s} = 14$  TeV with an instantaneous  
 1895 luminosity of  $\mathcal{L} = 5 \times 10^{34}$  cm $^{-2}$ s $^{-1}$  with up to 200 collisions per beam-crossing. Over the course  
 1896 of operation, the HL-LHC is expected to collect a total integrated luminosity of  $\mathcal{L} = 3000$  fb $^{-1}$  by  
 1897 2035 [84].

1898 These run conditions will be much harsher than what ATLAS has experienced so far, and there  
 1899 are several upgrades planned to adapt the detector to the high luminosity environment. Most  
 1900 notably, the entire ID will be replaced with an all-silicon tracker which will extend the coverage  
 1901 from  $|\eta| \leq 2.7$  up to  $|\eta| \leq 4.0$ . This will allow for forward particle tracks to be reconstructed, which  
 1902 can in turn be matched to clusters in the calorimeters for use in electron identification or forward  
 1903 jet tagging [85].

1904 The upgraded detector, the higher beam energy, and the increased volume of data to be col-  
 1905 lected provides the opportunity to measure rare processes to a much higher precision than what  
 1906 is possible with the current LCH dataset. Same-sign  $W^\pm W^\pm jj$  production is one such process.  
 1907 With greater statistics, the accuracy of the cross section measurement can be improved over the  
 1908 13 TeV analysis detailed in Chapter 5, and it also will allow for more detailed physics studies, such  
 1909 as measuring the polarization state of the scattered  $W$  bosons. A measurement of the cross section

of longitudinally polarized  $W^\pm W^\pm jj$  scattering is one of the most enticing extensions of the existing  $W^\pm W^\pm jj$  measurements due to its sensitivity to the EWSB mechanism [86], and it is expected to be measurable for the first time at the HL-LHC. The analysis detailed in this chapter is based off of the 2018 ATLAS HL-LHC  $W^\pm W^\pm jj$  prospects study [87] which extends upon the results of the previous year’s study [88].

### 6.0.1 Analysis Overview

The experimental signature of interest is identical to the 13 TeV analysis (see Chapter 5): two prompt leptons (either electrons or muons) with the same electric charge, missing transverse energy, and two high energy forward jets. These jets are again required to have a large angular separation and a high combined invariant mass to preferentially select EWK-produced  $W^\pm W^\pm jj$  events.

Background processes are not expected to change with respect to the 13 TeV analysis and are summarized here. The dominant source of prompt background comes from  $WZ+jets$  events where both bosons decay leptonically. If the lepton from the  $Z$ -decay with opposite charge from the  $W$  falls outside of the detector acceptance or is not identified, the remaining two leptons will form a same-sign pair, and the event may pass the signal lepton criteria. To a much lesser extent,  $ZZ+jets$  events can enter the signal region this way provided two leptons are “lost”. Other prompt sources include  $t\bar{t}+V$  and multiple parton interactions, however both contributions are small. Overall, prompt backgrounds are expected to contribute less than in current analyses due to the addition of forward tracking in the upgraded ATLAS detector reducing the probability of leptons falling outside the detector acceptance. Jets mis-reconstructed as leptons or leptons from hadronic decays (such as  $t\bar{t}$  and  $W+jets$  production) comprise the non-prompt lepton background. Lastly, events with two prompt, opposite-charge electrons can appear as a same-sign event provided one of the electrons is mis-reconstructed and assigned the wrong charge.

In this analysis, the EWK production of  $W^\pm W^\pm jj$  is studied in the context of the planned HL-LHC run conditions and upgraded ATLAS detector. An optimized event selection (referred to as the *optimized selection*) is also explored in an effort to gain increased signal significance over the *default selection*. The cross section of the inclusive EWK production is measured for both the default and optimized selections, and the extraction of the expected longitudinal scattering significance is measured with the optimized selection.

1939 **6.1 Theoretical motivation**

1940 The motivation for studying the  $W^\pm W^\pm jj$  process as well as VBS in general has been established  
 1941 previously in Sections 2.3 and 5.0.1. Since only the longitudinally polarized vector bosons that is  
 1942 sensitive to the EWSB mechanism, a direct measurement of this cross section will be very useful for  
 1943 understanding how the Higgs unitarizes the scattering amplitude [86].

1944 **6.1.1 Experimental sensitivity to longitudinal polarization**

1945 There are three possible polarization states for a massive vector boson: two transverse (+ or -)  
 1946 and one longitudinal (0). Therefore, in a system with two  $W$  bosons, the overall polarization can be  
 1947 purely longitudinal (00), purely transverse (++, --, and +-), or mixed (+0 and -0). The three  
 1948 combinations will be referred to as *LL*, *TT*, and *LT* respectively.

1949 In order extract the longitudinal scattering component, it is necessary to find variables that can  
 1950 help distinguish the LL from the TT and LT events. Several were studied, and those with the best  
 1951 discriminating power between the different polarization states are the leading and subleading lepton  
 1952 transverse momenta as well as the azimuthal separation of the two VBS jets  $|\Delta\phi_{jj}|$ . Both leptons  
 1953 in LL events tend to be softer than the TT and LT events (see Figure 6.1), which motivates keeping  
 1954 cuts on the lepton  $p_T$  as low as possible in the event selection. In the case of the dijet separation, LL  
 1955 events prefer the tag jets to be back-to-back (see Figure 6.2).  $|\Delta\phi_{jj}|$  is passed to a binned likelihood  
 1956 fit to extract the longitudinal scattering significance.

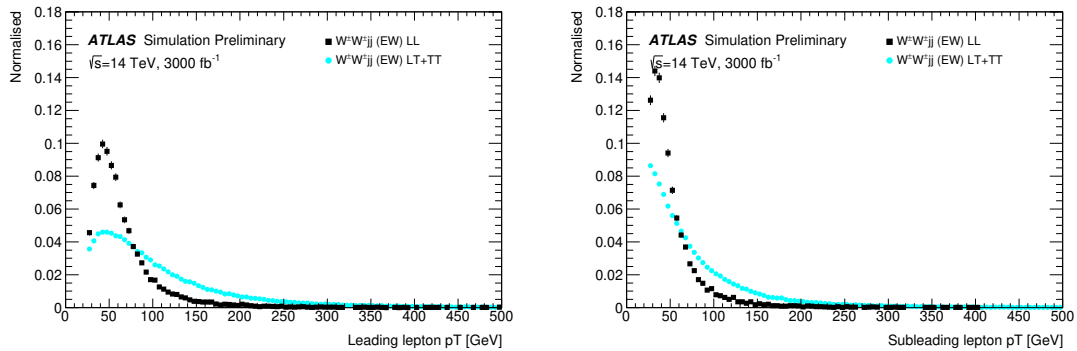


Figure 6.1: Comparison of the leading (left) and subleading (right) lepton  $p_T$  distributions for purely longitudinal (LL, black) and mixed polarization (LT+TT, cyan)  $W^\pm W^\pm jj$  events.

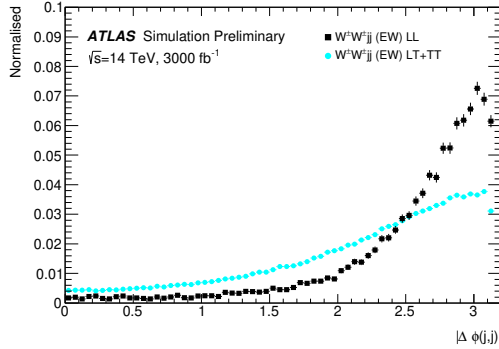


Figure 6.2: Comparison of the azimuthal dijet separation ( $|\Delta\phi_{jj}|$ ) for purely longitudinal (LL, black) and mixed polarization (LT+TT, cyan)  $W^\pm W^\pm jj$  events.

## 1957 6.2 Monte Carlo samples

1958 As this is a prospects study for a future collider, all signal and background processes are modeled  
 1959 using MC simulations. The samples are generated at the expected HL-LHC center of mass energy  
 1960  $\sqrt{s} = 14$  TeV, and the event yields are scaled to the anticipated integrated luminosity of  $\mathcal{L} =$   
 1961  $3000 \text{ fb}^{-1}$ . The MC samples used in the analysis are generated at particle-level and have not been  
 1962 run through the full simulation of the ATLAS detector. Instead, smearing functions derived from  
 1963 a GEANT4 simulation of the upgraded ATLAS detector are used to estimate detector effects such as  
 1964 momentum resolution. In addition, pileup events are fully simulated. The MC samples used in this  
 1965 analysis are summarized in Table 6.1.

1966 The signal sample consists of both VBS and non-VBS electroweak (EWK)  $W^\pm W^\pm jj$  production,  
 1967 and it is simulated with the `Madgraph5_aMC@NLO` generator using the NNPDF3.0 PDF set and in-  
 1968 terfaced with PYTHIA v8 [89] for hadronization and parton showering. To study the longitudinal  
 1969 polarization more directly, two additional `Madgraph5_aMC@NLO`  $W^\pm W^\pm jj$  samples are used: one  
 1970 containing only the longitudinal contribution (LL) and a second containing the transverse (TT) and  
 1971 mixed (LT) contributions.

1972 There are many other processes that can produce the same final state as the  $W^\pm W^\pm jj$  and must  
 1973 also be accounted for using MC simulations.  $WZ$  events are generated using `SHERPA v2.2.0`, which  
 1974 includes up to one parton at NLO in the strong coupling constant and up to three additional partons  
 1975 at LO. Both EWK and QCD production are included in these samples.  $ZZ$  and triboson  $VVV$   
 1976 ( $V = W, Z$ ) events are generated using `SHERPA v2.2.2` with up to two additional partons in the  
 1977 final state. For the triboson backgrounds, the bosons can decay leptonically or hadronically.  $W+jets$

Process	Generator	Comments
$W^\pm W^\pm jj$ (EWK)	Madgraph5_aMC@NLO	Signal sample
$W^\pm W^\pm jj$ (QCD)	Madgraph5_aMC@NLO	
$W^\pm W^\pm jj$ (LL)	Madgraph5_aMC@NLO	Pure longitudinal polarization sample
$W^\pm W^\pm jj$ (TT+LT)	Madgraph5_aMC@NLO	Mixed and transverse polarization sample
Diboson	SHERPA v2.2.0	$WZ$ events
	SHERPA v2.2.2	$ZZ$ events
Triboson	SHERPA v2.2.2	
$W+jets$	Madgraph5_aMC@NLO	
$Z+jets$	POWHEG-BOX v2	
$t\bar{t}$	POWHEG-BOX	
Single top	POWHEG-BOS	

Table 6.1: Summary of MC samples used in the analysis.

1978 backgrounds are generated for electron, muon, and tau final states at LO with `Madgraph5_aMC@NLO`  
 1979 and the `NNPDF3.0` PDF set with showering from `PYTHIA v8`.  $Z+jets$  events are produced using  
 1980 `POWHEG-BOX v2` and the `CT10` PDF set interfaced with `PYTHIA v8`. Finally,  $t\bar{t}$  and single-top events  
 1981 are generated using `POWHEG-BOX` with showering from `PYTHIA v6`.

### 1982 6.3 Background estimations

1983 In this analysis, all background contributions are estimated using MC simulations. Backgrounds  
 1984 from electron charge misidentification and fake electrons from jets, which are traditionally estimated  
 1985 using data-driven techniques, are instead estimated using a set of parameterization functions applied  
 1986 to the MC. These functions calculate the probability that an electron is assigned the wrong charge or  
 1987 a jet is mis-reconstructed as an electron parameterized by the  $p_T$  and  $\eta$  of the respective electron or  
 1988 jet. The probabilities are derived from studies on expected electron performance with the upgraded  
 1989 ATLAS detector [90].

1990 Processes involving two  $W$  or  $Z$  bosons are grouped together as *diboson* backgrounds, with the  
 1991 exception of  $W^\pm W^\pm jj$  events produced via QCD interactions, which are kept separate. Similarly,  
 1992 all backgrounds with three vector bosons are combined and labeled as *triboson*. Any  $W+jets$  or top  
 1993 events that pass selection and do not contain a fake electron, as well as any  $Z+jets$  events without an  
 1994 electron identified as having its charge misidentified are combined as *other non-prompt* backgrounds.

---

1995 **6.3.1 Truth-based isolation**

1996 The canonical isolation variables used in ATLAS analyses require detailed information from many  
1997 detector subsystems including particle tracks and calorimeter responses. Since the MC samples used  
1998 in this analysis have not been run through a full detector simulation, it is not possible to reproduce  
1999 the official isolation variables. For truth-level analysis, this is generally not a serious concern, as  
2000 high- $p_T$  signal leptons tend to be well isolated to begin with. However, isolation is one of the  
2001 most powerful tools for rejecting leptons from non-prompt sources, such as top events, which are  
2002 produced in association with additional nearby particles from  $b$  and  $c$  hadron decays. It was seen in  
2003 the early stages of this analysis that without any sort of isolation requirement, contributions from  
2004 top backgrounds (including single top,  $t\bar{t}$  and  $t\bar{t} + V$ ) were more than an order of magnitude higher  
2005 than expected.

2006 As a result, it is necessary to find one or more quantities that are comparable to the isolation  
2007 information that is available in fully-simulated samples. Analogues to track- and calorimeter-based  
2008 isolation are constructed by summing the momentum and energy, respectively, of stable truth parti-  
2009 cles with  $p_T > 1$  GeV within a specified radius of each signal lepton. For the track-based isolation,  
2010 only charged truth particles are used; both charged and neutral particles (excluding neutrinos) are  
2011 included for the calorimeter-based isolation. Ultimately, a set of isolation cuts are chosen that are  
2012 similar to those recommended by ATLAS for Run 2 analyses. The truth-based isolation requirements  
2013 are listed in Table 6.2.

	Electron Isolation	Muon Isolation
Track-based isolation cone size	$\Delta R < 0.2$	$\Delta R < 0.3$
Track-based isolation requirement	$\sum p_T/p_T^e < 0.06$	$\sum p_T/p_T^\mu < 0.04$
Calorimeter-based isolation cone size	$\Delta R < 0.2$	$\Delta R < 0.2$
Calorimeter-based isolation requirement	$\sum E_T/p_T^e < 0.06$	$\sum E_T/p_T^\mu < 0.15$

Table 6.2: Truth-based isolation requirements for electrons and muons.

2014 With no cut on truth-based isolation, 83% of the total background consists of top events without  
2015 including contributions to the fake electron background. The isolation requirement reduces the top  
2016 background by over 99%, and the percentage of the total background from top events is reduced to  
2017 2%. Additional studies on the truth-based isolation as well as full event yields with and without the  
2018 isolation requirement can be found in Appendix B.1.

---

2019 **6.4 Object and event selection**

2020 The majority of the default object and event selections were determined in the preceeding  $W^\pm W^\pm jj$   
 2021 HL-LHC prospects study [88], which focused on the impact of the upgraded detector's forward  
 2022 tracking capabilities. Several different combinations of lepton and jet  $\eta$  ranges were tested, and the  
 2023 results are used in this study.

2024 **6.4.1 Object selection**

2025 Electrons and muons are preselected to have  $p_T > 7$  and  $6$  GeV, respectively, and lie within  $|\eta| \leq 4.0$ .  
 2026 The likelihood of a given lepton to pass the trigger and identification requirements is estimated by  
 2027 calculating an efficiency dependent on the  $p_T$  and  $\eta$  of the lepton. The leptons are also required to  
 2028 pass the isolation criteria detailed in Table 6.2. Jets that have been tagged as a fake electron by the  
 2029 functions described in Section 6.3 are treated as electrons for the purpose of the object selection and  
 2030 are subject to the same criteria. In order to be considered a signal lepton, the transverse momentum  
 2031 requirement is raised to  $p_T > 25$  GeV. The two highest  $p_T$  leptons passing this selection are chosen  
 2032 to be the leading and subleading signal leptons.

2033 Jets are clustered using the anti- $k_t$  algorithm from final-state particles within a radius of  $\Delta R =$   
 2034  $0.4$  (excluding muons and neutrinos). All jets are required to have  $p_T > 30$  GeV and lie within  $|\eta| <$   
 2035  $4.5$ ; in order to suppress jets from pileup interactions, jets outside of  $|\eta| \geq 3.8$  must pass an higher  
 2036 momentum cut of  $p_T > 70$  GeV. Jets overlapping a preselected electron within  $\Delta R(e, j) < 0.05$  are  
 2037 removed in order to prevent double counting. The two highest  $p_T$  jets are defined as the leading  
 2038 and subleading tag jets.

2039 **6.4.2 Event selection**

2040 The default event selection is summarized in Table 6.3 and described here. Exactly two signal  
 2041 leptons are required with the same electric charge and separated from each other by  $\Delta R(ll) > 0.3$ .  
 2042 In order to suppress contributions from Drell-Yan backgrounds, the two signal leptons must have  
 2043 an invariant mass  $m_{ll}$  greater than  $20$  GeV. Additionally, if both signal leptons are electrons, their  
 2044 mass must be at least  $10$  GeV away from the  $Z$ -boson mass in order to reduce background from  
 2045  $Z$ -boson decays<sup>17</sup>. The event is required to have at least  $40$  GeV of missing transverse energy ( $E_T^{\text{miss}}$ )

---

<sup>17</sup>The electron charge misidentification rate in the upgraded ATLAS detector is estimated to be high enough that contributions from  $Z \rightarrow ee$  backgrounds are non-negligible.

Selection requirement	Selection value
Lepton kinematics	$p_T > 25 \text{ GeV}$ $ \eta  \leq 4.0$
Jet kinematics	$p_T > 30 \text{ GeV}$ for $ \eta  \leq 4.5$ $p_T > 70 \text{ GeV}$ for $ \eta  > 3.8$
Dilepton charge	Exactly two signal leptons with same charge
Dilepton separation	$\Delta R_{l,l} \geq 0.3$
Dilepton mass	$m_{ll} > 20 \text{ GeV}$
$Z$ boson veto	$ m_{ee} - m_Z  > 10 \text{ GeV}$ ( $ee$ -channel only)
$E_T^{\text{miss}}$	$E_T^{\text{miss}} > 40 \text{ GeV}$
Jet selection	At least two jets with $\Delta R_{l,j} > 0.3$
$b$ jet veto	$N_{\text{b-jet}} = 0$
Dijet separation	$\Delta \eta_{jj} > 2.5$
Trilepton veto	No additional preselected leptons
Dijet mass	$m_{jj} > 500 \text{ GeV}$
Lepton-jet centrality	$\zeta > 0$

Table 6.3: Summary of the signal event selection.

2046 to account for the two final-state neutrinos. Events with additional preselected leptons are vetoed,  
 2047 which greatly reduces  $WZ$  and  $ZZ$  backgrounds.

2048 Each event must have at least two jets, and both tag jets are required to not overlap with the  
 2049 signal leptons. Events with one or more  $b$ -jets are vetoed to suppress backgrounds from heavy-flavor  
 2050 decays. In order to preferentially select EWK production, the tag jets are required to have a large  
 2051 separation between them and a large invariant mass. Finally, a cut on the lepton centrality<sup>18</sup>,  $\zeta$ ,  
 2052 defined in Equation 6.1 further enhances the EWK  $W^\pm W^\pm jj$  signal.

$$\zeta = \min[\min(\eta_{\ell 1}, \eta_{\ell 2}) - \min(\eta_{j 1}, \eta_{j 2}), \max(\eta_{j 1}, \eta_{j 2}) - \max(\eta_{\ell 1}, \eta_{\ell 2})] \quad (6.1)$$

2053

## 2054 6.5 Selection optimization

2055 The default event selection is optimized in order to improve the strength of the  $W^\pm W^\pm jj$  EWK  
 2056 signal. The expectation is that the increased detector acceptance from the forward tracking combined  
 2057 with an increase in center of mass energy and much higher integrated luminosity will allow tighter  
 2058 selection cuts without jeopardizing signal statistics.

---

<sup>18</sup> $\zeta$  is a measurement of whether the two signal leptons lie between the two tagging jets in  $\eta$ , as is preferred by the VBS topology.

2059 **6.5.1 Random grid search algorithm**

2060 The chosen method for optimizing the event selection is a cut-based algorithm known as the Random  
 2061 Grid Search (RGS) [91]. Consider a simple case of two variables  $x$  and  $y$  chosen to differentiate signal  
 2062 from background. In order to be considered a signal event, a given event would be required to pass  
 2063 a set of selection criteria, called a *cut point*:  $c = \{x > x_c, y > y_c\}$ . A simple method to choose the  
 2064 optimal cut point (i.e. the “best” values of the cuts  $x_c$  and  $y_c$ ) would be to construct an  $n \times m$   
 2065 rectangular grid in  $x$  and  $y$  consisting of points  $(x_0, y_0), (x_1, y_1), \dots, (x_n, y_m)$ , as Figure 6.3a. One  
 2066 can then choose a cut point  $c_k = \{x > x_i, y > y_j\}$  that maximizes the signal significance as given  
 2067 by a chosen metric. This would be considered a *rectangular grid search*.

2068 While effective in principle, a rectangular grid search comes with two major drawbacks:

- 2069 1. The algorithm scales exponentially as the number of variables to be optimized increases, as  
 2070 this is effectively increasing the dimensionality of the grid. In the simple case of a square grid  
 2071 with  $N$  bins per variable  $v$ , the number of cut points to be evaluated grows as  $N^v$ .
- 2072 2. Signal and background samples are rarely evenly distributed over the entire grid, resulting  
 2073 in many cut points being sub-optimal and evaluating them would be a waste of computing  
 2074 resources.

2075 To combat these limitations, the RGS algorithm constructs a grid of cut points directly from  
 2076 the signal sample itself. In the two-dimensional example, this means that the variables  $x_i$  and  $y_j$   
 2077 making up the cut point  $c_k = \{x > x_i, y > y_j\}$  take their values directly from a given signal event.  
 2078 This has the benefit of creating a *random grid* of cut points that is biased towards regions of high  
 2079 signal concentration by construction. This reduces the need for exponentially increasing numbers of  
 2080 cut points while ensuring that computing resources are not wasted in regions with few to no signal  
 2081 events. An example of a two-dimensional random grid is shown in Figure 6.3b.

2082 Once the random grid of cut points is constructed, the optimal cut point can be chosen using any  
 2083 number of metrics, such as signal to background ratio. For the purpose of the  $W^\pm W^\pm jj$  upgrade  
 2084 study, the optimal cut point is chosen to be the one that maximizes the signal significance  $Z$  as  
 2085 defined in Equation 6.2 [92]:

$$Z = \sqrt{2 \left[ (s + b) \ln \left( \frac{s + b}{b_0} \right) + b_0 - s - b \right] + \frac{(b - b_0)^2}{\sigma_b^2}} \quad (6.2)$$

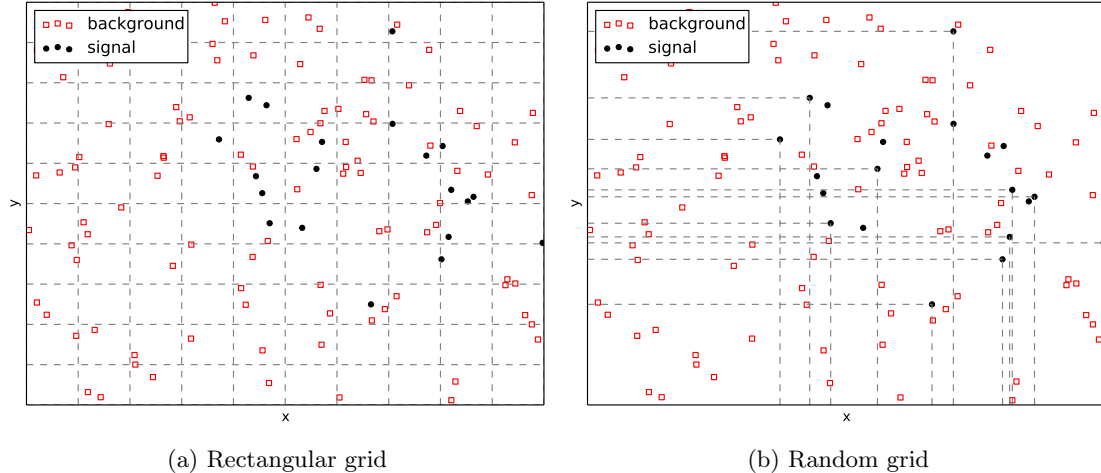


Figure 6.3: A visual representation of a two-dimensional rectangular grid (left) and a random grid (right) in variables  $x$  and  $y$ . The signal events are the black circles, and the red squares are the background events. Each intersection of gray dashed lines represents a cut point to be evaluated by the optimization.

where  $s$  and  $b$  are the number of signal and background events, respectively,  $\sigma_b$  is the total uncertainty on the background, and  $b_0$  is defined as:

$$b_0 = \frac{1}{2} \left( b - \sigma_b^2 + \sqrt{(b - \sigma_b^2)^2 + 4(s + b)\sigma_b^2} \right) \quad (6.3)$$

In the case where the background is known precisely (i.e.  $\sigma_b = 0$ ), Equation 6.2 simplifies to

$$Z = \sqrt{2 \left( b \left[ (1 + s/b) \ln(1 + s/b) - s/b \right] \right)} \quad (6.4)$$

which further reduces to the familiar  $Z = s/\sqrt{b}$  for the case when  $s \ll b$ .

### 6.5.2 Inputs to the optimization

In order to train the RGS, signal and background samples are prepared from events passing the event selection outlined in Table 6.3 up through the  $b$ -jet veto. The signal sample is chosen to be the longitudinally polarized  $W^\pm W^\pm jj$  EWK events, and the transverse and mixed polarizations are treated as background along with  $W^\pm W^\pm jj$  events from QCD interactions and the traditional backgrounds listed in Section 6.3. Splitting the inclusive  $W^\pm W^\pm jj$  EWK events by polarization allows the optimization to favor the longitudinally polarized events as much as possible, even though they both contribute to the EWK signal.

2098 The following variables are chosen for optimization:

2099     • Leading lepton  $p_T$

2100     • Dilepton invariant mass ( $m_{ll}$ )

2101     • Leading and subleading jet  $p_T$

2102     • Dijet invariant mass ( $m_{jj}$ )

2103     • Lepton-jet centrality ( $\zeta$ )

2104 Subleading lepton  $p_T$  is omitted as it is desirable to keep the cut value as low as possible due  
 2105 to its sensitivity to the longitudinal polarization (as discussed in Section 6.1.1); despite this, the  
 2106 leading lepton  $p_T$  is still allowed to be optimized as it can have strong background rejection power.  
 2107 Additionally, the dijet separation  $\Delta\eta_{jj}$  was included in early studies of the optimization, however it  
 2108 was dropped due to the cut value being motivated by well-studied differences between EWK- and  
 2109 QCD-produced  $W^\pm W^\pm jj$  events (as in Figure 5.6b).

2110 Two additional constraints were imposed when selecting the optimal cut point:

2111 1. At least 1000 signal events must survive in order to prevent the optimization from being too  
 2112 aggressive and unnecessarily reducing signal statistics.

2113 2. The dijet invariant mass may only vary within a 50 GeV range of the default value (from  
 2114 450–550 GeV) due to the cut being physically motivated by the VBS event topology described  
 2115 in Section 5.0.2.

2116 Lastly, the signal significance is calculated without taking into account the uncertainty of the  
 2117 background using Equation 6.4. This is due to the fact that the statistical uncertainties of the fake  
 2118 electron and charge misidentification backgrounds are quite large, owing to poor MC statistics in a  
 2119 few of the samples. If Equation 6.2 were used instead, the optimization would cut unreasonably  
 2120 hard against these backgrounds. Since Monte Carlo statistics is not expected to be a limiting factor  
 2121 when this analysis is performed at the HL-LHC, it is more realistic to simply ignore these large  
 2122 statistical uncertainties for the purpose of the optimization.

### 2123 6.5.3 Results of the optimization

2124 Ultimately, the random grid is constructed from over 38,000 LL-polarized  $W^\pm W^\pm jj$  events in the  
 2125 six variables listed above. After applying the constraints, the optimal cut point reduces the total  
 2126 background from 9900 to 2310 while reducing the signal from 3489 to 2958. This corresponds to

2127 an increase in signal significance from  $Z = 33.26$  to  $Z = 52.63$  as calculated by Equation 6.4. The  
 2128 updates to the event selection are listed in Table 6.4.

2129 The large reduction in the background is primarily a result of increasing the leading and sub-  
 2130 leading jet  $p_T$  from 30 GeV to 90 GeV and 45 GeV, respectively. As can be seen in Figure 6.4,  
 2131 this increase removes a significant portion of the backgrounds from jets faking electrons and charge  
 2132 mis-ID. Additionally, the loosening of the lepton-jet centrality cut  $\zeta$  allows more signal events to  
 2133 survive the event selection (see Figure 6.5). Other changes to the event selection are minor and  
 2134 do not individually have a large impact on the signal or background yields; similar distributions of  
 2135 these variables are shown in Appendix B.2.

2136 The full event yields after optimization as well as the cross section measurement are detailed  
 2137 alongside those using the default selection in Section 6.6.

Selection requirement	Selection value
Lepton kinematics	$p_T > 28$ GeV (leading lepton only)
Jet kinematics	$p_T > 90$ GeV (leading jet) $p_T > 45$ GeV (subleading jet)
Dilepton mass	$m_{ll} > 28$ GeV
Dijet mass	$m_{jj} > 520$ GeV
Lepton-jet centrality	$\zeta > -0.5$

Table 6.4: Updates to the  $W^\pm W^\pm jj$  event selection criteria after optimization. Cuts not listed remain unchanged from the default selection in Table 6.3.

## 2138 6.6 Results

### 2139 6.6.1 Event yields

2140 After applying the full event selection, the analysis is broken down into four channels based off of  
 2141 the flavor of the signal leptons:  $\mu\mu$ ,  $ee$ ,  $\mu e$ , and  $e\mu$ . The full signal and background event yields are  
 2142 shown in Table 6.5 for each channel separately and combined using the default event selection. 3489  
 2143 EWK  $W^\pm W^\pm jj$  events are expected compared to 9900 background events. The dominant sources  
 2144 of background are jets faking electrons followed by charge misidentification and diboson processes.  
 2145 Triboson events, QCD  $W^\pm W^\pm jj$ , and other non-prompt sources make up approximately 5% of the  
 2146 total background combined.

2147 The event yields for the optimized selection detailed in Section 6.5.3 are listed in Table 6.6. After  
 2148 optimization, 2958 signal events and just 2310 background events are expected. Diboson events are  
 2149 now the primary source of background, as the optimization greatly reduces the fake and charge

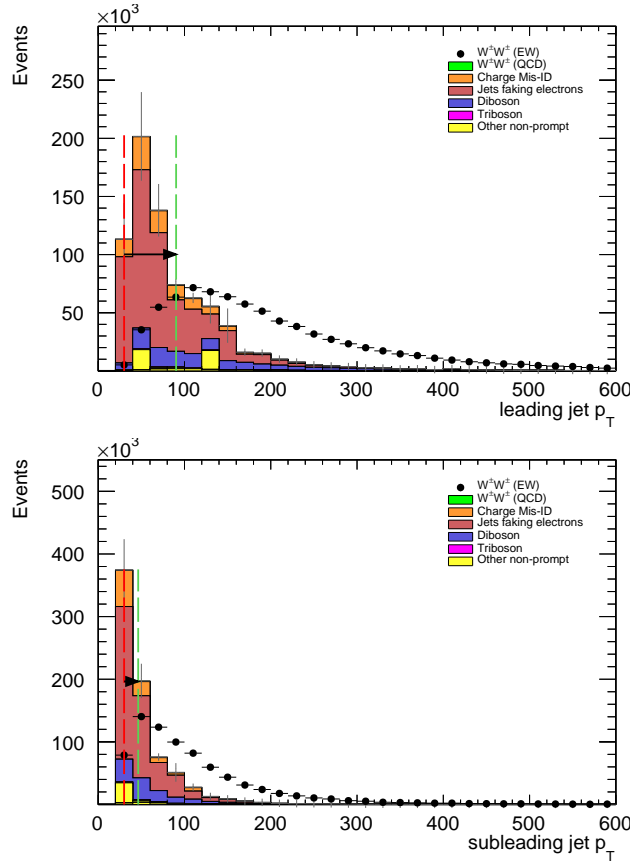


Figure 6.4: Leading (top) and subleading (bottom) jet  $p_T$  distributions. The default and optimized cuts are represented by the red and green dashed lines, respectively. The  $W^\pm W^\pm jj$  EWK signal (black points) is normalized to the same area as the sum of the backgrounds (colored histogram).

	All channels	$\mu\mu$	$ee$	$\mu e$	$e\mu$
$W^\pm W^\pm jj$ (QCD)	206.4	91.1	22.8	38.4	54.1
Charge Misidentification	2300	0.0	2100	90	160
Jets faking electrons	5000	0.0	3400	1200	340
$WZ + ZZ$	2040	500	438	423	680
Tribosons	115	47	15.4	21.6	31.2
Other non-prompt	210	110	20	60	27
Total Background	9900	750	6000	1900	1290
Signal $W^\pm W^\pm jj$ (EWK)	3489	1435	432	679	944

Table 6.5: Signal and background event yields using the default event selection for an integrated luminosity of  $\mathcal{L} = 3000 \text{ fb}^{-1}$ . Events containing a fake or charge-flipped electron are removed from their respective sources and combined into a single entry each.

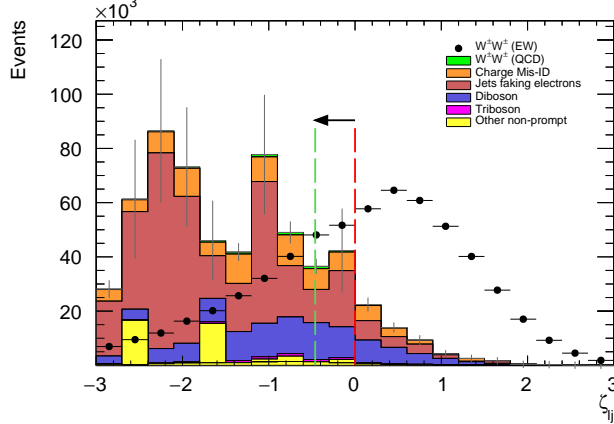


Figure 6.5: Lepton-jet centrality distribution. The default and optimized cuts are represented by the red and green dashed lines, respectively. The  $W^\pm W^\pm jj$  EWK signal (black points) is normalized to the same area as the sum of the backgrounds (colored histogram).

mis-ID contributions. As discussed earlier, the increase in the leading and subleading jet  $p_T$  cuts as well as the loosening of the centrality cut are most responsible for the changes in the signal and background yields; distributions of these quantities using the default and the optimized event selections can be found in Figures 6.6, 6.7, and 6.8, respectively.

	All channels	$\mu\mu$	$ee$	$\mu e$	$e\mu$
$W^\pm W^\pm jj$ (QCD)	168.7	74.6	19.7	32.2	42.2
Charge Misidentification	200	0.0	11	30	160
Jets faking electrons	460	0.0	130	260	70
$WZ + ZZ$	1286	322	289	271	404
Tribosons	76	30.1	9.6	15.1	21.6
Other non-prompt	120	29	16.6	50	19
Total Background	2310	455	480	660	710
Signal $W^\pm W^\pm jj$ (EWK)	2958	1228	380	589	761

Table 6.6: Signal and background event yields using the optimized event selection for an integrated luminosity of  $\mathcal{L} = 3000 \text{ fb}^{-1}$ . Events containing a fake or charge-flipped electron are removed from their respective sources and combined into a single entry each.

It is important to note, however, that the MC sample used to estimate  $Z+jets$  events suffers from poor statistics which results in large per-event weights once scaled to  $\mathcal{L} = 3000 \text{ fb}^{-1}$ . This sample contributes heavily to the fake and charge misidentification backgrounds, and a handful of these events being cut out by the optimization is largely responsible for the dramatic reduction of the corresponding backgrounds. As a result, the optimized results presented here are likely overly optimistic. However, given proper MC statistics, it is still expected that this optimization will

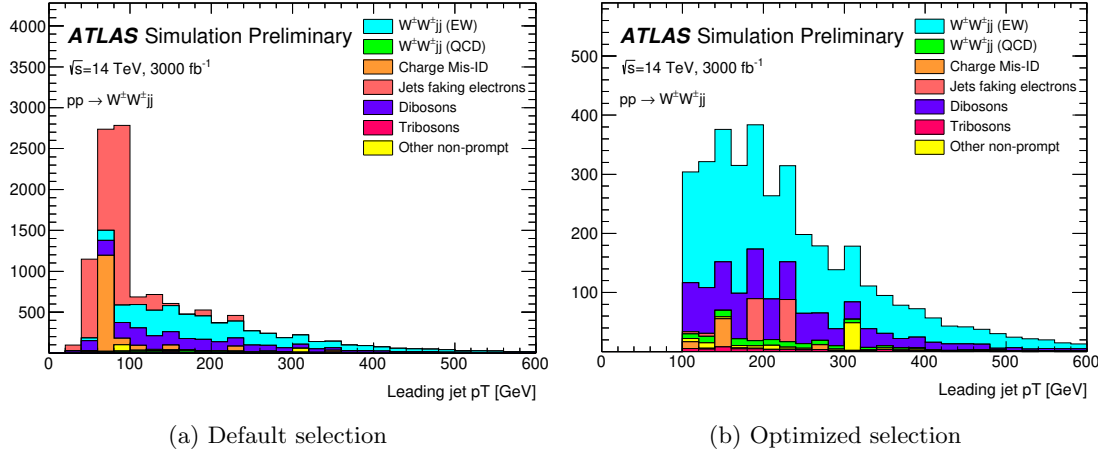


Figure 6.6:  $p_T$  distributions for the leading jet using the default (left) and optimized (right) event selections for all channels combined.

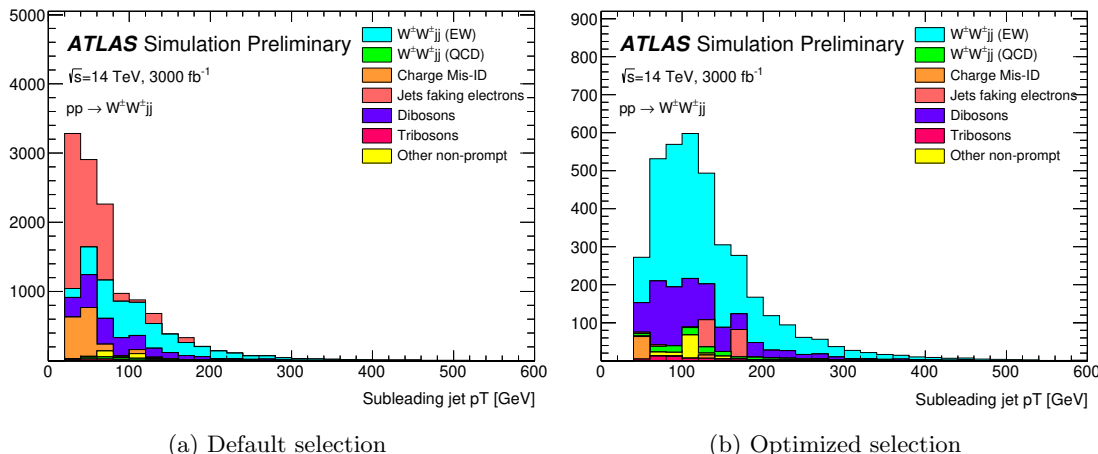


Figure 6.7:  $p_T$  distributions for the subleading jet using the default (left) and optimized (right) event selections for all channels combined.

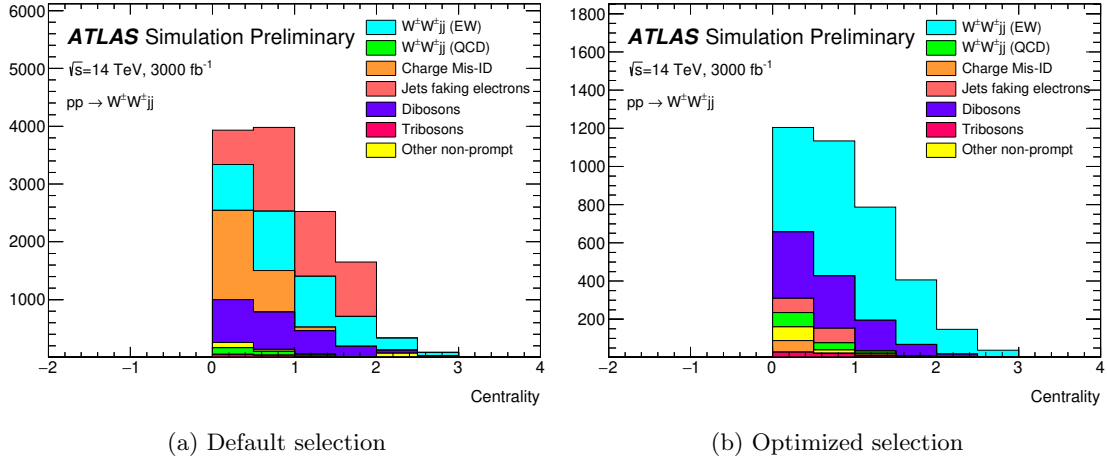


Figure 6.8:  $p_T$  distributions for lepton-jet centrality  $\zeta$  using the default (left) and optimized (right) event selections for all channels combined.

outperform the default selection.

### 6.6.2 Uncertainties

The uncertainties considered for the analysis are summarized in Table 6.7. Values for experimental systematics on the trigger efficiency, lepton and jet reconstruction, and flavor tagging are taken directly from the 13 TeV analysis [48]. The rate uncertainties for the background processes are halved from the 13 TeV values according to ATLAS recommendations. The uncertainty on the fake electron estimation is also halved from the 13 TeV analysis. Finally, a conservative estimate of the uncertainty on the charge flip background is used as the electron charge mis-ID rate due to material interactions is difficult to predict at this stage.

### 6.6.3 Cross section measurement

The cross section is calculated using the same method as in the 13 TeV analysis, detailed in Section 5.4. Unlike the previous analysis, however, eight lepton channels are used here instead of six. The  $\mu e$  and  $e\mu$  channels remain separated in addition to the  $\mu\mu$  and  $ee$  channels, and each lepton flavor channel is further split by charge (i.e.  $\mu\mu \rightarrow \mu^+\mu^+ + \mu^-\mu^-$ ), as this increases the sensitivity of the analysis. Each channel's  $m_{jj}$  distribution is combined in a profile likelihood fit to extract the EWK  $W^\pm W^\pm jj$  production cross section. Using the default event selection, the expected cross

Source	Uncertainty (%)
$W^\pm W^\pm jj$ (EWK)	3
Luminosity	1
Trigger efficiency	0.5
Lepton reconstruction and identification	1.8
Jets	2.3
Flavor tagging	1.8
Jets faking electrons	20
Charge misidentification	25
$W^\pm W^\pm jj$ (QCD)	20
Top	15
Diboson	10
Triboson	15

Table 6.7: Summary of estimated experimental and rate uncertainties.

2176 section calculated to be:

$$\sigma_{W^\pm W^\pm jj}^{\text{expected}} = 16.89 \pm 0.36 \text{ (stat)} \pm 0.53 \text{ (theory)} \pm 0.84 \text{ (syst)} \text{ fb} \quad (6.5)$$

2177 and with the optimized event selection:

$$\sigma_{W^\pm W^\pm jj}^{\text{expected}} = 16.94 \pm 0.36 \text{ (stat)} \pm 0.53 \text{ (theory)} \pm 0.78 \text{ (syst)} \text{ fb} \quad (6.6)$$

2178 The optimized selection should not change the measured value of the cross section, and indeed both  
 2179 are consistent with within uncertainties. The systematic uncertainty is reduced by approximately  
 2180 7% with the optimized selection. The total uncertainty on the cross section measurement is approx-  
 2181 imately 6%, compared to approximately 20% on the measured fiducial cross section of the 13 TeV  
 2182 analysis reported in Equation 5.30.

2183 Projections of each uncertainty type and the total uncertainty on the cross section as a function of  
 2184 integrated luminosity are shown in Figure 6.9. The predictions are made by scaling the event yields  
 2185 by different luminosity values and re-running the fitting procedure. As the integrated luminosity  
 2186 increases past  $\mathcal{L} > 3000 \text{ fb}^{-1}$ , the statistical uncertainty continues to reduce; however, the total  
 2187 uncertainty becomes limited by the systematics. Additionally, the total uncertainty is expected to  
 2188 reduce by less than a percent as the integrated luminosity increases past the planned  $3000 \text{ fb}^{-1}$ .

#### 2189 6.6.4 Longitudinal scattering significance

2190 The longitudinal scattering significance is extracted in much the same way as the cross section, this  
 2191 time using a binned likelihood fit on the  $|\Delta\phi_{jj}|$  distribution. In order to increase sensitivity, the

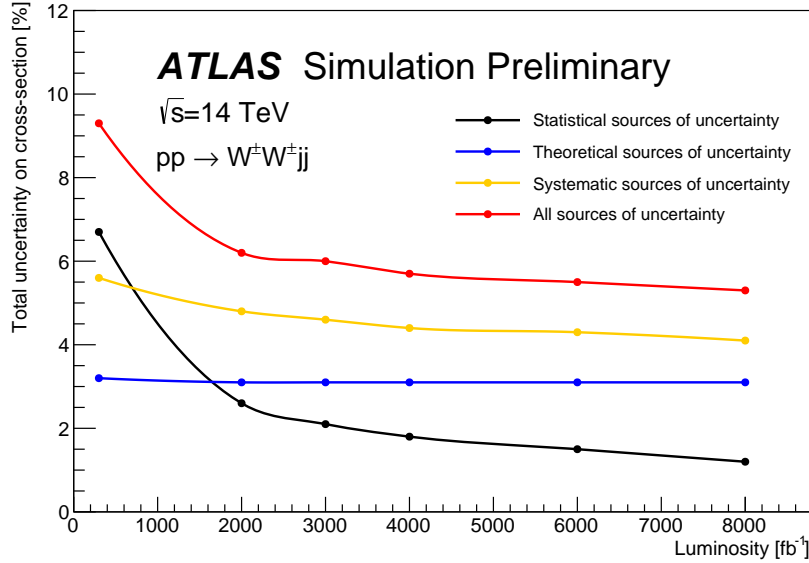


Figure 6.9: Projections of the statistical (black), theoretical (blue), systematic (yellow), and total (red) uncertainties on the measured cross section as a function of integrated luminosity using the optimized event selection.

2192     $|\Delta\phi_{jj}|$  distribution is split into two bins in  $m_{jj}$ , and an additional cut on the pseudorapidity of the  
 2193    subleading lepton is applied ( $|\eta| < 2.5$ ) to reduce background contributions from fake electrons and  
 2194    charge flip. The  $|\Delta\phi_{jj}|$  distributions used in the fit are shown in Figure 6.10. Due to limited statistics  
 2195    in the LL events, the four lepton flavor channels are not split by charge. The expected significance  
 2196    of the  $W_L^\pm W_L^\pm jj$  process is  $1.8\sigma$  with a precision of 47% on the measurement. Projections of the  
 2197    expected significance as a function of integrated luminosity is shown in Figure 6.11.

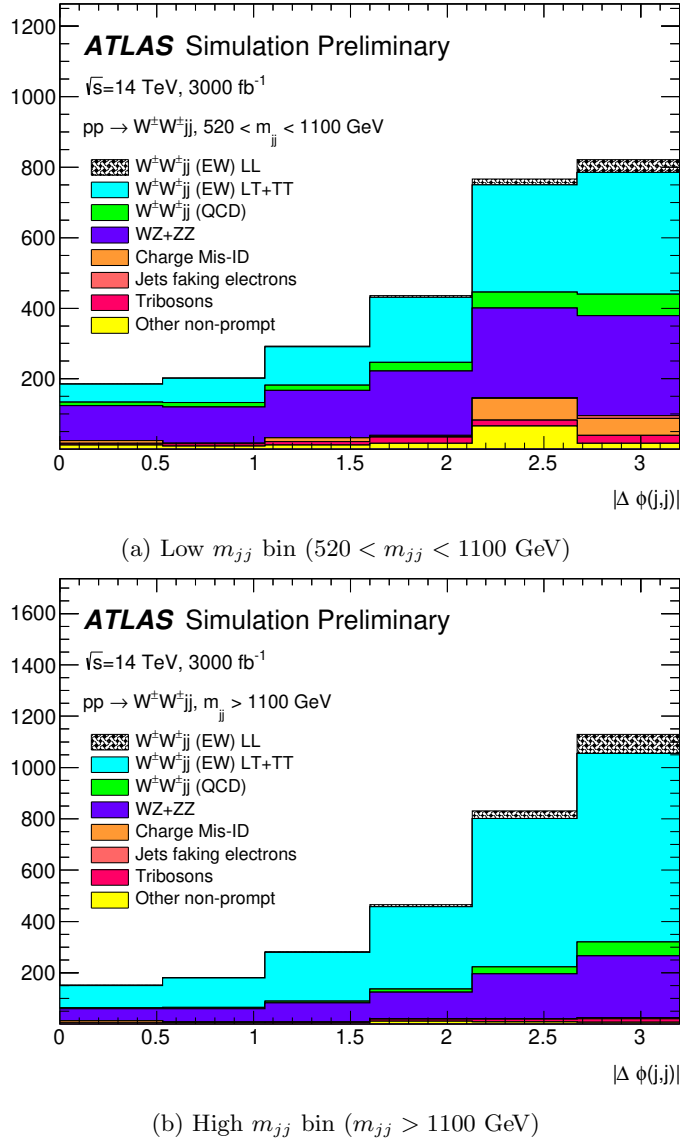


Figure 6.10: Dijet azimuthal separation ( $|\Delta\phi_{jj}|$ ) for the low  $m_{jj}$  region ( $520 < m_{jj} < 1100$  GeV, top) and the high  $m_{jj}$  region ( $m_{jj} > 1100$  GeV, bottom). The purely longitudinal (LL, gray) is plotted separately from the mixed and transverse (LT+TT, cyan) polarizations.

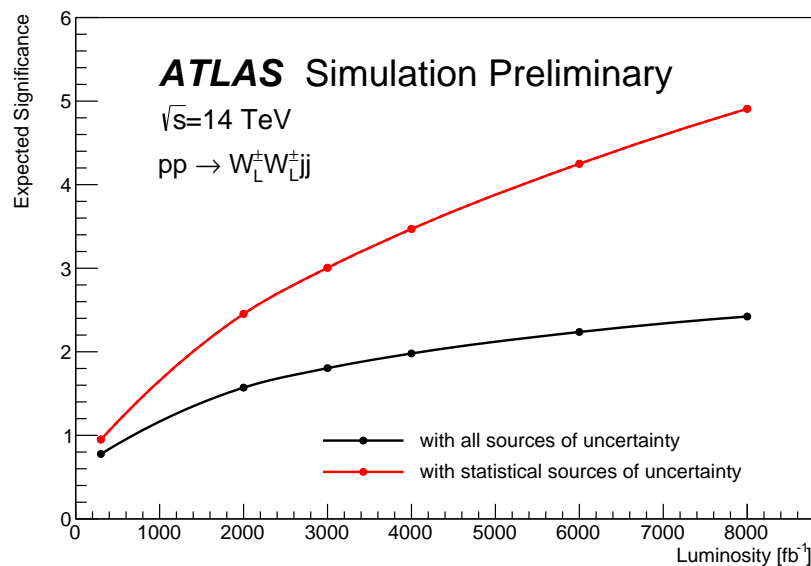


Figure 6.11: Projections of the expected longitudinal scattering significance as a function of integrated luminosity when considering all sources of uncertainties (black) or only statistical uncertainties (red).

2198

## CHAPTER 7

---

2199

## Conclusion

---

2200 Here's where you wrap it up.

2201

## APPENDIX A

2202

### Additional material on

2203

### $W^\pm W^\pm jj$ measurement at $\sqrt{s} = 13$ TeV

2204

#### A.1 Impact of experimental uncertainty on MC background estimations

2205 Tables A.1-A.6 contain the impact of experimental systematic uncertainties for the remaining back-  
2206 grounds estimated from MC simulation. The  $W^\pm W^\pm jj$  EWK signal and  $WZ$  background sys-  
2207 tematics are listed in the main body of the document, in Tables 5.21 and 5.22, respectively. While the  
2208 percentage of the contributions for some systematics appear large, the size of these backgrounds are  
2209 quite small compared to the total background.

$W^\pm W^\pm jj$ QCD	$ee$ % Yield	$e\mu$ % Yield	$\mu\mu$ % Yield
Jet-related Uncertainties	3.41	3.04	2.85
b-tagging efficiency	2.56	2.48	2.48
Pile-up	4.99	0.45	0.33
Trigger efficiency	0.02	0.08	0.41
Lepton reconstruction/ID	1.62	1.19	1.89
MET reconstruction	0.41	0.22	0.34

Table A.1: Impact of experimental uncertainties for the  $W^\pm W^\pm jj$  QCD processes in all channels.

Triboson	$ee$ % Yield	$e\mu$ % Yield	$\mu\mu$ % Yield
Jet-related Uncertainties	13.09	13.39	16.85
b-tagging efficiency	2.96	3.77	4.95
Pile-up	19.37	24.66	6.87
Trigger efficiency	0.02	0.07	0.47
Lepton reconstruction/ID	1.66	1.27	2.48
MET reconstruction	0.00	0.46	0.00

Table A.2: Impact of experimental uncertainties for triboson process in all channels.

$t\bar{t}V$	$ee$ % Yield	$e\mu$ % Yield	$\mu\mu$ % Yield
Jet-related Uncertainties	17.65	11.97	14.27
b-tagging efficiency	15.02	9.04	13.83
Pile-up	8.73	10.69	4.18
Trigger efficiency	0.03	0.08	0.39
Lepton reconstruction/ID	2.57	3.27	2.66
MET reconstruction	1.75	4.16	1.62

Table A.3: Impact of experimental uncertainties for  $t\bar{t}V$  processes in all channels.

$W\gamma$	$ee$ % Yield	$e\mu$ % Yield	$\mu\mu$ % Yield
Jet-related Uncertainties	7.05	33.36	—
b-tagging efficiency	1.97	2.94	—
Pile-up	4.11	14.17	—
Trigger efficiency	0.01	0.14	—
Lepton reconstruction/ID	1.40	1.13	—
MET reconstruction	0.00	0.00	—

Table A.4: Impact of experimental uncertainties for the  $W\gamma$  process in all channels.

$Z\gamma$	$ee$ % Yield	$e\mu$ % Yield	$\mu\mu$ % Yield
Jet-related Uncertainties	16.22	370.44	—
b-tagging efficiency	1.08	3.10	—
Pile-up	12.57	11.51	—
Trigger efficiency	0.02	0.07	—
Lepton reconstruction/ID	1.26	22.01	—
MET reconstruction	0.00	0.00	—

Table A.5: Impact of experimental uncertainties for the  $Z\gamma$  process in all channels.

$ZZ$	$ee$ % Yield	$e\mu$ % Yield	$\mu\mu$ % Yield
Jet-related Uncertainties	15.71	15.76	35.18
b-tagging efficiency	2.23	2.35	2.89
Pile-up	1.22	3.20	4.58
Trigger efficiency	0.03	0.10	0.36
Lepton reconstruction/ID	3.59	3.10	5.70
MET reconstruction	4.84	3.26	3.24

Table A.6: Impact of experimental uncertainties for the  $ZZ$  process in all channels.

2210 **A.2 Additional signal region plots**

2211

## APPENDIX B

2212

2213

# Additional material on $W^\pm W^\pm jj$ prospects at the HL-LHC

2214

## B.1 Truth isolation

2215 As mentioned in Section 6.3.1, the size of the background contribution from top processes are much  
 2216 larger than expected when no isolation is applied. The event yields using an earlier version of the  
 2217 event selection with no truth-based isolation requirement are listed in Table B.1. Here, top events  
 2218 make up nearly 90% of the total background, and the contributions from fake and charge-flipped  
 2219 electrons are also large. The event yields using the same event selection with the truth-based isolation  
 2220 included are shown in Figure B.2. When comparing the two tables, the considerable reduction in  
 the top background can be clearly seen.

yields by type	all channels	$\mu\mu$	$ee$	$\mu e$	$e\mu$
signal	4011	1583.2	531.7	793.1	1103.1
ww qcd	252.6	105.8	30.4	48	68.4
charge flip	2528.4	0.0	2075.4	255.1	197.8
fakes	7135.4	0.0	4675.1	1904.3	555.9
diboson	2370.4	581.2	491.8	517.9	779.6
triboson	125.5	49.1	17.8	24.6	34.1
top	90150.5	26618	15301.6	25277.9	22953.1
z+jets	241.2	0.0	0.0	0.0	241.2
w+jets	31.4	3.9	7.6	13.2	6.7
total bkg	102803.9	27354	22592	28027.8	24830.1
signal	4011	1583.2	531.7	793.1	1103.1

Table B.1: Event yields prior to applying any form of truth-based isolation criteria.

2221

2222

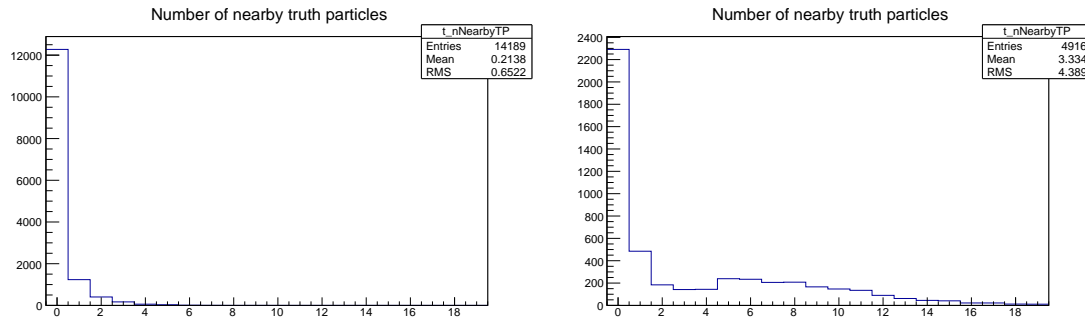
TODO: Add tables for tight vs loose working point, information on the necessity of TRUTH1++

yields by type	all channels	$\mu\mu$	$ee$	$\mu e$	$e\mu$
signal	3470.5	1427.3	428.8	675.8	938.7
ww qcd	205.8	90.8	22.7	38.3	54
charge flip	2398.3	0.0	2104.6	95.8	197.9
fakes	4309.7	0.0	3390.6	750.8	168.3
diboson	1552.4	311.3	355.6	346.8	538.7
triboson	115	46.8	15.4	21.6	31.2
top	156.9	42.3	14.8	76.6	23.3
$z+jets$	0.0	0.0	0.0	0.0	0.0
$w+jets$	0.3	0.0	0.0	0.3	0.0
total bkg	8738.1	491.3	5903.7	1329.8	1013.4
signal	3470.5	1427.3	428.8	675.8	938.7

Table B.2: Event yields after applying a test version of the truth-based isolation.

### 2223 B.1.1 TRUTH1++ derivations

2224 The ATLAS standard TRUTH1 derivations used for this analysis contain a slimmed truth particle  
 2225 container in order to reduce the file size. As a result, many of the truth particles that would be  
 2226 included in the isolation variables are missing, and the truth-based isolation will not accurately  
 2227 model the reconstruction-level isolation variables. In order to recover the performance of the truth-  
 2228 based isolation in the top MC samples (where it is most needed), a custom derivation was produced  
 2229 privately that duplicated the default TRUTH1 data structure but includes the full truth particle  
 2230 record. The reduced size of the truth particle information in the TRUTH1 derivation compared to the  
 2231 TRUTH1++ derivation is shown in Figure B.1.

Figure B.1: Number of truth particles within  $\Delta R < 0.4$  of a selected muon or electron using the ATLAS standard TRUTH1 (left) and the custom TRUTH1++ (right) derivations in  $t\bar{t}$  simulation. The complete truth record is stored in the TRUTH1++ derivation, and this is best seen in the first bin, where the lepton has no nearby truth particles.

---

**2232    B.1.2 Check of truth-based isolation**

2233 Since the isolation variables are constructed from truth particles, there is an expectation that the  
 2234 efficiency of the isolation selection will be higher than what would be seen in the full simulation.  
 2235 In order to test this, a truth-level 13 TeV  $t\bar{t}$  MC sample was run through a selection altered to  
 2236 mimic the 13 TeV  $W^\pm W^\pm jj$  measurement as closely as possible. The results were compared to the  
 2237  $t\bar{t}$  background in the 13 TeV analysis extrapolated to 14 TeV and  $3000 \text{ fb}^{-1}$ , and the truth-based  
 2238 isolation reduces the expected events by a factor of approximately 4. However, the statistics in the  
 2239 13 TeV truth-level sample are low, and it is therefore difficult to measure precisely how much the  
 2240 truth-based isolation overperforms.

**2241    B.1.3 Loose isolation working point**

2242 As another check on the truth-based isolation, a second isolation working point was constructed  
 2243 to match the official ATLAS Fixed Cut Loose isolation working point. The definition of this loose  
 2244 isolation are found in Table B.3.

2245 The primary impact of loosening the isolation is a substantial increase in the non-prompt back-  
 2246 round from top processes, and a moderate increase in the charge mis-ID and fake backgrounds.  
 2247 Backgrounds from prompt leptons only did not see major changes. As a result, the tight working  
 2248 point is chosen for the analysis. The event yields by sample and by background type using the  
 2249 loose working point are in Table B.4, and Table B.5 has the numbers using the tight working point  
 2250 (defined in Table 6.2) for comparison.

	Electron Isolation	Muon Isolation
Track-based isolation cone size	$\Delta R < 0.2$	$\Delta R < 0.3$
Track-based isolation requirement	$\sum p_T/p_T^e < 0.15$	$\sum p_T/p_T^\mu < 0.15$
Calorimeter-based isolation cone size	$\Delta R < 0.2$	$\Delta R < 0.2$
Calorimeter-based isolation requirement	$\sum E_T/p_T^e < 0.2$	$\sum E_T/p_T^\mu < 0.3$

Table B.3: Electron and muon isolation requirements for the loose working point.

run number	all channels			mm			ee			me			em		
	events	stat	sys	events	stat	sys	events	stat	sys	events	stat	sys	events	stat	sys
signal	3783.21	22.08	0.00	1524.99	15.00	0.00	484.74	7.01	0.00	740.76	9.01	0.00	1032.72	11.50	0.00
ww qcd	223.95	3.54	44.79	97.17	2.51	19.43	25.51	1.03	5.10	42.23	1.40	8.45	59.04	1.80	11.81
charge flip	3025.40	1276.74	0.00	0.00	0.00	0.00	2615.30	1267.89	0.00	197.20	87.94	0.00	212.90	121.63	0.00
fakes	5315.55	1775.87	0.00	0.00	0.00	0.00	3524.24	1694.39	0.00	1356.74	450.60	0.00	434.57	282.33	0.00
diboson	2195.61	38.10	219.58	548.72	18.54	54.87	451.27	18.29	45.14	470.61	15.71	47.07	725.01	22.95	72.50
triboson	117.43	5.90	17.62	47.55	4.32	7.13	15.83	1.94	2.37	22.11	2.18	3.32	31.94	2.76	4.80
top	554.63	218.75	83.21	229.26	135.53	34.40	61.15	38.23	9.18	232.30	167.28	34.85	31.92	6.43	4.78
z+jets	0.00	0.00	0.00	0.00	0.00	0.00	0.00	0.00	0.00	0.00	0.00	0.00	0.00	0.00	0.00
w+jets	1.21	0.87	0.00	0.00	0.00	0.00	0.00	0.00	0.00	0.00	0.00	0.00	0.02	0.00	0.00
total bkg	11433.78	2198.44	239.70	922.70	136.88	67.99	6693.30	2116.67	46.41	2322.38	488.89	59.27	1495.40	308.36	73.77
signal	3783.21	22.08	0.00	1524.99	15.00	0.00	484.74	7.01	0.00	740.76	9.01	0.00	1032.72	11.50	0.00

Table B.4: Event yields broken down by sample and by background type using the loose isolation workingpoint. Events containing a fake or charge-flipped electron are removed from their respective sample and added to the ‘fakes’ and ‘charge flip’ rows, respectively. Errors include statistical uncertainty and estimated systematic rate uncertainty based on the background process.

run number	all channels			mm			ee			me			em		
	events	stat	sys	events	stat	sys	events	stat	sys	events	stat	sys	events	stat	sys
signal	3489.49	21.23	0.00	1434.85	14.55	0.00	431.75	6.61	0.00	679.09	8.63	0.00	943.8	11.00	0.00
ww qcd	206.42	3.41	41.28	91.12	2.43	18.22	22.84	0.98	4.57	38.37	1.34	7.67	54.09	1.72	10.82
charge flip	2335.73	1163.47	0.00	0.00	0.00	0.00	2087.78	1159.5	0.00	90.37	33.32	0.00	157.58	90.02	0.00
fakes	4979.27	1756.47	0.00	0.00	0.00	0.00	3406.20	1705.03	0.00	1230.80	362.15	0.00	342.27	216.54	0.00
diboson	2039.94	36.93	204.00	499.69	18.04	49.97	437.60	14.12	43.76	422.90	14.18	42.29	679.75	25.25	67.98
triboson	115.03	5.87	17.29	46.84	4.31	7.03	15.40	1.94	2.32	21.55	2.17	3.24	31.24	2.74	4.70
top	211.74	84.14	31.76	107.96	71.12	16.20	19.58	3.76	2.93	57.21	44.47	8.58	26.99	5.40	4.05
z+jets	0.00	0.00	0.00	0.00	0.00	0.00	0.00	0.00	0.00	0.00	0.00	0.00	0.00	0.00	0.00
w+jets	0.30	0.28	0.00	0.00	0.00	0.00	0.00	0.00	0.00	0.28	0.28	0.00	0.02	0.02	0.00
total bkg	9888.43	2108.87	211.25	745.61	73.54	56.04	5898.40	2061.99	44.16	1861.48	366.67	43.95	1291.94	235.95	69.11
signal	3489.49	21.23	0.00	1434.85	14.55	0.00	431.75	6.61	0.00	679.09	8.63	0.00	943.80	11.00	0.00

Table B.5: Event yields broken down by background type using the tight isolation workingpoint. Events containing a fake or charge-flipped electron are removed from their respective sample and added to the “fakes” and “charge flip” rows, respectively. Errors include statistical uncertainty and estimated systematic rate uncertainty based on the background process.

## 2251 B.2 Plots of other optimization variables

2252 Plots of the remaining optimization variables not shown in Section 6.5.3 are presented here for  
 2253 reference. Figures B.2, B.3, and B.4 compare signal and background distributions for the default  
 2254 and optimized cuts. None of these cuts change by much in the optimized selection and their impacts  
 2255 on the overall event selection is minimal.

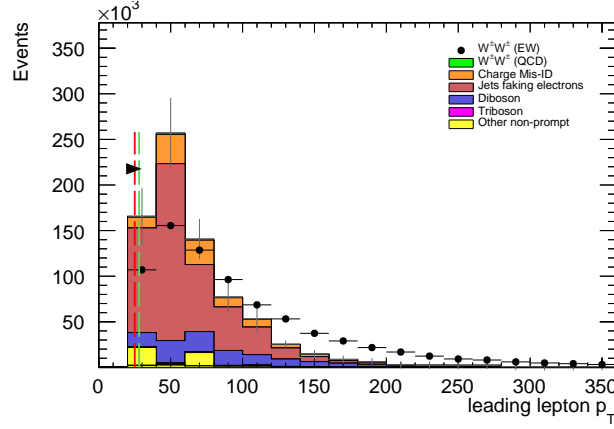


Figure B.2: Leading lepton  $p_T$  distribution. The default and optimized cuts are represented by the red and green dashed lines, respectively. The  $W^\pm W^\pm jj$  EWK signal (black points) is normalized to the same area as the sum of the backgrounds (colored histogram).

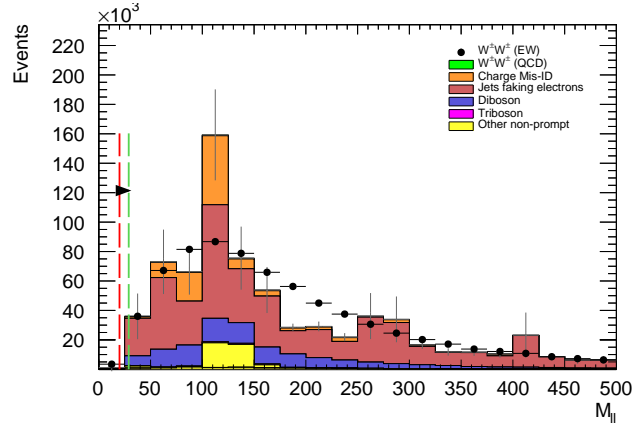


Figure B.3: Dilepton invariant mass distribution. The default and optimized cuts are represented by the red and green dashed lines, respectively. The  $W^\pm W^\pm jj$  EWK signal (black points) is normalized to the same area as the sum of the backgrounds (colored histogram).

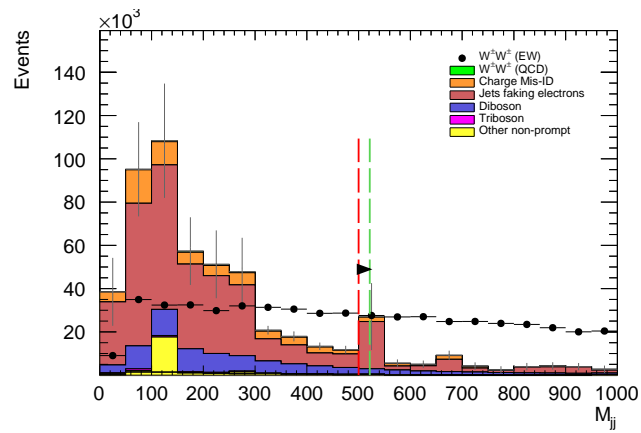


Figure B.4: Dijet invariant mass distribution. The default and optimized cuts are represented by the red and green dashed lines, respectively. The  $W^\pm W^\pm jj$  EWK signal (black points) is normalized to the same area as the sum of the backgrounds (colored histogram).

---

## Bibliography

---

- 2257 [1] ATLAS Collaboration, M. Aaboud et al., *Measurement of the  $W^\pm Z$  boson pair-production*  
 2258 *cross section in  $pp$  collisions at  $\sqrt{s} = 13$  TeV with the ATLAS Detector*, *Phys. Lett.* **B762**  
 2259 (2016) 1–22, [arXiv:1606.04017 \[hep-ex\]](#). (document)
- 2260 [2] S. Weinberg, *The Quantum Theory of Fields, Volume 1: Foundations*. Cambridge University  
 2261 Press, 1995. [2.1](#)
- 2262 [3] M. E. Peskin and D. V. Schroeder, *An Introduction to Quantum Field Theory*.  
 2263 Addison-Wesley, 1995. [2.1](#)
- 2264 [4] R. P. Feynman, *Mathematical formulation of the quantum theory of electromagnetic*  
 2265 *interaction*, *Phys. Rev.* **80** (1950) 440–457. [2.1](#)
- 2266 [5] M. Y. Han and Y. Nambu, *Three-triplet model with double SU(3) symmetry*, *Phys. Rev.* **139**  
 2267 (1965) B1006–B1010. [2.1](#)
- 2268 [6] D. J. Gross and F. Wilczek, *Asymptotically Free Gauge Theories - I*, *Phys. Rev.* **D8** (1973)  
 2269 3633–3652. [2.1](#)
- 2270 [7] D. J. Gross and F. Wilczek, *ASYMPTOTICALLY FREE GAUGE THEORIES. 2.*, *Phys.*  
 2271 *Rev.* **D9** (1974) 980–993. [2.1](#)
- 2272 [8] H. D. Politzer, *Reliable Perturbative Results for Strong Interactions?*, *Phys. Rev. Lett.* **30**  
 2273 (1973) 1346–1349. [,274(1973)]. [2.1](#)
- 2274 [9] A. Salam and J. C. Ward, *Weak and Electromagnetic Interactions*, *Nuovo Cimento* **11** (1959)  
 2275 568–577. [2.1](#)
- 2276 [10] S. L. Glashow, *The Renormalizability of Vector Meson Interactions*, *Nucl. Phys.* **10** (1959)  
 2277 107–117. [2.1](#)
- 2278 [11] ALEPH, DELPHI, L3, OPAL, SLD, LEP Electroweak Working Group, SLD Electroweak  
 2279 Group, SLD Heavy Flavour Group Collaboration, S. Schael et al., *Precision electroweak*  
 2280 *measurements on the  $Z$  resonance*, *Phys. Rept.* **427** (2006) 257–454, [arXiv:hep-ex/0509008](#)  
 2281 [hep-ex]. [2.1](#)
- 2282 [12] F. Englert and R. Brout, *Broken symmetry and the mass of gauge vector mesons*, *Phys. Rev.*  
 2283 *Lett.* **13** (1964) 321–323. [2.1](#)

- 2284 [13] P. W. Higgs, *Broken symmetries, massless particles and gauge fields*, Physics Letters **12**  
 2285 (1964) 132–133. 2.1
- 2286 [14] P. W. Higgs, *Broken symmetries and the masses of gauge bosons*, Phys. Rev. Lett. **13** (1964)  
 2287 508–509. 2.1
- 2288 [15] ATLAS Collaboration, *Observation of a new particle in the search for the Standard Model*  
 2289 *Higgs boson with the ATLAS detector at the LHC*, Phys. Lett. B **716** (2012) 1,  
 2290 arXiv:1207.7214 [hep-ex]. 2.1, 5.0.1
- 2291 [16] CMS Collaboration, *Observation of a new boson at a mass of 125 GeV with the CMS*  
 2292 *experiment at the LHC*, Phys. Lett. B **716** (2012) 30, arXiv:1207.7235 [hep-ex]. 2.1, 5.0.1
- 2293 [17] UA1 Collaboration, G. Arnison et al., *Experimental Observation of Isolated Large Transverse*  
 2294 *Energy Electrons with Associated Missing Energy at  $s^{**}(1/2) = 540\text{-GeV}$* , Phys. Lett. **B122**  
 2295 (1983) 103–116. [,611(1983)]. 2.2
- 2296 [18] UA1 Collaboration, G. Arnison et al., *Experimental Observation of Lepton Pairs of Invariant*  
 2297 *Mass Around  $95\text{-GeV}/c^{**2}$  at the CERN SPS Collider*, Phys. Lett. **B126** (1983) 398–410.  
 2298 [,7.55(1983)]. 2.2
- 2299 [19] Particle Data Group Collaboration, K. A. Olive et al., *Review of Particle Physics*, Chin.  
 2300 Phys. **C38** (2014) 090001. 2.2, 2.2
- 2301 [20] D. R. Green, P. Meade, and M.-A. Pleier, *Multiboson interactions at the LHC*, Rev. Mod.  
 2302 Phys. **89** (2017) no. 3, 035008, arXiv:1610.07572 [hep-ex]. 2.3
- 2303 [21] H.-J. He and W. B. Kilgore, *The Equivalence theorem and its radiative correction - free*  
 2304 *formulation for all  $R(xi)$  gauges*, Phys. Rev. **D55** (1997) 1515–1532, arXiv:hep-ph/9609326  
 2305 [hep-ph]. 2.3
- 2306 [22] B. W. Lee, C. Quigg, and H. B. Thacker, *The Strength of Weak Interactions at Very*  
 2307 *High-Energies and the Higgs Boson Mass*, Phys. Rev. Lett. **38** (1977) 883–885. 2.3
- 2308 [23] S. D. Rindani, *Strong gauge boson scattering at the LHC*, in *Physics at the Large Hadron*  
 2309 *Collider*, A. Datta, B. Mukhopadhyaya, A. Raychaudhuri, A. K. Gupta, C. L. Khetrapal,  
 2310 T. Padmanabhan, and M. Vijayan, eds., pp. 145–155. 2009. arXiv:0910.5068 [hep-ph]. 2.3, 2.3
- 2311 [24] V. D. Barger, K.-m. Cheung, T. Han, and R. J. N. Phillips, *Strong  $W^+W^+$  scattering signals*  
 2312 *at pp supercolliders*, Phys. Rev. **D42** (1990) 3052–3077. 2.3
- 2313 [25] G. van den Oord, *Recursion, Monte Carlo and Vector Boson Scattering at Hadron Colliders*.  
 2314 PhD thesis, Nijmegen U., 2012.  
 2315 [http://www.nikhef.nl/pub/services/biblio/theses\\_pdf/thesis\\_G\\_v\\_d\\_Oord.pdf](http://www.nikhef.nl/pub/services/biblio/theses_pdf/thesis_G_v_d_Oord.pdf). 2.3,  
 2316 2.3
- 2317 [26] A. Alboteanu, W. Kilian, and J. Reuter, *Resonances and Unitarity in Weak Boson Scattering*  
 2318 *at the LHC*, JHEP **11** (2008) 010, arXiv:0806.4145 [hep-ph]. 2.5
- 2319 [27] L. R. Evans and P. Bryant, *LHC Machine*, JINST **3** (2008) S08001.  
 2320 <https://cds.cern.ch/record/1129806>. This report is an abridged version of the LHC  
 2321 Design Report (CERN-2004-003). 3.1

- 2322 [28] ATLAS Collaboration, *The ATLAS Experiment at the CERN Large Hadron Collider*, JINST  
2323 **3** (2008) S08003. 3.1
- 2324 [29] ATLAS Collaboration, *ATLAS inner detector: Technical Design Report, Vol. 1*. CERN,  
2325 Geneva, 1997. <https://cds.cern.ch/record/331063>. 4
- 2326 [30] P. F. Åkesson, T. Atkinson, M. J. Costa, M. Elsing, S. Fleischmann, A. N. Gaponenko,  
2327 W. Liebig, E. Moyse, A. Salzburger, and M. Siebel, *ATLAS Tracking Event Data Model*,  
2328 Tech. Rep. ATL-SOFT-PUB-2006-004. ATL-COM-SOFT-2006-005.  
2329 CERN-ATL-COM-SOFT-2006-005, CERN, Geneva, Jul, 2006.  
2330 <https://cds.cern.ch/record/973401>. 4.1
- 2331 [31] P. Brückman, A. Hicheur, and S. J. Haywood, *Global chi2 approach to the Alignment of the*  
2332 *ATLAS Silicon Tracking Detectors*, Tech. Rep. ATL-INDET-PUB-2005-002.  
2333 ATL-COM-INDET-2005-004. CERN-ATL-INDET-PUB-2005-002, CERN, Geneva, 2005.  
2334 <https://cds.cern.ch/record/835270>. 4.1, 4.1
- 2335 [32] ATLAS Collaboration Collaboration, *Alignment of the ATLAS Inner Detector Tracking*  
2336 *System with 2010 LHC proton-proton collisions at  $\sqrt{s} = 7$  TeV*, Tech. Rep.  
2337 ATLAS-CONF-2011-012, CERN, Geneva, Mar, 2011.  
2338 <https://cds.cern.ch/record/1334582>. 4.1, 4.2.3, 4.14
- 2339 [33] R. Härtel and S. Bethke, *Iterative local Chi2 alignment approach for the ATLAS SCT detector*.  
2340 PhD thesis, Nov, 2005. <http://cds.cern.ch/record/1511044>. Presented 28 Nov 2005. 4.1
- 2341 [34] ATLAS Collaboration Collaboration, P. Brückman de Renstrom, *Alignment strategy for the*  
2342 *Inner Detector of ATLAS*, . <https://cds.cern.ch/record/1047114>. 4.1
- 2343 [35] *Alignment of the ATLAS Inner Detector and its Performance in 2012*, Tech. Rep.  
2344 ATLAS-CONF-2014-047, CERN, Geneva, Jul, 2014.  
2345 <https://cds.cern.ch/record/1741021>. 4.1, 4.2.1, 4.4
- 2346 [36] J. J. Peña, *Alignment of the ATLAS Inner Detector Upgraded for the LHC Run II*, J. Phys.  
2347 Conf. Ser. **664** (2015) no. 7, 072025. 4.1
- 2348 [37] J. Alison and I. J. Kroll, *The Road to Discovery: Detector Alignment, Electron Identification,*  
2349 *Particle Misidentification, WW Physics, and the Discovery of the Higgs Boson*. PhD thesis,  
2350 Dec, 2015. <https://cds.cern.ch/record/1536507>. Presented 08 Nov 2012. 6
- 2351 [38] *ATLAS Inner Detector Alignment Performance with February 2015 Cosmic Rays Data*, Tech.  
2352 Rep. ATL-PHYS-PUB-2015-009, CERN, Geneva, Apr, 2015.  
2353 <https://cds.cern.ch/record/2008724>. 4.3, 4.2
- 2354 [39] ATLAS Collaboration Collaboration, M. Capeans, G. Darbo, K. Einsweiller, M. Elsing,  
2355 T. Flick, M. Garcia-Sciveres, C. Gemme, H. Pernegger, O. Rohne, and R. Vuillermet, *ATLAS*  
2356 *Insertable B-Layer Technical Design Report*, Tech. Rep. CERN-LHCC-2010-013.  
2357 ATLAS-TDR-19, Sep, 2010. <https://cds.cern.ch/record/1291633>. 4.2
- 2358 [40] *Alignment of the ATLAS Inner Detector with the initial LHC data at  $\sqrt{s} = 13$  TeV*, Tech.  
2359 Rep. ATL-PHYS-PUB-2015-031, CERN, Geneva, Jul, 2015.  
2360 <https://cds.cern.ch/record/2038139>. 4.2

- 2361 [41] *Study of the mechanical stability of the ATLAS Insertable B-Layer*, Tech. Rep.  
2362 ATL-INDET-PUB-2015-001, CERN, Geneva, Jun, 2015.  
2363 <https://cds.cern.ch/record/2022587>. 4.2.1
- 2364 [42] *Common Framework Implementation for the Track-Based Alignment of the ATLAS Detector*,  
2365 Tech. Rep. ATL-SOFT-PUB-2014-003, CERN, Geneva, Mar, 2014.  
2366 <https://cds.cern.ch/record/1670354>. 4.2.1
- 2367 [43] ATLAS Collaboration Collaboration, *Study of alignment-related systematic effects on the  
2368 ATLAS Inner Detector track reconstruction*, Tech. Rep. ATLAS-CONF-2012-141, CERN,  
2369 Geneva, Oct, 2012. <https://cds.cern.ch/record/1483518>. 4.4, 4.4, 4.4.1.1, 4.4.1.2
- 2370 [44] S. Marti-Garcia, S. Camarda, T. Golling, M. Danninger, N. A. Styles, J. Wollrath, W. K.  
2371 Di Clemente, S. Henkelmann, J. Jimenez Peña, O. Estrada Pastor, A. K. Morley, H. Oide,  
2372 A. T. Vermeulen, P. Butti, E. Ricci, F. M. Follega, and R. Iuppa, *Studies of radial distortions  
2373 of the ATLAS Inner Detector*, Tech. Rep. ATL-COM-INDET-2018-010, CERN, Geneva, Mar,  
2374 2018. <https://cds.cern.ch/record/2306724>. 4.4
- 2375 [45] ATLAS Collaboration Collaboration, *Electron and photon energy calibration with the ATLAS  
2376 detector using data collected in 2015 at  $\sqrt{s} = 13$  TeV*, Tech. Rep. ATL-PHYS-PUB-2016-015,  
2377 CERN, Geneva, Aug, 2016. <https://cds.cern.ch/record/2203514>. 4.4.1
- 2378 [46] ATLAS Collaboration, ATLAS Collaboration, *Evidence for Electroweak Production  
2379 of  $W^\pm W^\pm jj$  in  $pp$  Collisions at  $\sqrt{s} = 8$  TeV with the ATLAS Detector*, *Phys. Rev. Lett.* **113**  
2380 (2014) no. 14, 141803, arXiv:1405.6241 [hep-ex]. 5
- 2381 [47] CMS Collaboration, V. Khachatryan et al., *Study of vector boson scattering and search for  
2382 new physics in events with two same-sign leptons and two jets*, *Phys. Rev. Lett.* **114** (2015)  
2383 no. 5, 051801, arXiv:1410.6315 [hep-ex]. 5
- 2384 [48] ATLAS Collaboration Collaboration, *Observation of electroweak production of a same-sign  $W$   
2385 boson pair in association with two jets in  $pp$  collisions at  $\sqrt{s} = 13$  TeV with the ATLAS  
2386 detector*, Tech. Rep. ATLAS-CONF-2018-030, CERN, Geneva, Jul, 2018.  
2387 <https://cds.cern.ch/record/2629411>. 5, 5.7, 6.6.2
- 2388 [49] CMS Collaboration, CMS Collaboration, *Observation of electroweak production of same-sign  
2389  $W$  boson pairs in the two jet and two same-sign lepton final state in proton-proton collisions  
2390 at  $\sqrt{s} = 13$  TeV*, arXiv:1709.05822 [hep-ex]. 5
- 2391 [50] C. Bittrich, W. K. Di Clemente, et al., *Support note for measurement of electroweak  
2392  $W^\pm W^\pm jj$  production at  $\sqrt{s} = 13$  TeV*, Tech. Rep. ATL-COM-PHYS-2018-252, CERN,  
2393 Geneva, Mar, 2018. <https://cds.cern.ch/record/2309552>. 5, 5.3.3, 2, 4, 5.4.3
- 2394 [51] J. M. Campbell and R. K. Ellis, *Higgs Constraints from Vector Boson Fusion and Scattering*,  
2395 *JHEP* **04** (2015) 030, arXiv:1502.02990 [hep-ph]. 5.0.1, 5.0.2
- 2396 [52] M. Szleper, *The Higgs boson and the physics of  $WW$  scattering before and after Higgs  
2397 discovery*, arXiv:1412.8367 [hep-ph]. 5.0.1
- 2398 [53] E. Accomando, A. Ballestrero, A. Belhouari, and E. Maina, *Isolating Vector Boson Scattering  
2399 at the LHC: Gauge cancellations and the Equivalent Vector Boson Approximation vs complete  
2400 calculations*, *Phys. Rev.* **D74** (2006) 073010, arXiv:hep-ph/0608019 [hep-ph]. 5.0.1

- 2401 [54] C. Gumpert, M. Kobel, B. Heinemann, and U. Klein, *Measurement of Electroweak Gauge*  
 2402 *Boson Scattering in the Channel  $pp \rightarrow W^\pm W^\pm jj$  with the ATLAS Detector at the Large*  
 2403 *Hadron Collider.* PhD thesis, Dec, 2014. <https://cds.cern.ch/record/2003240>. Presented  
 2404 27 Feb 2015. 5.0.2, 5.1
- 2405 [55] B. Jager, L. Salfelder, M. Worek, and D. Zeppenfeld, *Physics opportunities for vector-boson*  
 2406 *scattering at a future 100 TeV hadron collider,* Phys. Rev. **D96** (2017) no. 7, 073008,  
 2407 arXiv:1704.04911 [hep-ph]. 5.6
- 2408 [56] J. Almond, L. Bianchini, et al., *Search for heavy neutrino,  $W_R$  and  $Z_R$  gauge bosons in events*  
 2409 *with two high- $P_T$  leptons and jets with the ATLAS detector in  $pp$  collisions at  $\sqrt{s} = 8$  TeV,*  
 2410 Tech. Rep. ATL-COM-PHYS-2013-810, CERN, Geneva, Jun, 2013.  
<https://cds.cern.ch/record/1555805>. Supporting note for EXOT-2012-24, published as  
 2412 JHEP07 (2015) 162. 5.0.3
- 2413 [57] ATLAS Collaboration, M. Aaboud et al., *Luminosity determination in  $pp$  collisions at  $\sqrt{s} =$*   
 2414 *8 TeV using the ATLAS detector at the LHC,* Eur. Phys. J. **C76** (2016) no. 12, 653,  
 2415 arXiv:1608.03953 [hep-ex]. 5.1
- 2416 [58] G. Avoni et al., *The new LUCID-2 detector for luminosity measurement and monitoring in*  
 2417 *ATLAS,* JINST **13** (2018) no. 07, P07017. 5.1
- 2418 [59] ATLAS Collaboration, G. Aad et al., *The ATLAS Simulation Infrastructure,* Eur. Phys. J.  
 2419 **C70** (2010) 823–874, arXiv:1005.4568 [physics.ins-det]. 5.1.1
- 2420 [60] S. Agostinelli et al., *GEANT4 - a simulation toolkit,* Nucl. Instrum. Meth. **A506** (2003)  
 2421 250–303. 5.1.1
- 2422 [61] T. Sjostrand, S. Mrenna, and P. Skands, *A Brief Introduction to PYTHIA 8.1,* Comput.  
 2423 Phys. Commun. **178** (2008) 852–867, arXiv:0710.3820 [hep-ph]. 5.1.1
- 2424 [62] T. Gleisberg et al., *Event generation with SHERPA 1.1,* JHEP **02** (2009) 007,  
 2425 arXiv:0811.4622 [hep-ph]. 5.1.1
- 2426 [63] S. Schumann and F. Krauss, *A parton shower algorithm based on Catani-Seymour dipole*  
 2427 *factorization,* JHEP **03** (2008) 038, arXiv:0709.1027 [hep-ph]. 5.1.1
- 2428 [64] S. Höche, F. Krauss, S. Schumann, and F. Siegert, *QCD matrix elements and truncated*  
 2429 *showers,* JHEP **05** (2009) 053, arXiv:0903.1219 [hep-ph]. 5.1.1
- 2430 [65] R. D. Ball et al., *Parton distributions for the LHC Run II,* JHEP **04** (2015) 040,  
 2431 arXiv:1410.8849 [hep-ph]. 5.1.1
- 2432 [66] S. Alioli, P. Nason, C. Oleari, and E. Re, *A general framework for implementing NLO*  
 2433 *calculations in shower Monte Carlo programs: the POWHEG BOX,* JHEP **06** (2010) 043,  
 2434 arXiv:1002.2581 [hep-ph]. 5.1.1
- 2435 [67] A. Ballestrero et al., *Precise predictions for same-sign  $W$ -boson scattering at the LHC,* Eur.  
 2436 Phys. J. **C78** (2018) no. 8, 671, arXiv:1803.07943 [hep-ph]. 5.1.1
- 2437 [68] J. Alwall, R. Frederix, S. Frixione, V. Hirschi, F. Maltoni, O. Mattelaer, H. S. Shao,  
 2438 T. Stelzer, P. Torrielli, and M. Zaro, *The automated computation of tree-level and*  
 2439 *next-to-leading order differential cross sections, and their matching to parton shower*  
 2440 *simulations,* JHEP **07** (2014) 079, arXiv:1405.0301 [hep-ph]. 5.1.1

- 2441 [69] H.-L. Lai, M. Guzzi, J. Huston, Z. Li, P. M. Nadolsky, J. Pumplin, and C. P. Yuan, *New  
2442 parton distributions for collider physics*, Phys. Rev. D **82** (2010) 074024, arXiv:1007.2241  
2443 [hep-ph]. 5.1.1
- 2444 [70] T. Sjostrand, S. Mrenna, and P. Skands, *PYTHIA 6.4 physics and manual*, JHEP **05** (2006)  
2445 026, arXiv:0603175 [hep-ph]. 5.1.1
- 2446 [71] ATLAS Collaboration, G. Aad et al., *Muon reconstruction performance of the ATLAS  
2447 detector in protonproton collision data at  $\sqrt{s} = 13$  TeV*, Eur. Phys. J. **C76** (2016) no. 5, 292,  
2448 arXiv:1603.05598 [hep-ex]. 5.2.1.1, 12
- 2449 [72] ATLAS Collaboration Collaboration, *Electron efficiency measurements with the ATLAS  
2450 detector using the 2015 LHC proton-proton collision data*, Tech. Rep.  
2451 ATLAS-CONF-2016-024, CERN, Geneva, Jun, 2016.  
2452 <https://cds.cern.ch/record/2157687>. 5.2.1.2
- 2453 [73] M. Cacciari, G. P. Salam, G. Soyez, *The anti- $k_t$  jet clustering algorithm*, JHEP **04** (2008) 063,  
2454 arXiv:0802.1189 [hep-ph]. 5.2.1.3
- 2455 [74] ATLAS Collaboration, M. Aaboud et al., *Jet energy scale measurements and their systematic  
2456 uncertainties in proton-proton collisions at  $\sqrt{s} = 13$  TeV with the ATLAS detector*, Phys.  
2457 Rev. **D96** (2017) no. 7, 072002, arXiv:1703.09665 [hep-ex]. 5.2.1.3
- 2458 [75] *Tagging and suppression of pileup jets with the ATLAS detector*, Tech. Rep.  
2459 ATLAS-CONF-2014-018, CERN, Geneva, May, 2014.  
2460 <http://cds.cern.ch/record/1700870>. 5.2.1.3
- 2461 [76] D. Adams, C. Anastopoulos, et al., *Recommendations of the Physics Objects and Analysis  
2462 Harmonisation Study Groups 2014*, Tech. Rep. ATL-PHYS-INT-2014-018, CERN, Geneva,  
2463 Jul, 2014. <https://cds.cern.ch/record/1743654>. 5.2.1.4
- 2464 [77] ATLAS Collaboration, M. Aaboud et al., *Measurement of the cross-section for producing a W  
2465 boson in association with a single top quark in pp collisions at  $\sqrt{s} = 13$  TeV with ATLAS*,  
2466 JHEP **01** (2018) 063, arXiv:1612.07231 [hep-ex]. 5.2.1.4
- 2467 [78] ATLAS Collaboration, M. Aaboud et al., *Performance of missing transverse momentum  
2468 reconstruction with the ATLAS detector using proton-proton collisions at  $\sqrt{s} = 13$  TeV*, Eur.  
2469 Phys. J. **C78** (2018) no. 11, 903, arXiv:1802.08168 [hep-ex]. 5.2.2
- 2470 [79] ATLAS Collaboration, M. Aaboud et al., *Measurements of b-jet tagging efficiency with the  
2471 ATLAS detector using  $t\bar{t}$  events at  $\sqrt{s} = 13$  TeV*, JHEP **08** (2018) 089, arXiv:1805.01845  
2472 [hep-ex]. 5.2.2
- 2473 [80] J.-F. Arguin, J. Claude, G. Gonella, B. P. Kersevan, K. Koneke, K. Lohwasser, K. Mochizuki,  
2474 M. Muskinja, C. Piaulet, and P. Sommer, *Support Note for Electron ID: charge  
2475 mis-identification*, Tech. Rep. ATL-COM-PHYS-2017-1014, CERN, Geneva, Jul, 2017.  
2476 <https://cds.cern.ch/record/2273365>. 5.3.3
- 2477 [81] C.-H. Kom and W. J. Stirling, *Charge asymmetry in  $W + \text{jets}$  production at the LHC*, Eur.  
2478 Phys. J. **C69** (2010) 67–73, arXiv:1004.3404 [hep-ph]. 5.4
- 2479 [82] R. Steerenberg, *LHC Report: Another run is over and LS2 has just begun...*,  
2480 [https://home.cern/news/news/accelerators/  
2481 lhc-report-another-run-over-and-ls2-has-just-begun](https://home.cern/news/news/accelerators/lhc-report-another-run-over-and-ls2-has-just-begun), 2018. Accessed: 2018-12-14. 6

- 2482 [83] *Letter of Intent for the Phase-I Upgrade of the ATLAS Experiment*, Tech. Rep.  
2483 CERN-LHCC-2011-012. LHCC-I-020, CERN, Geneva, Nov, 2011.  
2484 <http://cds.cern.ch/record/1402470>. 6
- 2485 [84] G. Apollinari, I. Bjar Alonso, O. Brning, M. Lamont, and L. Rossi, *High-Luminosity Large  
2486 Hadron Collider (HL-LHC): Preliminary Design Report*. CERN Yellow Reports: Monographs.  
2487 CERN, Geneva, 2015. <https://cds.cern.ch/record/2116337>. 6
- 2488 [85] ATLAS Collaboration Collaboration, ATLAS Collaboration, *ATLAS Phase-II Upgrade  
2489 Scoping Document*, Cern-lhcc-2015-020, Geneva, Sep, 2015.  
2490 <http://cds.cern.ch/record/2055248>. 6
- 2491 [86] D. Espriu and B. Yencho, *Longitudinal WW scattering in light of the “Higgs boson”  
2492 discovery*, Phys. Rev. D **87** (2013) 055017, arXiv:1212.4158 [hep-ph]. 6, 6.1
- 2493 [87] ATLAS Collaboration Collaboration, *Prospects for the measurement of the  $W^\pm W^\pm$  scattering  
2494 cross section and extraction of the longitudinal scattering component in pp collisions at the  
2495 High-Luminosity LHC with the ATLAS experiment*, Tech. Rep. ATL-PHYS-PUB-2018-052,  
2496 CERN, Geneva, Dec, 2018. <http://cds.cern.ch/record/2652447>. 6
- 2497 [88] ATLAS Collaboration Collaboration, *Studies on the impact of an extended Inner Detector  
2498 tracker and a forward muon tagger on  $W^\pm W^\pm$  scattering in pp collisions at the  
2499 High-Luminosity LHC with the ATLAS experiment*, Tech. Rep. ATL-PHYS-PUB-2017-023,  
2500 CERN, Geneva, Dec, 2017. <https://cds.cern.ch/record/2298958>. 6, 6.4
- 2501 [89] T. Sjöstrand, S. Ask, J. R. Christiansen, R. Corke, N. Desai, P. Ilten, S. Mrenna, S. Prestel,  
2502 C. O. Rasmussen, and P. Z. Skands, *An Introduction to PYTHIA 8.2*, Comput. Phys.  
2503 Commun. **191** (2015) 159–177, arXiv:1410.3012 [hep-ph]. 6.2
- 2504 [90] ATLAS Collaboration Collaboration, *Expected performance for an upgraded ATLAS detector  
2505 at High-Luminosity LHC*, Tech. Rep. ATL-PHYS-PUB-2016-026, CERN, Geneva, Oct, 2016.  
2506 <http://cds.cern.ch/record/2223839>. 6.3
- 2507 [91] P. C. Bhat, H. B. Prosper, S. Sekmen, and C. Stewart, *Optimizing Event Selection with the  
2508 Random Grid Search*, Comput. Phys. Commun. **228** (2018) 245–257, arXiv:1706.09907  
2509 [hep-ph]. 6.5.1
- 2510 [92] G. Cowan, K. Cranmer, E. Gross, and O. Vitells, *Asymptotic formulae for likelihood-based  
2511 tests of new physics*, Eur. Phys. J. **C71** (2011) 1554, arXiv:1007.1727 [physics.data-an].  
2512 [Erratum: Eur. Phys. J.C73,2501(2013)]. 6.5.1